Department of Precision and Microsystems Engineering

Design of a low cost displacement interferometer

Wei She

Report no : 2022.031
Coach : Dr N. Bhattacharya
Dr W. Pril
Specialisation : OPT
Type of report : Master thesis
Date : 2022-07-01

Abstract

Lithography machines that manufacture integrated circuits require non-contact and nanometer-scale position measurement, which is led by displacement laser interferometer in some ASML machines. The aim of the project is to design a displacement interferometer using non-polarizing light to meet the requirements and be cost-effective. The design is challenging considering the requirements of 350 mm measurement range, 300 μrad angular range and less than 1 nm periodical non-linearity (PNL) error.

This thesis analyzes all the design requirements first. To fulfill the requirements, efficient design strategies are clarified, and the phase detection method is determined.

Three interferometer designs are investigated and developed in this thesis. The design concepts are collected from ASML internal references. Mathematical models are built to represent the optics and trace the light in each interferometer. Optimization tools are developed to solve and tune the parameters that fulfill all the dimension-related requirements. Geometrical optics simulations are performed to verify the mathematical models and the optimization results. The source and behavior of PNL error in each interferometer are carefully researched. In a design with lenses, sequential mode simulations are performed to calculate the wavefront error. Further calculations based on the wavefront error indicate this interferometer design is not feasible.

Based on the theoretical analysis two interferometer designs can fulfill all the requirements. These two interferometers are built in the cleanroom with off-the-shelf parts to validate the working principle and PNL errors. The optics, optomechanics and electronics used in the tests are explained. The methods of alignment and measurement are introduced. The working principles of the two interferometers are validated, and the behaviors of PNL error match the theoretical analysis.

Contents

Chapter 1

Introduction to the project

1.1 Motivation

With the fast development of semiconductor industry, demand for precise measurement increases continuously. Developments in semiconductor industry are lead by Moore's law [1], which observes that the number of transistors in a dense integrated circuit (IC) doubles about every two years. To achieve this goal, precise measurement technology has to be developed, with smaller uncertainty, higher repeatability and reproducibility. These key terms of measurement science have been defined in the famous GUM series [2]:

- Measurand: particular quantity subject to measurement.
- Uncertainty: parameter, associated with the result of a measurement, that characterizes the dispersion of the values that could reasonably be attributed to the measurand.
- Accuracy: closeness of the agreement between the result of a measurement and a true value of the measurand.
- Repeatability: closeness of the agreement between the results of successive measurements of the same measurand carried out under the same conditions of measurement.
- Reproducibility: closeness of the agreement between the results of measurements of the same measurand carried out under changed conditions of measurement.

Though absolute measurement can never be realized, effort has been made to achieve higher accuracy, repeatability, reproducibility and minimize the uncertainty.

Lithography machines that manufacture integrated circuits require non-contact and nanometer-scale position measurement. Capacitive sensors are able to fulfill the accuracy and non-contact requirements [3], however, the measurement range is limited to a few millimeters. In lithography machines the measurand is a wafer stage with several hundred millimeters moving range. A laser interferometer is an instrument that can achieve sub-nanometer measurement accuracy throughout a large measurement range. It also has the benefits of high repeatability, and does not come in contact with the measured device. With these advantages, the laser interferometer is used as an effective instrument for stage position measurement in lithography machines.

1.2 Project aim

Many high-precision interferometers on the market can meet the product needs of ASML, a leading manufacturer of lithography machines. But if they were to be implemented, it would lead to high costs. Therefore, in order to reduce the cost and meet the specific accuracy requirements, as well as be compatible with the existing system, a new interferometer needs to be developed. The interferometer works in an environment where the temperature ranges from 20 to 24°, the temperature gradient is less than 1° per hour, the air pressure ranges from 78.0 to 101.4 kPa, the pressure gradient is less than 2.0 kPa per hour [4]. The main goal of this project is to develop an alternative interferometer to achieve desired accuracy and be cost effective. The aim of this project is to:

Design a low cost fiber delivered displacement interferometer using 1532 nm laser source.

The interferometer should achieve the requirements in Table 1.1.

Table 1.1: Interferometer design requirements

Function	**Specification**
Measurement range	350 mm
Maximum deadpath	350 mm
Target angular range	> 300 μrad
Modulation depth of interference	$> 50\%$
Beam area on the target mirror	within 20×8 mm^2
Periodical non-linearity error amplitude	< 1 nm
Thermal sensitivity	< 15 nm/K

To further understand what affects the design requirements, some prior knowledge of the displacement interferometry is needed. The relevant background knowledge is introduced in Chapter 2. The elaborations on the design requirements and preliminary design choice are discussed in Chapter 3. In the existing system, the light emerging from the fiber has a Gaussian intensity profile with a waist diameter of 3.6 mm, which is used throughout the project.

Chapter 2

Displacement interferometry

2.1 Components in the interferometer

In this section, optical components that are often used in displacement interferometry are introduced. This will help with interpreting how different interferometer systems work.

Laser as light source

The displacement interferometer requires a monochromatic light source. Narrow linewidth (high degree of monochromaticity), high degree of temporal coherence, power stability are essential requirements for the observation of steady interference fringes throughout large measurement distance.

Helium-neon (He-Ne) laser is widely used for interferometry because it meets all the above mentioned requirements, is inexpensive and provides a continuous, visible output. It normally operates at a wavelength of 633 nm. The main drawback of He-Ne laser is the short mean time between failures. It has continuous power output ranging from less than 1 mW to over 50 mW (in frequency stabilized He-Ne laser the output power is around 1 mW). It typically has a lifetime of 50,000 hours (less than 6 years of 24/7 operation) [5].

Laser diodes have various advantages when used as the source in fiber interferometers. They can be as small as needle tips, operate in wide range of wavelengths typically from 375 nm to 2000 nm, have high electrical to laser power conversion efficiency of over 30%, can be operated by battery, and can be modulated to Giga hertz frequencies by changing the injection current or temperature [6]. An undesired behavior encountered in application of wavelength modulation is mode hopping. Normally the wavelength shifts slowly with temperature, however when the laser switches from one longitudinal mode to another (mode hopping), the wavelength may make discrete jumps [7]. During mode hopping, the laser's output power fluctuates slightly, resulting in an increase in relative noise. Drawbacks of laser diode beams are large divergence, elliptical shape and astigmatism. However, packages incorporating additional optics are able to produce a collimated beam [8]. Further discussion on laser linewidth and stability is covered in later Section 2.4.

Optical fiber

An optical fiber has a cylindrical structure that transports electromagnetic waves in infrared or visible bands of electromagnetic spectrum. Optical fibers consist of three different layers. A central core is surrounded by a cladding, which is then covered by a protective jacket. Depending on the number $\nu = 2\pi a\sqrt{n_{co}^2 - n_{cl}^2}/\lambda$, optical fibers are divided into multi-mode ($\nu \gg 1$) and Single-Mode Fiber (SMF) ($0 < \nu < \nu_c$), where a is the core radius, λ is the wavelength of the light in free space, n_{co} and n_{cl} are the core and cladding refractive indices respectively, ν_c is cut off frequency [9]. A SMF with $\nu_c < 2.405$ typically is designed to carry only one transverse mode of light [10]. A multi-mode fiber has a fairly large core diameter that enables multiple light modes to be propagated, which is detrimental to collimation and interference.

The asymmetry from the manufacturing process or mechanical stresses after installation can lead to birefringence, polarization mode coupling or random polarization rotations along the SMF, which is referred to as polarization mode dispersion [11]. This effect is detrimental to optical communications and interference. Random polarization rotation can be overcome by using a Polarization Maintain Fiber (PMF). Light propagates without any disturbance in its polarization state when aligned to one of the principle axes of the PMF.

Optical circulator

An optical circulator is a device made with typically 3 or 4 ports. It allows light to travel in only one direction. An example of a three-ports optical circulator is shown in Figure 2.1. Light entering to Port 1 will exit Port 2 with minimal loss, while light entering Port 2 will exit Port 3 with minimal loss. Light entering Port 2 experiences a large amount of loss at Port 1, and light entering Port 3 experiences a large amount of loss at Ports 2 and 1. The four-ports optical circulator is not shown here but follows the same rules.

With the use of optical circulators, light can be delivered and acquired by the same fiber tip (collimator package). In other words, using a circulator light from a fiber can be sent into a different system, typically in free space, recollected by the same fiber, and most of the light will still be received by the photodetector. Only a very small amount of light is sent back into laser source. Thus the disturbance from the received light to the laser source is minimized.

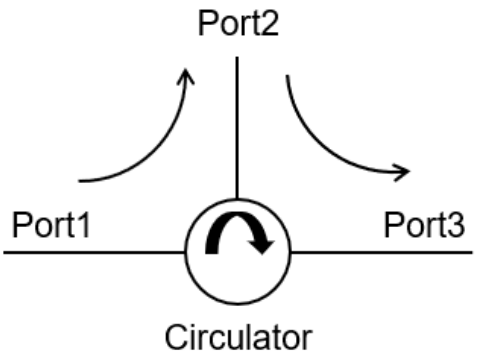

Figure 2.1: Example of a three-ports optical circulator

Retroreflector

The Corner-Cube Retroreflector (CCR) is an optical structure that consists of three adjacent, mutually-orthogonal reflective planes. The intersection point of the three planes can be seen as the corner of a cube. It is designed to reflect an input beam once per plane. The reflected beam is always parallel to the incident beam, independent of the orientation of the CCR and the incident beam.

To be more specific, the exit beam and incident beam are collinear if the incident beam is aligned to the vertex of CCR. Otherwise the two beams are still parallel but separated. The position of the first reflection determines which sequence of reflections the beam will follow. Beam always exits from the opposite segment.

The polarizing properties of the CCR are important to account for when used in interferometer systems. A basic Total Internal Reflection (TIR) CCR is shown in Figure 2.2. An anti-reflective coating at the entrance of the TIR CCR is optional to prevent potential ghost reflections.

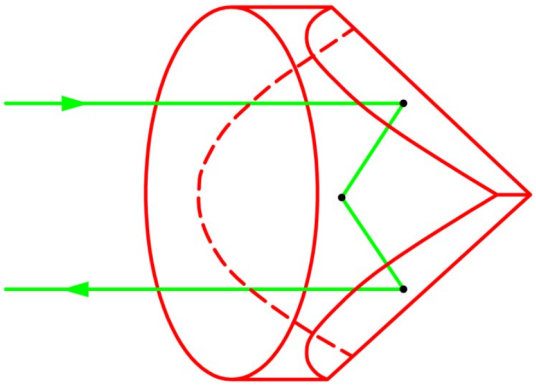

Figure 2.2: Ray trajectory in a total internal reflection corner-cube retroreflector [12]

In Figure 2.2, the incident light is normal to the incident plane. To ensure total internal reflection, the CCR is typically designed such that each face would have an incident angle of 54.7356° for normal incident beams [13]. According to the refraction law [14], the total internal reflection angle is:

$$\theta_{in} = \arcsin \frac{n_{air}}{n_{glass}} \tag{2.1}$$

Where n_{air} is the refractive index of the substance outside CCR, n_{glass} is the refractive index of CCR. A CCR made from BK-7 has refractive index of 1.513 [15]. The refractive index of air is approximately 1, the exact value of which does not matter for the illustrative purposes. Equation 2.1 gives a result of θ_{in} = 41.3715°. The geometrical incident angles 54.7356° are larger than θ_{in}, which means the three reflections are total internal reflections. The s- and p- polarizations will reflect from each face with a different phase delay dependent on the angle of incidence and the refractive indices. This difference of phase delay is detrimental for the interference signal, and finally introduces error in displacement measurement. A metal-coated CCR minimizes changes in polarization states by using the specular reflection principle.

2.2 Different types of interferometer

Through the years, variable concepts of interferometer have been designed. The working principles and their pros and cons are introduced in this section.

Michelson interferometer

Michelson interferometer [16], shown schematically in Figure 2.3, uses a beam splitter to divide and combine the monochromatic light beams. Mirror M_2 is fixed. When the other mirror M_1 is moving, an interference pattern is observed and changes on the screen. The Michelson interferometer model is simple. However, small misalignments and angular deviations of the reference mirror and the measured target can harm the measurement performance a lot.

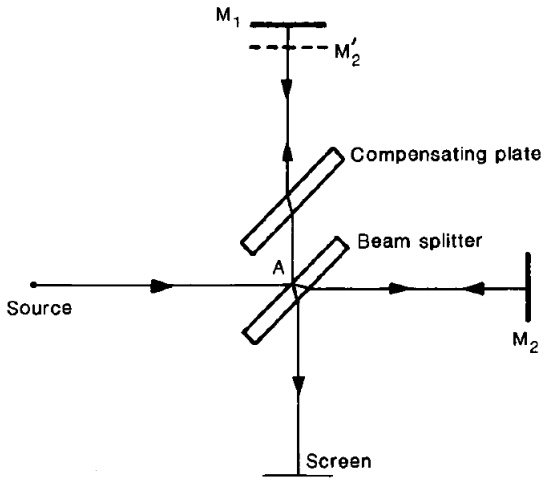

Figure 2.3: Configuration of a Michelson interferometer [17]

Fizeau interferometer

A basic layout of a Fizeau interferometer is shown in Fig. 2.4. A laser source is spatially filtered via a microscope objective and a pinhole. This pinhole is located at the focal point of a collimating lens. Between the pinhole and lens is a beam splitter. The collimated beam encounters the reference surface and reflects at the test surface. The return beam contains information on aberration introduced by the test surface. Thus the Fizeau interferometer is commonly used for measuring the shape of an optical surface. This type of interferometer is not suitable for displacement measurement.

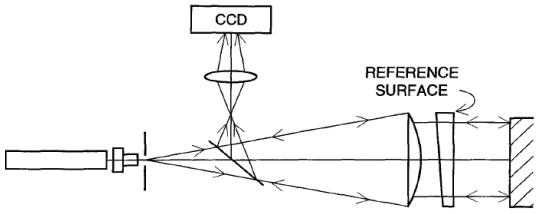

Figure 2.4: Configuration of a Fizeau interferometer [18]

Mach-Zehnder interferometer

A basic layout of a Mach-Zehnder interferometer is shown in Figure 2.5. A light beam is first split into two parts by a beamsplitter and then combined by a second beamsplitter. Depending on the relative phase acquired by the beam along the two paths, the second beamsplitter will reflect the beam with efficiency between 0 and 100%. The Mach-Zehnder interferometer is also sensitive to misalignments.

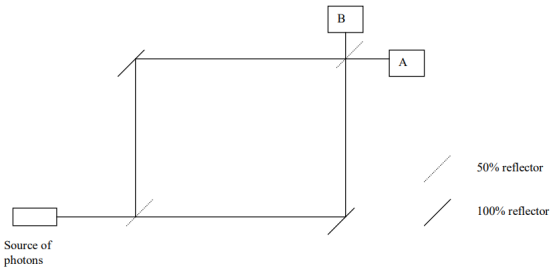

Figure 2.5: Configuration of a Mach-Zehnder interferometer [17]

Plane mirror interferometer

A more complex interferometer with a Polarizing Beam Splitter (PBS), quarter-wave plates and a corner-cube retroreflector gets around the issues of misalignment sensitivity and angular sensitivity of the measured target. A PBS allows light in p-polarization to pass through unhindered, and reflects light in s-polarization. A quarter-wave plate using the principle of birefringence can transform linearly polarized light to circularly polarized light and vice-versa.

A typical Plane Mirror Interferometer (PMI) layout is shown schematically in Figure 2.6. The source emits light with equal s- and p-polarizations. Upon striking the interface of a PBS, the s-polarization will be diverted to the upper CCR, while the p-polarization will pass on to the plane reflector. Then the incoming measurement beam with p-polarization transmits through the quarter-wave plate a second time, and exits with s-polarization. Next it is diverted to the CCR and passes on to the plane reflector again (called second pass). The returning measurement beam with p-polarization is mixed with the s-polarized reference beam. Then they pass through a mixer (polarizer), which selects out the common linear polarization between the two. This is what the detector sees.

A major advantage of the double pass PMI is that it has a low sensitivity to angular deviations of the target mirror. In addition, if there is no misalignment, both the reference beam and the measurement beam have undergone through common path in PBS and CCR, which means that any changes in the reference arm will be seen by the measurement arm, and thus cancelled out.

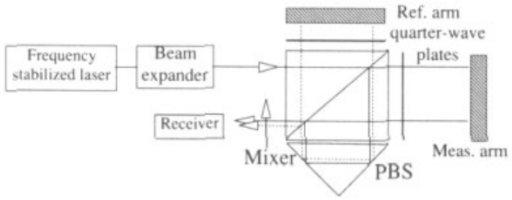

Figure 2.6: Configuration of a plane mirror interferometer [19]

Conclusion on interferometer design

Table 2.1: Summary on different types of interferometer

Model	Advantage	Disadvantage
Michelson	Simple layout	1.Optical power loss 2.Misalignment sensitive
Fizeau	Not feasible for displacement measurement	
Mach-Zehnder	Highly configurable	Misalignment sensitive
PMI	1.Large angular range 2.Long common path	1.Complex 2.Need polarization control

Table 2.1 summarises the advantages and disadvantages of using the interferometers discussed in this section.

2.3 Phase detection approach

Homodyne detection with quadrature detection

Homodyne interferometers have the same frequencies in the reference and measurement arms. Homodyne interferometers in metrology are typically realized with a Michelson-type layout. However, the measurement based on the layout shown in Figure 2.3 can not determine the di-

rection of target movement at the moment when maximum or minimum power is observed.

A typical layout solving the directional ambiguity is shown in Figure 2.7. A linearly polarized laser beam passes through a quarter-wave plate and it becomes circularly polarized. In order for this to occur, the incoming beam's polarization direction needs to be at 45° relative to the quarter-wave plate's principal axis. Circularly polarized light has orthogonal fields that are 90° apart in phase. A polarizing beamsplitter then splits the output beam into two orthogonally polarized beams, each sensed by a detector. As a result, depending on the direction of the mirror's movement, detector 1 leads or lags detector 2. This phase information can then be used to deduce the direction of movement and therefore the position of the mirror.

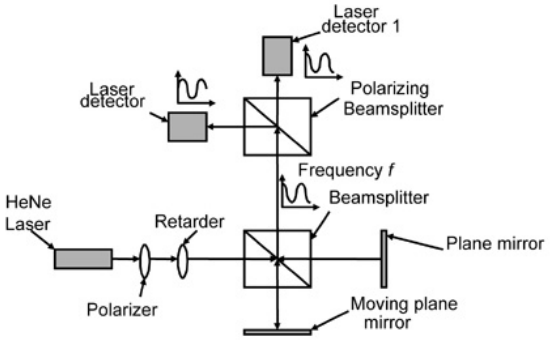

Figure 2.7: Homodyne laser interferometer with quadrature detection [20]

Quadrature detector systems have common error sources: the phase shift between signals of two detectors is not exactly 90°, unequal gain in different detector channels and zero offset. These error sources result in periodic non-linearity errors, which is discussed further in Section 2.4. A simple post-processing method to get rid of these errors is introduced in [21].

Homodyne detection using phase-generated-carrier

Another solution for directional ambiguity is to modulate the phase at a detectable frequency, which is far lower than the frequency of light [22]. To explain the demodulation algorithm, first in a homodyne interferometer without Phase-Generated-Carrier (PGC) approach, the detected irradiance can be represented as:

$$I = A + B\cos\varphi(t) \tag{2.2}$$

Where $\varphi(t)$ is the phase difference between the different arms of interferometer. The constants A and B are proportional to the input optical power. If a sinusoidal modulation with a frequency ω_0 and amplitude C is applied on the laser source, Equation 2.2 becomes:

$$I = A + B\cos(\,C\cos\omega_0 t + \varphi(t)) \tag{2.3}$$

Use the Jacobi-Anger expansion [23] to expand Equation 2.3 into the Bessel series:

$$I = A + B\{[\,J_0(C) + 2\sum_{k=1}^{\infty}(-1)^k J_{2k}(C)\cos(\,2kw_0t)\,]\,\cos\varphi(t) \\ -[\,2\sum_{k=0}^{\infty}(-1)^k J_{2k+1}(C)\sin(\,(\,2k+1)\,w_0t)\,]\,\sin\varphi(t)\} \tag{2.4}$$

From this expression, the sidebands contain the signal of interest and are either present about the even or the odd multiples of the modulated frequency ω_0. The signal is obtained by multiplying the total output signal with the proper multiple of ω_0.

Heterodyne displacement interferometer

The homodyne interferometer uses a single frequency of light, and the "difference" between the measurement and reference signals only shows up as a baseband phase and detected irradiance is a variation away from DC. DC detection is slow and suffers from $\frac{1}{f}$ and other noise in detectors. Signal irradiance variations (due to air turbulence or accumulated contaminants on mirror and optic surfaces) are indistinguishable from position changes.

A heterodyne interferometer uses a laser source with two orthogonally polarized, close together frequencies f_1 and f_2. When the two different frequencies are mixed with e.g. a polarizer, it produces a signal with a beat envelope at a frequency of $f_1 - f_2$, and a carrier frequency of $(f_1 + f_2)/2$. The carrier frequency is automatically low-pass filtered out by the detector, leaving the beat frequency as the only detected time-varying signal. Figure 2.8 shows a typical configuration of a heterodyne interferometer. A single laser is made to produce two frequencies of light in orthogonal linear polarizations. Distance measurement is the phase difference between the reference and measurement signals. The reference signal is a fixed phase beat frequency, which is obtained by mixing the two frequencies before the interferometer. The measurement signal is a beat frequency modulated by the moving object.

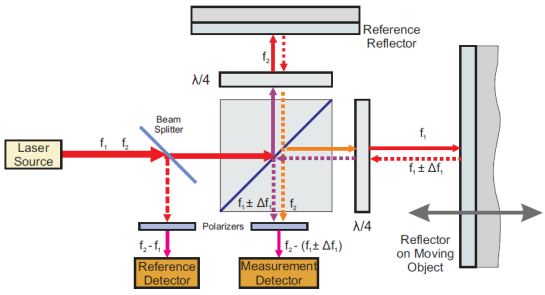

Figure 2.8: Heterodyne interferometer [24]

Synthetic-heterodyne displacement interferometer

Synthetic-heterodyne demodulation is a useful technique for dynamic displacement and velocity measurement using interferometric sensors as it can provide an output signal, which is

immune to interferometric drift [25]. The basic synthetic-heterodyne demodulation algorithm is introduced in [26], which requires knowledge of the interferometer visibility and also the argument of the even and uneven Bessel functions. Improved synthetic-heterodyne demodulation algorithm is introduced in [25].

Conclusion on phase detection

Table 2.2: Summary of phase detection approaches

Approach	Advantage	Disadvantage
Homodyne quadrature detection	Single frequency light source	1.Need elements for retarding and dividing light 2.Need two detectors 3.DC detection
PGC detection	Simple layout	Need frequency modulation and stabilization
Heterodyne detection	1.Fast 2.AC detection	1.Need light source consisting of two frequencies 2.Need polarization control
Synthetic-heterodyne detection	Suitable for the velocity measurement	

Table 2.2 summarises the advantages and disadvantages of using different phase detection approaches discussed in this section.

2.4 Introduction to error sources

A displacement interferometer measures displacement based on the relative phase difference between the measurement and reference beams. Therefore, anything affecting the measured phase or wavelength affects the accuracy of measurement. In this section, several types of error source existing in interferometer system and compensation methods are introduced.

Periodical non-linearity error

Periodic Non-Linearity (PNL) error is linked to unintended signals reaching the detector, which distorts the signal from the ideal. The PNL typically refers to error signals with a period of one wavelength of optical path change [27]. PNL error of an interferometer usually ranges from sub-nanometer scale to several nanometers, depending on the source of the error [28].

PNL error exists both in homodyne and heterodyne interferometers. In homodyne interferometers using polarizing optics, the PNL error is the dominant error due to polarization leakage between different polarizations. In addition, the PNL error in a homodyne interferometer can also originate from multi-order ghost reflections, which makes the error very difficult to compensate for in the hardwares [29]. The non-linearity of a heterodyne interferometer originates mainly from the cross talk between different frequencies of two linearly polarized beams, which has been investigated by [30]. PNL error also arises from the imperfection or misalignments of interferometer optics [31]. To reduce these errors, modern interferometers use higher quality PBSs and wave plates.

Laser wavelength accuracy

For most interferometric setups, a monochromatic light source is essential for measurement accuracy. Michelson used a sodium flame as monochromatic light source. Although it contains a

narrow range of optical frequencies, its stability is not sufficient for modern measurements. The Pound-Drever-Hall technique is a widely used and powerful approach for stabilizing the frequency of light emitted by a laser by means of locking to a stable cavity [32]. With the progress of semiconductor lasers, Distributed Feedback (DFB) [33] have been fabricated. DFB lasers are narrow-linewidth, single-frequency laser diodes that use a corrugated waveguide throughout the active region of the laser cavity. Thus DFB lasers are perfectly suitable for the use in interferometry.

With the wavelength stabilized, interferometers used in the vacuum environment can achieve a very small value of wavelength uncertainty. For applications in air, a discussion of the atmospheric effects on the wavelength of the measured beam is introduced in next section.

Atmospheric compensation

Since the wavelength of light from a particular laser is specified in vacuum, λ_{vac}, for operation in air, an accurate measurement of refractive index of air n_{air} is essential to get the exact wavelength in air:

$$\lambda_{air} = \frac{\lambda_{vac}}{n_{air}} \tag{2.5}$$

In 1966, the Edlén equation [34] was created from numerous measurements with different air pressure, temperature, humidity and gas compositions that relates the refractive index to these measured parameters. Later improved equations better suited to the very wide ranges of atmospheric conditions have been developed [35, 36, 37, 38]. In short, the Edlén Equation describes the variability of the refractive index of the optical path, which can be simplified to:

$$n - 1 = K(\lambda)\frac{P}{T}\frac{1 + \epsilon P(1 - \alpha T)}{1 + \frac{\delta}{T}} \approx K(\lambda)\frac{P}{T} \tag{2.6}$$

Where $K(\lambda)$ is a wavelength dependent scaling factor, $\rho = \frac{P}{T}$ is the density of air.

Error originating from the setup

Some error sources are from misalignments of the setup or the thermal expansion of materials.

All distance measurements are prone to cosine error and Abbe error. Cosine error exists when the measurement axis is not perfectly parallel with the line connecting the two measured points. Abbe error is defined as [24]:

$$\varepsilon_{Abbe} = L \tan\theta \tag{2.7}$$

Where L represents the lateral offset between the desired axis of measurement and the actual axis of measurement and θ represents the angle between the normal of the mirror and the measurement axis.

Both interferometer and the object being measured undergo thermal expansion when the ambient temperature changes. For short measurement ranges, it is possible to compensate thermal expansion by balancing the optical path, so that interferometer temperature changes affect both beams almost equally.

Chapter 3

Preliminary design analysis

In Chapter 2 several types of interferometers and phase detection algorithms have been introduced for the purpose of designing a low cost, 1532 nm interferometer. The interferometer should be able to work over 350 mm measurement range and over 300 μrad angular range of the measured target, with a deadpath of no more than 350 mm, PNL error less than 1 nm and thermal sensitivity less than 15 nm/K. By analyzing the prior art, preliminary design choices on the interferometer layout and phase detection approach will be made.

Section 2.3 shows that both homodyne and heterodyne detection methods can obtain the magnitude and direction of the displacement from the interference signal. Both conventional homodyne quadrature detection and heterodyne detection require multiple detectors, retardation plates and polarizing optics, meaning these are not cost-effective approaches. PGC detection instead only requires a single detector and can be implemented with non-polarizing optics, making it the superior choice.

In order to design an interferometer satisfying all the requirements, the influence of the configuration of the interferometer and the PGC phase detection approach should be elaborated on.

- **Measurement range**
  The interferometer should be able to measurement the displacement of the target from its deadpath to the deadpath plus the measurement range. Two factors associated to the measurement range should be considered:

  1. *Beam walk-off*
     The measurement beam will deviate from its original path when the target mirror deviates from the ideally positioned angle. The offset between the reference and the measurement beam is called beam walk-off. The beam walk-off is zero at the target mirror, however, the walk-off is scaled with the measurement distance. It generally follows this relationship:

$$\text{Walk-off} = NoP \cdot s \cdot \theta \tag{3.1}$$

     Where NoP is the number of passes, e.g., for a single-pass interferometer the NoP

= 2, for a double-pass interferometer the NoP = 4. s is the distance between the observing beam shift position and the target, θ is the tip-tilt angle of the target. The maximum permissible beam walk-off depends on the design of the interferometer. Equation 3.1 also indicates how the measurement range and angular range requirements are associated: when the maximum permissible beam walk-off is fixed, the larger the measurement distance is, the smaller the permissible angular deviation of the target mirror is. Thus, the angular range should be evaluated at the maximum measurement distance.

2. *Interferometer design*
   The maximum permissible beam walk-off depends on the design of the interferometer. More specifically, the exact beam walk-off under target tip-tilt has to be derived from the changes of the beam path determined by the interferometer optics. By changing the design, the beam walk-off can be either exaggerated or mitigated (even fully compensated) compared to its general Equation 3.1.

- **Deadpath**
  The deadpath is the part of the optical path that is not part of the measurement [24]. The deadpath is added to the measurement distance, which reduces the angular range of the target. In addition, the deadpath in free space introduces a deadpath error when the temperature changes [24]. In addition, due to the beam divergence, the beam diameter becomes larger as it travels longer. Thus, it is preferable to have a smaller deadpath. It is possible to balance the deadpath by adding an extra path either in the reference arm or in the measurement arm in the design. The maximum deadpath requirement is given considering the deadpath is no larger than the measurement range. This introduces a limit on the Optical Path Difference (OPD). Complementary information on the PGC detection algorithm is that it introduces a limit on the minimum deadpath [39]:

$$\frac{OPD_{max}}{OPD_{min}} \leq 2.5 \tag{3.2}$$

  Where OPD_{max} and OPD_{min} represent the OPD when the target mirror is at the maximum and minimum measurement distance, respectively. Substituting OPD_{min} = Deadpath and OPD_{max} = Deadpath + Measurement Range leads to the result:

$$\text{Deadpath} \geq \frac{2\,\text{Measurement Range}}{3} \tag{3.3}$$

  The measurement range requirement is 350 mm, according to Equation 3.3 the corresponding minimum deadpath limited by the PGC is about 233 mm. This minimum deadpath value will often be referred to in the design of the interferometers.

- Target angular range
  Section 2.2 shows that the PMI has a larger angular range than the single-pass Michelson interferometer. In principle, double-pass interferometers transfer the angular mismatch into a beam walk-off, within certain range of which a good contrast interference is ensured. This certain range of beam walk-off limits the angular range of the target. It is possible to minimize the beam walk-off by changing the interferometer design. As Equation 3.1 shows, the beam walk-off is maximum at the maximum measurement distance, and thus the angular range of the target mirror should be specified for the maximum measurement distance.

- Modulation depth
  The modulation depth can be defined as the modulation amplitude (i.e. one-half of the peak-to-peak changes) divided by the mean value [40]. The interference of two waves with the same amplitude has a modulation depth of 100%. If one of the wave has a much smaller amplitude than the other, the modulation depth tends to zero, thus the signal from the detector will be dominated by the DC component. Assuming one of the reference and the measurement beams is perfectly coupled to the receiving fiber, any beam walk-off or beam misalignment degrades the signal modulation depth. The 50% modulation depth requirement can determine the value of maximum permissible beam walk-off or the beam misalignment.

- Beam area on the target mirror
  In double or more pass interferometers, the measurement beams strike the target mirror at more than one position. These beam striking positions are mainly determined by the interferometer design, and they should be limited to a small area. Although the mirror chuck at the wafer stage should be sufficiently large to reflect beams throughout the measurement range, a longer beam area increases the length of the mirror considering the two ends of the measurement range, and a wider beam area directly increases the width of the mirror. The additional extra mirror area means an extra mass and cost. First, for a given motor power, the additive mass reduces the acceleration of the wafer stage, which increases the time it takes to move the stage. Second, in order to accommodate larger mirrors, the volume of the stage also needs to be increased, which means that the increase in mass is non-linear with the increase in beam area on the target mirror. The beam area on the target mirror requirement is given considering being compatible with the existing system.

- PNL error
  Section 2.4 introduces the properties and sources of the PNL error. The PNL error mainly originates from the multi-order ghost reflections in a homodyne interferometer without using polarizing optics. The amplitude and frequency of the PNL error should be derived based on the specific interferometer design. Heydemann fitting can be used to compensate the PNL error that is harmonics of the fringe [21].

- Thermal sensitivity
  If the reference and measurement beams have non-common optical path in the interferometer optics, the material thermal expansion of the interferometer optics results in different optical path changes in the two beams, which is falsely interpreted as a target displacement.

The speed limit is not mentioned in the requirements, but it is also worth an investigation. When using the PGC as the phase detection algorithm, the modulation frequency f_{mod} determines the speed limit. The permissible fringe moving frequency is $\pm 0.4 f_{mod}$ with a margin considered. For a double-pass interferometer, the speed limit of the target in meter per second is $\pm 0.1 f_{mod} \lambda$. The larger the number of pass is, the smaller the speed limit of the target is. Limited by the bandwidths of electronics, the modulation frequency in the existing system is up to 10 MHz, which permits a maximum target velocity of 1.52 m/s. This speed limit is acceptable for stage position measurement. When the number of pass of the interferometer becomes larger, it will limit the detectable speed.

In conclusion, a new interferometer using the PGC phase detection method needs to be de-

signed, in order to reduce cost and meet the specified requirements, as well as to be compatible with the existing system at ASML, primarily using a 1532 nm fiber delivered light source. Based on the elaborations on the requirements, Table 3.1 concludes the strategies that can be used to fulfill the requirements. Besides using the strategies to design and verify the feasibility of an interferometer, any risk of spoiling the interference in a specific interferometer design should also be carefully investigated.

Table 3.1: Design strategies for the design requirements

Requirements	**Design strategies**
Measurement range	1. Minimize the deadpath 2. Mitigate the beam walk-off
Deadpath	1. Minimize the deadpath to the PGC detection limit 2. Balance the deadpath of the reference and measurement beams
Target angular range	1. Minimize the deadpath 2. Mitigate the beam walk-off
Beam area on the target mirror	Minimize the beam shift caused by the interferometer design
PNL error	1. Prevent disturbing interference, e.g., make the disturbing reflection occur at an angle 2. Apply an Anti-Reflective (AR) coating on the optical interfaces generating ghost reflections
Thermal sensitivity	Balance the thermal sensitivity of the reference and measurement paths so that the temperature influence is cancelled out

Among all the requirements, the two requirements, the PNL error and the thermal sensitivity, need to be considered independently of the other requirements, respectively. Some PNL error can be prevented by the interferometer design, and some can be reduced by using high quality optics with efficient anti-reflective coating. The PNL error can also be compensated in post-processing as it is predictable. Thermal sensitivity can be qualitatively investigated based on the interferomter design, but the quantitative investigations can only be done after the design is built with the materials and methods of mount determined. In the interferometer design investigations, the feasibility analysis will focus on the requirements of the measurement range, angular range, deadpath and beam area on the target mirror. If the design is feasible, then the PNL error of the design will be investigated.

Chapter 4

Double-pass Lens-based Interferometer

Section 2.2 shows that the PMI has a large angular range of the measured target due to its double-pass design. The relatively high cost polarizing optics makes the PMI not ideal for low cost uses. An ideal interferometer design should be with the feature of multiple passes, and only use non-polarizing optics to reduce the cost.

In Chapter 4, 5 and 6, three different interferometer conceptual designs originating from the project are proposed. In order to fulfill the angular range requirement, all of the three interferometer conceptual designs are in types of double-pass or quadruple-pass. PGC demodulation scheme is considered as the phase detection approach for the interferometers.

4.1 Principle

Figure 4.1 shows the configuration of the Double-pass Lens-based Interferometer (DLI) [41]. The principle is illustrated in geometric optics with paraxial approximation. The light source emitted by a laser diode transmits through a SMF and exits from a collimator (input). The collimated beam parallel to the optical axis is focused on the right surface of an optical window by a convex lens. Both the window and the lens are on the optical axis. A fraction of the beam is reflected at the glass-air interface, then defocused by the lens, and collected as the reference beam by a collimator (output). The majority of the beam transmits through the right surface of the window and then is defocused by the second convex lens on axis, so that the wavefront of the beam becomes planar again and the propagation direction is parallel to the optical axis. A mirror (regarded as the measured target) is supposed to be perpendicular to the beam. After being reflected by the mirror, the beam is reflected and focused by the second lens. A fraction of the beam is reflected at the air-glass interface on the right surface of the window and then defocused by the second lens. After being reflected by the mirror, the beam is parallel to the optical axis. After being focused and defocused by the two lenses, the beam is parallel to the optical axis again and collected as the measurement beam by the collimator (output). A photodetector is connected to the collimator (output) through a fiber.

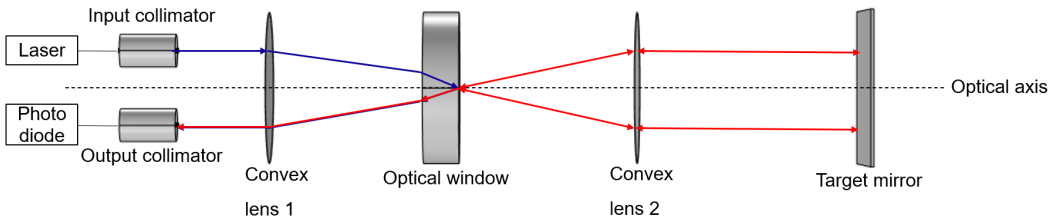

Figure 4.1: Schematic view of the double-pass lens interferomter. Reflections from the left surface of the optical window and higher order reflections are not drawn but have been investigated in Appendix B.

4.2 Feasibility analysis

The DLI uses an optical window as an interface creating the reference beam and a two lens system as a retroreflector. Because of this design, the distance between the rear surface of the optical window and the second lens is a part of the deadpath in the design. Due to the double-pass design, the reference and measurement beams have walk-off when the target mirror is tip-tilted, which limits the angular range. The beam walk-off has to be calculated to check if the angular range is fulfilled. The beam area on the target mirror can be found considering the symmetry of a two lens system. Potential ghost reflections should be investigated for the PNL error requirement.

Remarkably, in the DLI the beams are not on-axis but separated in the two sides of the optical axis. Lens aberrations make the paraxial rays and marginal rays go through slightly different paths. The wavefront error resulted from lens aberrations degrades the modulation depth of interference signal, and it might also be falsely interpolated as the target movement when the wavefront error changes. The lens aberration should be firstly investigated.

To build the optical system of the DLI and calculate the wavefront aberration, sequential models are built in ZEMAX. Different types of convex lenses are used for simulations: plano-convex spherical lens, bi-convex lens, achromatic doublets. The lenses and the optical window data sheets are listed in Appendix E.6. Effective focus length f = 30 mm and f = 100 mm doublets are used for simulations. Figure 4.2 shows the configurations of the DLI optical system. The source field is a flat wave with D_{aper} = 14.5 mm circular aperture. The distance between the lens and the optical window is a variable optimized by the software, so that the RMS of the wavefront on the image plane (located at infinity in the afocus system) is minimized. Figure 4.3 shows the corresponding wavefront maps on the image plane. Figure 4.4 shows the corresponding optical path differences of rays compared to the chief rays. Table 4.1 concludes the simulation results.

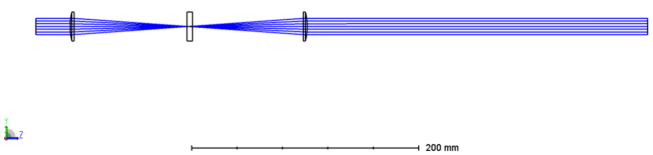

(a) Configuration of the DLI optical system using two plano-convex lens and one optical window.

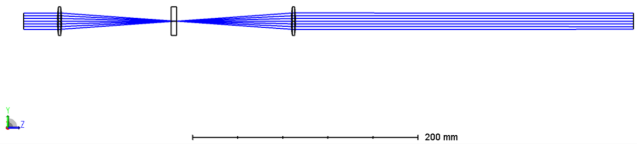

(b) Configuration of the DLI optical system using two bi-convex lens and one optical window.

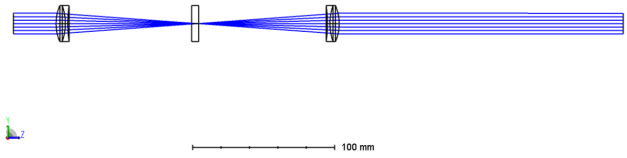

(c) Configuration of the DLI optical system using two doublets and one optical window.

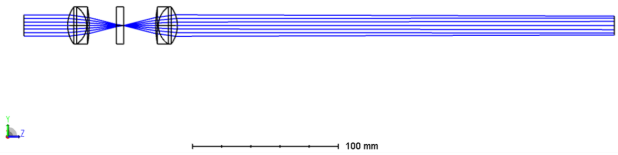

(d) Configuration of the DLI optical system using two doublets and one optical window.

Figure 4.2: Configurations of the DLI optical system using different combinations of lenses and the same optical window. The specifications of the lenses and the window is listed in Appendix E.6 and E.7 respectively.

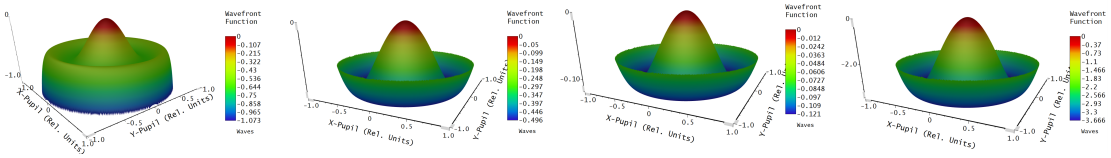

(a) The optimized wavefront on the image plane in the plano-convex lens configuration.

(b) The optimized wavefront on the image plane in the bi-convex lens configuration.

(c) The optimized wavefront on the image plane in the f = 100 mm doublets configuration.

(d) The optimized wavefront on the image plane in the f = 30 mm doublets configuration.

Figure 4.3: The optimized wavefront on the image plane in different configurations. The image plane is located at infinity since it is an afocal system. The physical diameter of the pupil is 14.5 mm.

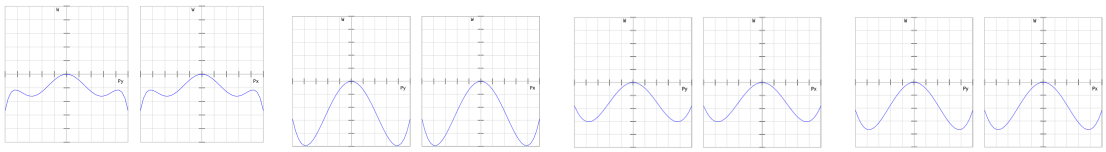

(a) The optical path length with respect to the chief ray on the image plane in the plano-convex lens configuration. The maximum scale of optical path length in the plot is $\pm$ **2** waves.

(b) The optical path length with respect to the chief ray on the image plane in the bi-convex lens configuration. The maximum scale of optical path length in the plot is $\pm$ **0.5** waves.

(c) The optical path length with respect to the chief ray on the image plane in the f = 100 mm doublets configuration. The maximum scale of optical path length in the plot is $\pm$ **0.2** waves.

(d) The optical path length with respect to the chief ray on the image plane in the f = 30 mm doublets configuration. The maximum scale of optical path length in the plot is $\pm$ **5** waves.

Figure 4.4: The optical path length with respect to the chief ray on the image plane in different configurations. The image plane is located at infinity since it is an afocal system. The physical diameter of the pupil is 14.5 mm.

Table 4.1: The peak to valley and RMS wavefront error values in different configurations

Configuration	**Peak to Valley** [λ]	**RMS** [λ]
Plano-convex f = 100 mm	1.0726	0.1699
Bi-convex f = 100 mm	0.4957	0.1301
Doublets f = 100 mm	0.1211	0.0308
Doublets f = 30 mm	3.6656	0.9505

A further simulation aimed to investigate how the wavefront error degrades the interference is done on the doublets with f = 30 mm configuration. The wavefront map information behind the second lens is shown in Subfigure 4.3d, the phase of which is exported and used as the phase information for the measurement beam. Figure 4.5 shows the f = 30 mm doublets configuration, in which only the reference beam path is considered. The source field is a flat wave with D_{aper} = 14.5 mm circular aperture. The distance between the first lens and the optical window is a variable optimized by the software, so that the RMS of the wavefront on the

image plane (located at infinity in the afocus system) is minimized. Figure 4.6 and 4.7 show the corresponding wavefront and optical path map respectively. The wavefront map in Figure 4.6 is exported and used as the phase information for the reference beam.

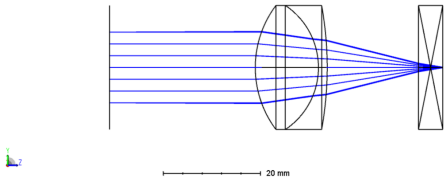

Figure 4.5: The f = 30 mm doublets configuration with only the first lens and the optical window. The reflection from the backside of the optical window is considered, so that the reference beam is obtained.

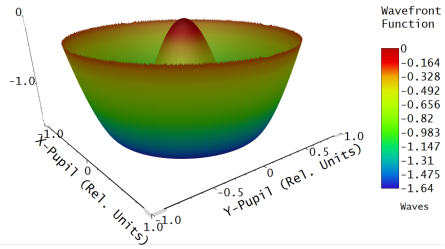

Figure 4.6: The optimized wavefront on the image plane in the f = 30 mm doublets configuration with only the first lens and the optical window.

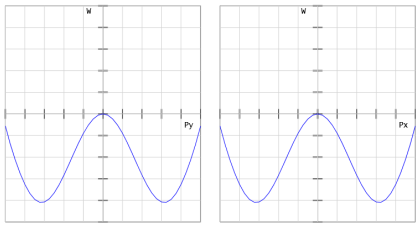

Figure 4.7: The optical path length with respect to the chief ray on the image plane in the f = 30 mm doublets configuration with only the first lens and the optical window. The maximum scale of optical path length in the plot is $\pm$ **2** waves.

The wavefront map can be used to simulation the interference signal. First the beam walk-off is not taken into considerations. The interference patterns when the reference and the measurement beams have 3 mm and 6 mm offset with respect to the optical axis are shown in Subfigure 4.8a and 4.8b respectively. Although the beams should not be on-axis, the interference patterns of on-axis beams are shown in Subfigure 4.8c for a reference. Figure 4.9 shows the corresponding irradiance with respect to the phase difference sweeping in one period.

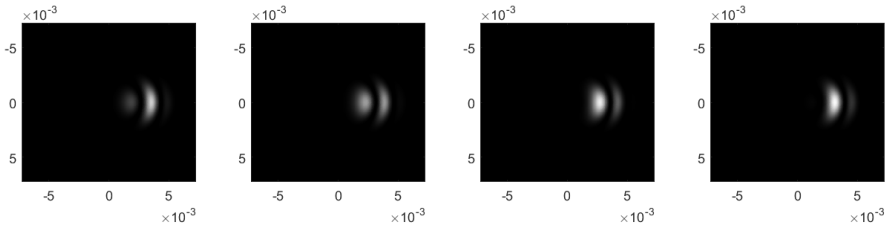

(a) The irradiance plot when the center of the reference and the measurement beams are 3 mm offset to the optical axis. From the left to the right figure, the phase differences of the two are 0, $\frac{\pi}{2}$, π, $\frac{3\pi}{2}$ respectively.

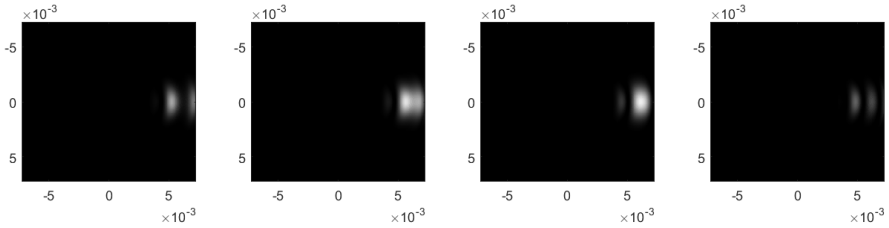

(b) The irradiance plot when the center of the reference and the measurement beams are 6 mm offset to the optical axis. From the left to the right figure, the phase differences of the two are 0, $\frac{\pi}{2}$, π, $\frac{3\pi}{2}$ respectively.

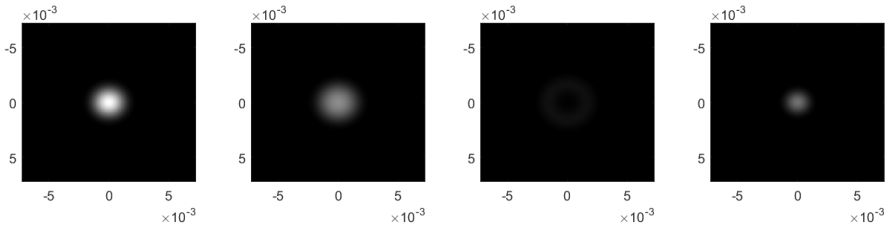

(c) The irradiance plot when tthe reference and the measurement beams are on-axis. From the left to the right figure, the phase differences of the two are 0, $\frac{\pi}{2}$, π, $\frac{3\pi}{2}$ respectively.

Figure 4.8: The irradiance of the interference pattern plotted in grey scale. The unit of the axes is meter.

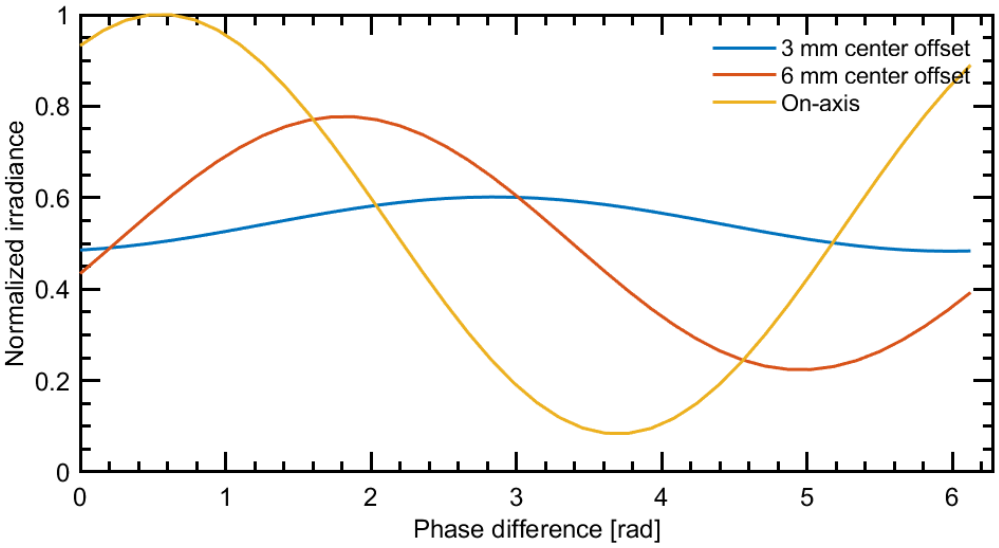

Figure 4.9: The irradiance with respect to the phase difference between the reference and the measurement beams.

Figure 4.9 shows the wavefront error degrades the interference in two ways:

1. Strength and modulation depth loss
   Comparing the three curves, the on-axis curve has the largest signal strength and modulation depth. In Subfigure 4.4d and 4.7, the slope is relatively small near the optical axis and around the area with a radius of 6 mm, and the slope in between is relatively large, which can explain why the 6 mm offset result has larger signal strength and modulation depth than the 3 mm offset. The radius of the small slope ring can be derived from the spherical aberration term. This radius can be designed for the location of the beam input.

2. Phase drift
   When the phase difference is 0, a constructive interference should be obtained. A slight phase drift is observed in the on-axis curve, and intensive phase drifts are observed in the offset curves. In displacement interferometry this effect itself does not become an issue as the displacement is extracted from the relative phase change when the target moving. But it introduces a measurement error with the presence of a beam walk-off, which will be shown in Figure 4.11.

When the target is tip-tilted, the beam walk-off will further degrade the interference. The interference patterns when the reference has 3 mm and 6 mm offset with respect to the optical axis are shown in Subfigure 4.10a and 4.10b respectively, where the measurement beam has 1.8 mm extra offset due to the beam walk-off. Figure 4.11 shows the corresponding irradiance with respect to the phase difference sweeping in one period.

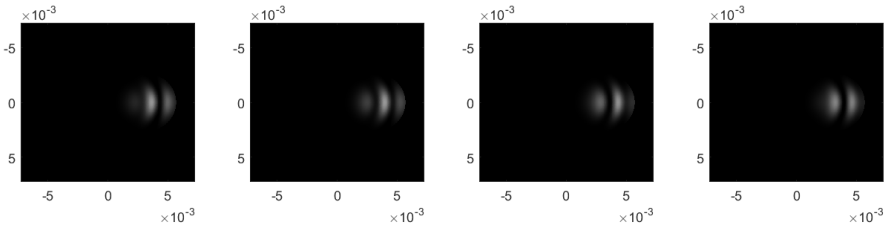

(a) The irradiance plot when the center of the reference is 3 mm offset to the optical axis and the measurement beam is 4.8 mm offset to the optical axis. From the left to the right figure, the phase differences of the two are 0, $\frac{\pi}{2}$, π, $\frac{3\pi}{2}$ respectively.

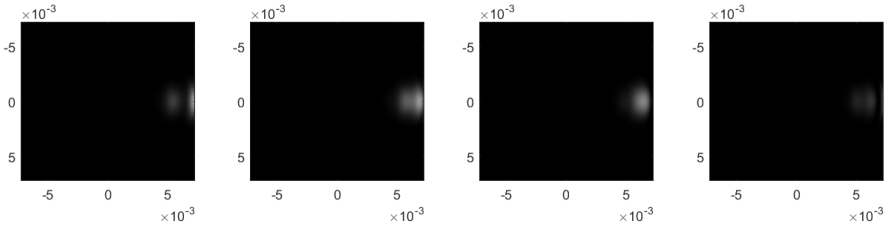

(b) The irradiance plot when the center of the reference is 6 mm offset to the optical axis and the measurement beam is 4.8 mm offset to the optical axis. From the left to the right figure, the phase differences of the two are 0, $\frac{\pi}{2}$, π, $\frac{3\pi}{2}$ respectively.

Figure 4.10: The irradiance of the interference pattern plotted in grey scale. The unit of the axes is meter.

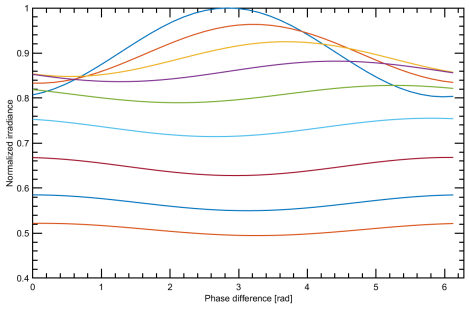

(a) The irradiance with respect to the phase difference when the center of the reference is 3 mm offset to the optical axis and the measurement beam is from 3 mm offset to 6.6 mm offset to the optical axis. When the measurement beam is 3 mm offset to the optical axis the corresponding curve reaches the maximum normalized irradiance 1. The maximum irradiance and modulation depth keep dropping when the measurement beam offset increases.

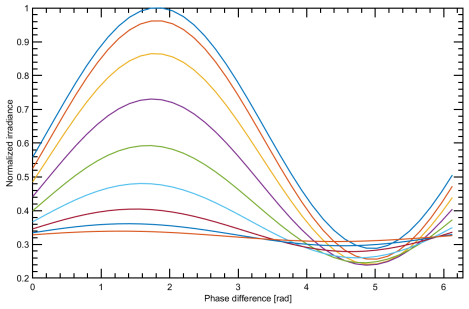

(b) The irradiance with respect to the phase difference when the center of the reference is 3 mm offset to the optical axis and the measurement beam is from 6 mm offset to 9.6 mm offset to the optical axis. When the measurement beam is 6 mm offset to the optical axis the corresponding curve reaches the maximum normalized irradiance 1. The maximum irradiance and modulation depth keep dropping when the measurement beam offset increases.

Figure 4.11: The irradiance with respect to the phase difference between the reference and the measurement beams.

Subfigure 4.11a shows a dramatic modulation depth loss when the beam walk-off increases. Subfigure 4.11b shows a relatively slow modulation depth loss when the beam walk-off increases. The phase drift is observed in both plots. It does not introduce an error when the target mirror orienting at the same direction, but if the target mirror deviates from its initial angle, this phase drift will be falsely interpolated as a target displacement.

The above interference simulations are based on the optimized wavefront information of the f = 30 mm doublets configuration. In reality, due to manufacturing limits, material thermal expansions and air refractive index changes, the wavefront error can be larger than the one used in the simulations.

Table 4.1 shows a smaller wavefront error in the f = 100 mm doublets configuration, which means that the aforementioned problems of signal modulation depth loss and phase drift will be mitigated. Without checking the interference simulation results on the f = 100 mm doublets configuration, the configuration is not feasible considering the minimum axial length of it is 200 mm ($2f$). Although there is no volume requirement in the project goal, considering the available mounting room for the interferometer head in the lithography machine, the large volume interferometer design is rejected by ASML. Increasing the focus length of the lens can reduce the wavefront error, but it is not the feasible method to solve the problem.

Table 4.1 shows the doublets configuration has less wavefront error than the plano-convex and the bi-convex lens configurations, which means the wavefront error can be reduced by optimizing the lens design. Doublets is a combination of two lenses that has partially eliminated aberrations. In order to minimize the wavefront error and the system volume, it is necessary to optimize and customize the lens with small aberration and small focal length, which increases the design cost and manufacturing cost. In conclusion, the DLI design is not feasible.
the aberration problem

The risk of aberration is emphasized and it is proved that the DLI design is not feasible due to the large wavefront error using standard lenses. The other specs of the DLI such as the dead-path, angular range, beam area size on the target and PNL error are still worth an investigation to see if the benefits overcome the high design and manufacturing cost of the lens. The relevant content is in Appendix B.

4.3 Conclusion

Based on the analysis in this chapter, it is concluded that the DLI has the following advantages and disadvantages:

- **Advantages**

    1. The lenses and optical window are on-axis, so that they are easy to mount and align.
    2. The target velocity factor NoP of a double-pass interferometer is smaller than a quadruple-pass interferometer, which results in a larger permissible velocity in the PGC detection approach.

- **Disadvantages**

    1. The lenses have to be well optimized to reduce the aberration and the volume of the system.

2. The reference and measurement beams have walk-off when the target mirror is tip-tilted, which limits the angular range.
3. The minimum deadpath is limited by the focal length of the second convex lens.
4. The deadpath lengths of the reference and the measurement beam are not balanced, which results in errors when temperature changes.
5. The target displacement factor $\frac{1}{NoP}$ of a double-pass interferometer is larger than a quadruple-pass interferometer, which means a coarser displacement resolution.

The concept of DLI is not feasible mainly due to the risk of aberration. No design example is given here.

Chapter 5

Quadruple-pass Interferometer

5.1 Principle

Figure 5.1 shows the configuration of the Quadruple-pass Interferometer (QI) [42]. The light source emitted by a laser diode enters from port 1 of a single-mode optical circulator, and then exits from the collimator connected to port 2. This collimated beam then passes through an uncoated wedge prism, and the exit beam is perpendicular to the right surface of the wedge prism. The uncoated condition means that both the left and right surfaces of the wedge prism produce natural reflections at their interfaces. The perpendicular condition means that only the reflected light from the right surface can travel back to the collimator, enter from port 2 of the circulator, and exit from port 3 connected to a photodetector. This reflected light from the right surface of the wedge prism is the reference beam. After passing through the wedge prism, the beam is reflected to a CCR by a mirror (regarded as the measured target) at a small angle. This small tilted angle of the target mirror is intentional, which makes sure that the reflected beam does not go back to the collimator, but goes to the CCR mounted next to the collimator. Since the exit beam of the CCR is parallel to the incident beam, the beam strikes the right surface of the wedge prism at 90° after being reflected by the mirror again. At the air-glass interface, a fraction of the light is reflected at 90°, which becomes the measurement beam. Because of the 90° reflection the beam will exactly retrace its path all the way to the collimator. After going through the mirror-CCR-mirror path again, the beam walk-off is automatically corrected. The measurement beam finally enters the collimator and is collected by the photodetector. This conceptual design is called a quadruple-pass interferometer since the measurement beam travels four times the (round-trip) path between the wedge prism and the mirror.

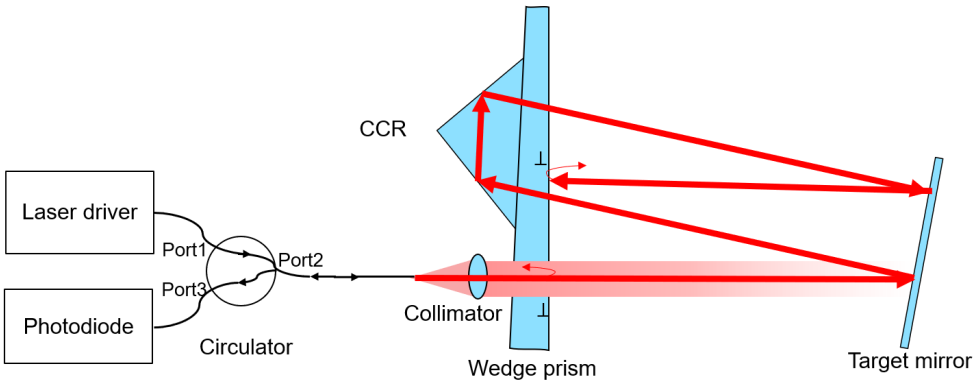

Figure 5.1: Schematic view of the quadruple-pass interferomter. The ⊥ symbol indicates where the beam is perpendicular to the surface of the wedge prism.

5.2 Feasibility analysis

The principle of the QI ensures that the reference and measurement beams have no walk-off or angular deviation. The feasibility research is to check whether the QI can meet the requirements of the measurement range, angular range, size of the beam area on the target.

Figure 5.2 shows the lateral view of the QI. The red lines indicate the beam path when the target mirror is at the minimum measurement position (i.e. the deadpath of the interferometer). The green lines indicate the beam path when the target mirror is at the maximum measurement position. When the target is at different positions, the beam reflected by the target will enter the CCR at different positions. The shifting distance is referred as the distance that the beam entering position at the CCR is shifted when the target is moving over the entire measurement range. Unless the beam strikes exactly the vertex of the CCR, the exit position of the beam will be different from the incident position. For those incident beams normal to the CCR entrance, the incident and exit positions are symmetric around the center of the entrance of the CCR [43]. The beam exiting the CCR is reflected by the target mirror at a different position than its first reflection. By analyzing this scenario, the following design variables are given with their effects on the QI:

- s : the distance between the entrance of the CCR and the target. The distance when the target is at the minimum measurement position is denoted as s_{min}.

- θ : the intentional tilted angle of the target (marked as 2θ in Figure 5.2 due to reflection). This variable together with s determines where the beam strikes the CCR. The larger θ, the larger the shifting distance.

- x_{sor} and y_{sor} : the distance between the source beam from the collimator and the vertex of the CCR in two orthogonal directions.
  This variable together with s and θ determines where the beam exits from the CCR. x_{sor} and y_{sor} can be expressed using horizontal and vertical components respectively, viewed from a plane perpendicular to the beam and the CCR. The beam shifts make the beams re-

flected at the target at different positions over the entire measurement range. All possible positions of the beam on the target should be limited to the specified beam area 20 mm×8 mm.

- D_{CCR} : the diameter of the CCR.
  This variable limits the range of positions of all beams entering and exiting the CCR. There are a few diameter options for an off-the-shelf CCR, e.g., 12.7, 25.4 and 50.0 mm. To minimize the beam deviation between the incident and reflected beams, it is considered to limit the beams within the Clear Aperture (CA) of a CCR. The diameter of the CA is typically 70% of the diameter of the CCR [44] but varies depending on the manufacturing process.

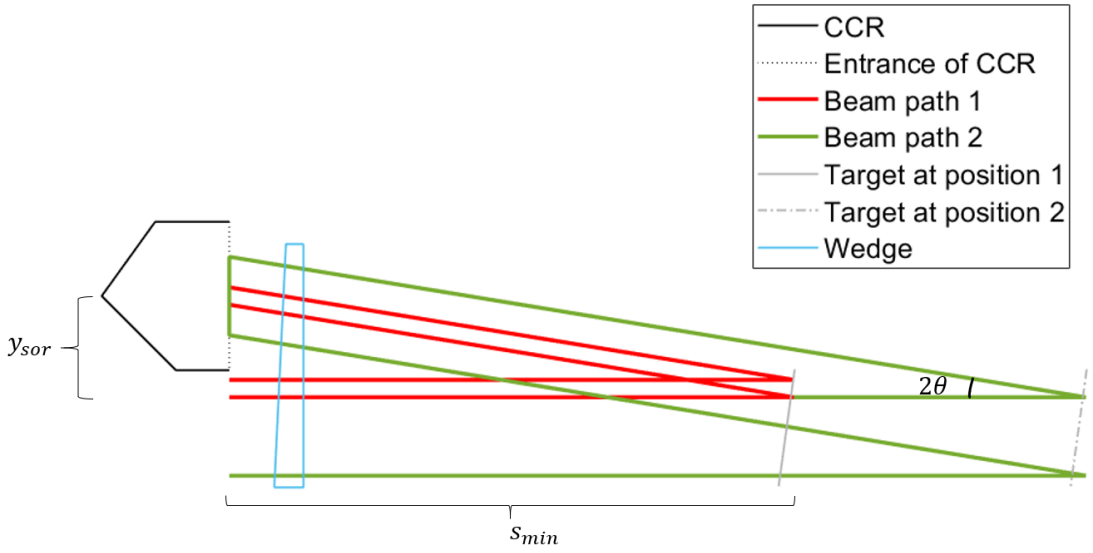

Figure 5.2: A lateral view of the QI with some key design variables marked. The scale is not corresponding to the realistic dimensions of the QI.

These variables need to be assigned a set of values to meet design requirements and avoid risks. In the set of a solution $[s_{min}, \theta, x_{sor}, y_{sor}, D_{CCR}]$ satisfying all the requirements, s_{min} represents the deadpath of the QI. Section 3 has shown that the deadpath is a critical parameter to minimize. Thus, the design problem is to find the set of design variables that minimizes s_{min} and satisfies all the requirements. The design problem can be formulated as an optimization problem and the solution can be found as the optimum satisfying all the constraints. The following Subsection 5.2.1 and 5.2.2 formulate the design problem into optimization problems and solve them.

5.2.1 Base model

For the design of the QI model first only off-the-shelf optical elements are considered. The choice of D_{CCR} will be thus be limited to 12.7, 25.4 and 50.0 mm. For each D_{CCR}, a set of op-

timal design variables $[s_{min}, \theta, x_{sor}, y_{sor}]$ will be determined and the best option of D_{CCR} will be chosen later. Based on the analysis of the design variables and their effects, an optimization problem can be formulated to find the set of design variables that minimizes the objective function and satisfies all the constraints. The optimization problem is formulated in the following method:

1. **Objective function**
   The objective function $f(\mathbf{x})$ is chosen as the ratio of the minimum measurement position and the maximum measurement position. Formulating the objective function in this way has the advantages of weighting the function based on the measurement range and not changing the monotonicity in the meantime. The function should be minimized with respect to the design variables $\mathbf{x}$.

2. **Design variable**
   The design variables are the key features marked in Figure 5.2.

   To calculate the values of the design variables, a right-handed coordinate system is established with the vertex of the CCR as the origin, the direction of the source beam after transmitting the wedge as the +z axis, the horizontal right direction in the plane perpendicular to the +z axis as the +x axis. Figure 5.3 directly shows the orientation of the coordinate system. With the coordinate system defined, the design variable d can be expressed by the position $[x_{sor}, y_{sor}, 0]$ of $\mathbf{P_{sor}}$ marked in Figure 5.3.

   The design variables are $\mathbf{x} = [x_{sor}, y_{sor}, s_{min}, \theta]$. Using the design variables, the positions of other points can be expressed. The result is shown in Table 5.1.

Table 5.1: Positions of the evaluated points expressed by design variables. s_{meas} is a constant representing the required measurement range.

Point	x (P)	y (P)
$\mathbf{P_{sor}}$	x_{sor}	y_{sor}
$\mathbf{P_1}$	x_{sor}	$y_{sor} + 2s_{min}\theta$
$\mathbf{P_{1'}}$	x_{sor}	$y_{sor} + 2\left(s_{min} + s_{meas}\right)\theta$
$\mathbf{P_3}$	-x_{sor}	$-y_{sor} - 4s_{min}\theta$
$\mathbf{P_{3'}}$	-x_{sor}	$-y_{sor} - 4\left(s_{min} + s_{meas}\right)\theta$

3. **Constraint**
   There are several constraints that the design variables need to be objected to:

   - g_1
     The origin of the source beam $\mathbf{P_{sor}}$ should not physically overlap with the CCR. The collimator cannot be mounted inside the CCR without extra manufacturing efforts.

   - g_2 and g_3
     All the beams entering and exiting the CCR should be within the CA. Otherwise, the beam deviation between the incident and reflected beams is not minimized. It is sufficient to only check this condition for $\mathbf{P_1}$ and $\mathbf{P_{1'}}$ as indicated in Figure 5.3, since the position for all other beams is completely defined by the position of these two beams. The angular range requirement can be considered in this condition.

- g_4
  The shifting distance should be no more than the required size of the beam area on the target.

- g_5
  All the second-pass beams should be outside the CCR. Otherwise, the second-pass beams will be reflected by the CCR and the wedge again. This reflection spoils the interference signal, since it is a ghost reflection with the intensity close to the measurement beam. This can result in large PNL error up to 61 nm, which is derived in Section 5.3. It is sufficient to just check this condition for $\mathbf{P_3}$ in Figure 5.3, as other second-pass beams will lie further away from the CCR.

- g_6
  Due to the PGC phase detection limit, the ratio of the optical path difference at the maximum and minimum measurement distance should be within the range from 2.5 to 6.

- Bound formulation
  Due to the symmetry, the values of x_{sor} and y_{sor} are specified as non-positive numbers, the value of θ is specified as non-negative number. In addition, the value of x_{sor} should be less than $\frac{D_{beam}}{2}$.

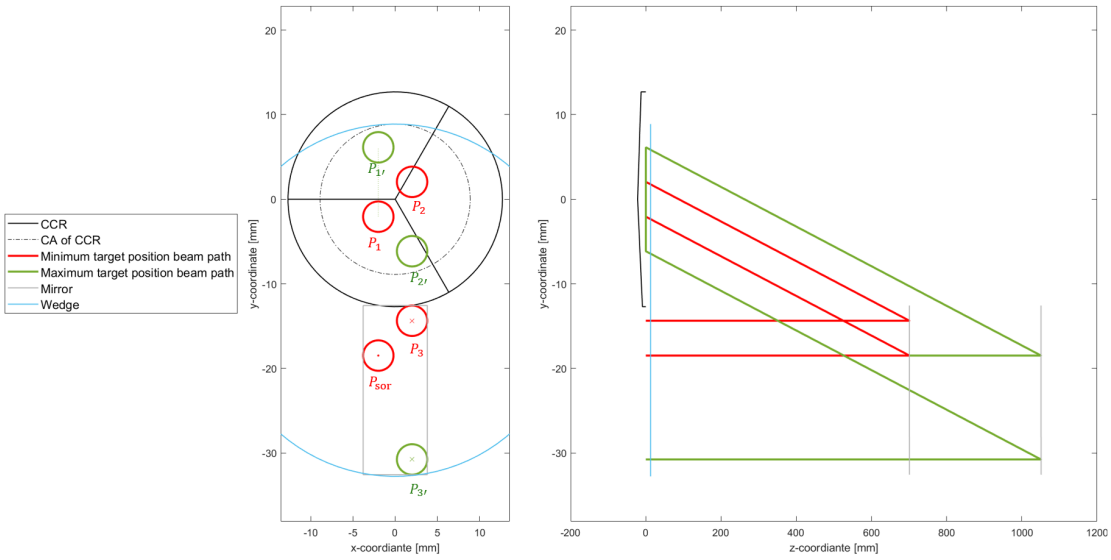

Figure 5.3: The views of the QI in xy-plane and yz-plane. The y-coordinates are matched in the two views. The view in xy-plane uses the same axis scale, but the view in yz-plane view uses different axis scales due to long measurement distance compared to other dimensions in y-axis. The view in xy-plane emphasizes the positions where the beams reach the CCR entrance, and the size of the beam is indicated by a circle. "·" within the circle indicates that the corresponding beam direction is along the +z-axis, "×" within the circle indicates that the corresponding beam direction is along the -z-axis. The view in yz-plane emphasizes the beam paths without indicating the beam size.

With the problem described, the optimization problem can be formulated by the negative null

form with scaling of all constraints:

$$
\begin{aligned}
\min_{\mathbf{x}} f(\mathbf{x}) &= \frac{s_{min}}{s_{min} + s_{meas}} \\
\text{subject to: } g_1(\mathbf{x}) &= -\frac{\|\mathbf{P_{sor}}\|}{\frac{D_{CCR}}{2} + \frac{D_{beam}}{2}} + 1 \leq 0 \\
g_2(\mathbf{x}) &= \frac{\|\mathbf{P_1}\|}{\frac{0.7\,D_{CCR}}{2} - \frac{D_{beam}}{2}} - 1 \leq 0 \\
g_3(\mathbf{x}) &= \frac{\|\mathbf{P'_1}\|}{\frac{0.7\,D_{CCR}}{2} - \frac{D_{beam}}{2}} + 1 \leq 0 \\
g_4(\mathbf{x}) &= \frac{4\,s_{meas}\,\theta}{L_{mir} - D_{Beam}} - 1 \leq 0 \\
g_5(\mathbf{x}) &= -\frac{\|\mathbf{P_3}\|}{\frac{D_{CCR}}{2} + \frac{D_{beam}}{2}} + 1 \leq 0 \\
g_6(\mathbf{x}) &= \frac{1.5 s_{min}}{s_{meas}} - 1 \leq 0 \\
x_{sor} &\leq -\frac{D_{beam}}{2} \\
y_{sor} &\leq 0 \\
\theta &\geq 0
\end{aligned}
\tag{5.1}
$$

The system of equations represents a constrained non-linear problem. The objective function and constraints are twice continuously differentiable. Therefore, sequential quadratic programming is chosen as the solving algorithm, which is realized by using the Matlab function `fmincon` in Appendix C.1. The required measurement range is 350 mm, the beam diameter D_{beam} is 3.6 mm given by the specs of the used collimator, three typical diameter values (12.7, 25.4 and 50.0 mm) of the standard CCR are used for searching solutions. The solutions given by the script are listed in Table 5.2. The Lagrange multipliers indicate which constraints are active, with a non-zero value indicating an active constraint.

Table 5.2: Optimization results with different diameters of the CCR.

D_{CCR}	**Optimized $\mathbf{P_{sor}}$**	**Optimized s_{min}**	**Optimized θ**	**Lagrange multiplier**
12.7	No feasible solution found			
25.4	(-2,-18.48)	700.8	0.0117	[0, 0, 0.2035,0.0944, 0.1142, 0]
50	(-2,-26.73)	1141	0.0117	[0.0903, 0, 0.0903, 0, 0.1797, 0]

The CCR with 25.4 mm diameter gives the smallest s_{min}. The Lagrange multipliers indicate the active constraints are g_3, g_4 and g_5. Figure 5.3 is scaled to the solution, from which the active constraints can be visualized: the beam represented by $\mathbf{P_{1'}}$ will remain within the CA for any position of the target mirror, including the specified target mirror angular misalignment of up to $\pm$ 300 µrad. The beam represented by $\mathbf{P_3}$ is outside and close to the CCR, the beams represented by $\mathbf{P_{sor}}, \mathbf{P_3}$ and $\mathbf{P'_3}$ make use of the area of 20 mm$\times$8 mm on the target mirror. The CCR with 50 mm diameter gives another feasible solution but with larger s_{min}. The Lagrange multipliers indicate the active constraints are g_1, g_3 and g_5. Figure 5.4 is scaled to the solution, from which the active constraints can be visualized: the beams represented by $\mathbf{P_{sor}}$ and $\mathbf{P_3}$ are outside and

close to the CCR, the beam represented by $\mathbf{P}_1'$ is within the CA. The constraint of the beam area size on the mirror is inactive in this case. The following conclusions can be drawn from the base model optimization problem research:

- Choosing the standard CCR with 25.4 mm diameter minimizes the deadpath of the QI. To further decrease the deadpath, one simple approach is to make the size of beam area on the target mirror larger. Since the constraint of the beam area size is defined by the design requirements, the result of enlarging the beam area size is only shown in Appendix C.2.
- Choosing a 12.7 mm diameter CCR does not satisfy the required measurement range and angular range. Choosing a 50 mm diameter CCR makes the minimum measurement distance larger. This indicates that the diameter of the CCR should not be too large or too small. An optimum might be found between 12.7 and 50 mm besides 25.4 mm. The value of the optimized CCR diameter is not interested in the base model research, but will be discussed in the advanced model research in Subsection 5.2.2.
- Eliminating constraint g_5 by positioning the wedge prism is a feasible solution. It end up with a solution using a 38.74 mm diameter wedge prism. Detailed discussion on the solution of positioning the wedge prism is in Appendix C.3.

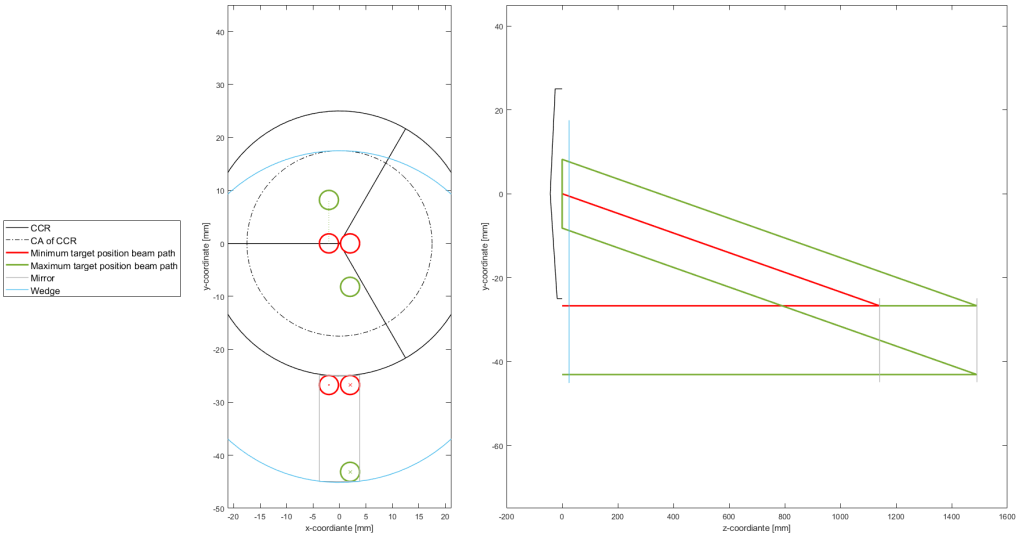

Figure 5.4: The views of the QI in xy-plane and yz-plane using a 50 mm diameter CCR and the corresponding solution in Table 5.2.

5.2.2 Advanced model

In the QI advanced model analysis, uses of customized elements are taken into consideration. Thus D_{CCR} is no longer chosen among 12.7, 25.4 and 50.0 mm, but it will also be considered as a design variable. The design variables in the advanced model is thus $\mathbf{x} = [D_{CCR}, x_{sor}, y_{sor}, s_{min}, \theta]$. The base model analysis in Subsection 5.2.1 has shown several optimization results and how the constraints affect the results. Based on the base model research, the following improvements can be made considering using customized elements:

- In Equation 5.1, g_1 can be eliminated by drilling a hole to mount the collimator inside the CCR. The cost will be expensive.
- Instead of choosing the CCR diameter among standard options, the optimum value of the CCR diameter can be solved.
- The wedge positioning approach shown in Appendix C.3 eliminating the ghost reflection constraint g_5 has been applied in the base model research. But the newly introduced constraint explained in Appendix C.3 still limits the deadpath strictly. Applying an anti-reflective (AR) coating on the particular area of the wedge prism can prevent potential ghost reflections. To identify the particular area on the wedge where an AR coating can eliminate ghost beams, additional attention should be paid to the beam path of the ghost beam. Covering too large of an area with AR coating will also degrade the quality of the measurement beam, so knowing the exact bounds within which the ghost beam stays is very important in identifying the AR coating area. What's more, the AR coating only prevents the reflection of the second-pass beam, the transmission part of the second-pass beam should also be investigated.

Based on these points, the new optimization problem for the advanced model can be formulated by the negative null form with scaling of all constraints:

$$\begin{aligned}
\min_{\mathbf{x}} f(\mathbf{x}) &= \frac{s_{min}}{s_{min} + s_{meas}} \\
\text{subject to: } g_1(\mathbf{x}) &= \frac{\|\mathbf{P_1}\|}{\frac{0.7\,D_{CCR}}{2} - \frac{D_{beam}}{2}} - 1 \leq 0 \\
g_2(\mathbf{x}) &= \frac{\|\mathbf{P_1'}\|}{\frac{0.7\,D_{CCR}}{2} - \frac{D_{beam}}{2}} + 1 \leq 0 \\
g_3(\mathbf{x}) &= \frac{4\,s_{meas}\,\theta}{L_{mir} - D_{Beam}} - 1 \leq 0 \\
g_4(\mathbf{x}) &= \frac{-2\,s_{min}\,\theta}{D_{beam}} + 1 \leq 0 \\
g_5(\mathbf{x}) &= \frac{-\|\mathbf{P_{ghostr}}\|}{\frac{D_{CCR}}{2} + \frac{D_{beam}}{2}} + 1 \leq 0 \\
g_6(\mathbf{x}) &= \frac{1.5 s_{min}}{s_{meas}} - 1 \leq 0 \\
x_{sor} &\leq -\frac{D_{beam}}{2} \\
y_{sor} &\leq 0 \\
\theta &\geq 0
\end{aligned} \tag{5.2}$$

Where $\mathbf{P_{ghostr}}$ represents the ghost reflection marked in Figure 5.5 with its position of $(x_{sor}, y_{sor} + 6\,(s_{min} + s_{meas})\,\theta)$. Using Matlab function `fmincon` and the script in Appendix C.4, the solution is listed in Table 5.3 and illustrated in Figure 5.5.

Table 5.3: Optimization results with different diameters of CCR.

D_{CCR}	**Optimized $\mathbf{P_{sor}}$**	**Optimized s_{min}**	**Optimized θ**	**Lagrange multiplier**
19.04	(-2, -11.90)	327.8	0.0117	[0.0128, 0.0950, 0.0983, 0, 0.1905, 0]

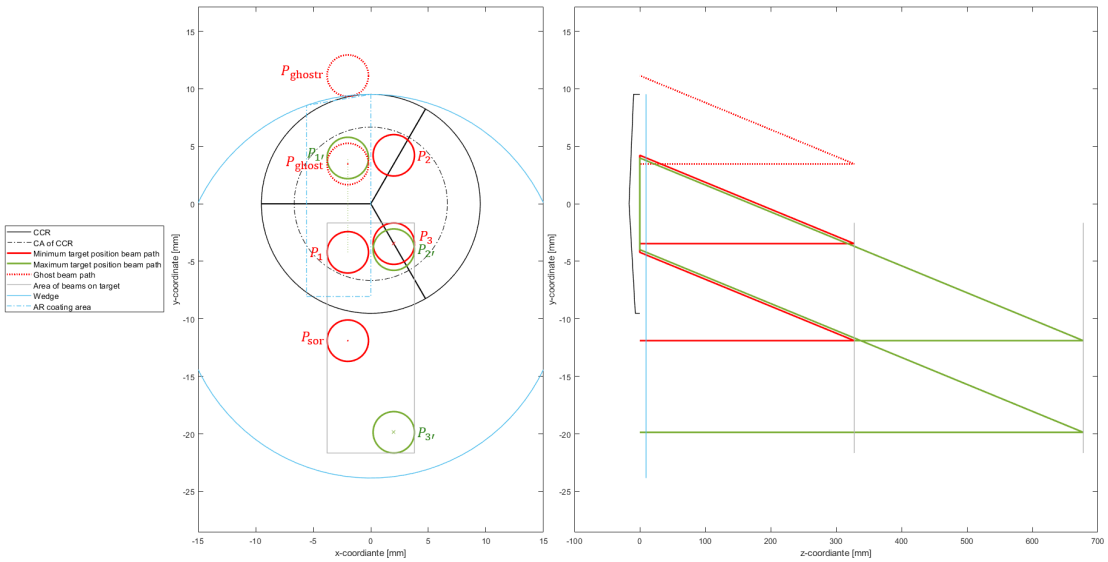

Figure 5.5: The views of the QI in xy-plane and yz-plane. The corresponding solution of the illustration is in Table 5.3. When the target is at the minimum measurement distance, the path of the ghost beam is represented by red dashed lines in the two views. $\mathbf{P_{ghost}}$ represents the exit beam of $\mathbf{P_3}$. Since it is perpendicular to the wedge prism, a ghost beam will be created if there is no anti-reflective coating on that area of the wedge prism. The beam represented by $\mathbf{P_{ghost}}$ exits the CCR, transmits through the wedge prism, and is reflected by the target mirror (the grey lines in the yz-plane view only represents the area of all desired beams on the target, but the actual target mirror can be regarded as a plane). The reflected ghost beam, represented by $\mathbf{P_{ghostr}}$ in the xy-plane view, does not go back into the CCR, thus it is not harmful anymore.

The Lagrange multipliers are non-zero for constraints g_1, g_2, g_3 and g_5, meaning these are active constraints. Although the beam area size on the target mirror is inactive in this solution, a larger beam area size corresponds to another optimum size of the CCR, which ends up with a smaller deadpath. Since the constraint of the beam area size is defined by the design requirements, the result of enlarging the beam area size is only shown in Appendix C.2.

5.3 PNL analysis

The QI only uses non-polarizing optics, thus there is no polarization leakage issue. The PNL error mainly originates from ghost reflections. The unacceptable ghost reflections have been taken into account and prevented in Section 5.2, which ensures the feasibility of the IFM concept. Although the QI base model and advanced model have given feasible designs, there are still ghost reflections in each model. The properties of the ghost reflections are researched in this section.

The measurement beam combines with the reference beam after four passes traveling. However, a fraction of the measurement beam is reflected at the air-glass interface of the right surface of the wedge prism at 90°, then travels another four passes, and finally mixes with the desired

reference and measurement beams. Multi-order ghost beams are generated every four passes, but the irradiance of the ghost beams decreases exponentially every four passes. Since the QI uses non-polarizing optics, general expressions for the electromagnetic fields of the reference, measurement and ghost beams along every polarization are:

$$\begin{aligned} E_r &= A_r e^{i(\,\omega t + k x_r + \phi_r)} \\ E_m &= A_m e^{i(\,\omega t + k x_m + \phi_m)} \\ E_g &= \sum_{n=2}^{\infty} A_{g_n} e^{i(\,\omega t + k x_{g_n} + \phi_{g_n})} \end{aligned} \tag{5.3}$$

Where the meanings of the symbols are:

- E_r, E_m, E_g: The electromagnetic fields of the reference, measurement, and summation of different order ghost beams respectively.
- A_r, A_m, A_{g_n}: The amplitudes of the electromagnetic field of the reference, measurement, and the nth-order ghost beam respectively. The order number n counts from 2, since the main ghost beam travels twice as many pass as the measurement beam.
- ω: The angular frequency of the beam.
- k: The wave number of the beam.
- x_r, x_m, x_{g_n}: The optical path lengths of the reference, measurement, and the nth-order ghost beam respectively.
- $\phi_r, \phi_m, \phi_{g_n}$: The initial phases of the reference, measurement, and the nth-order ghost beam respectively.

The total electromagnetic field is the linear superposition of each field. The irradiance without ghost reflections and with the nth-order ghost reflection at the detector is:

$$\begin{aligned} I_{ideal} &= c\varepsilon |\, E_r + E_m \,|^2 \\ &= c\varepsilon (\, A_r^2 + A_m^2 + 2A_r A_m \cos(\, k(\, x_m - x_r) + \phi_m - \phi_r)\,) \\ I_{g_n} &= c\varepsilon |\, E_r + E_m + E_{g_n} \,|^2 \\ &= c\varepsilon (\, A_r^2 + A_m^2 + 2A_r A_m \cos(\, k(\, x_m - x_r) + \phi_m - \phi_r) \\ &+ A_{g_n}^2 + 2A_r A_{g_n} \cos(\, k(\, x_{g_n} - x_r) + \phi_{g_n} - \phi_r) \; + 2A_m A_{g_n} \cos(\, k(\, x_{g_n} - x_m) + \phi_{g_n} - \phi_m)\,) \end{aligned} \tag{5.4}$$

Where c is the speed of the light, ε is the permittivity of the medium [45]. The OPD $x_m - x_r$ can be extracted using a quadrature phase detection method introduced in Subsection 2.3. The irradiance signal and its 90° phase shifted signal are detected, and the corresponding phase to the OPD is obtained from the arctangent of the two signals I_{S_0} and $I_{S_{90}}$ with DC removed:

$$\begin{aligned} \phi_{OPD} &= \arctan \frac{I_{S_{90}}}{I_{S_0}} \\ &= \arctan \frac{\sin(\, k(\, x_m - x_r))}{\cos(\, k(\, x_m - x_r))} \\ &= k(\, x_m - x_r)) \end{aligned} \tag{5.5}$$

The optical path length of the nth-order ghost beam travels $(n-1)$ time(s) more than the traveling distance of the measurement beam. Compared with the ϕ_{OPD} in Equation 5.5, x_{g_n} has the following properties in the QI:

$$\begin{aligned} n\,\phi_{OPD} &= k(x_{g_n} - x_r) \\ (n-1)\,\phi_{OPD} &= k(x_{g_n} - x_m) \end{aligned} \tag{5.6}$$

The PNL error resulted from the nth-order ghost reflection can be derived from Equation 5.4, 5.5 and 5.6:

$$\begin{aligned} \varepsilon_n &= \frac{1}{k\,NoP}\left(\arctan\frac{A_rA_m\sin(k(x_m-x_r)) + A_rA_{g_n}\sin(k(x_{g_n}-x_r)) + A_mA_{g_n}\sin(k(x_{g_n}-x_m))}{A_rA_m\cos(k(x_m-x_r)) + A_rA_{g_n}\cos(k(x_{g_n}-x_r)) + A_mA_{g_n}\cos(k(x_{g_n}-x_m))} - \dots \right. \\ &\quad \left. \arctan\frac{\sin(k(x_m-x_r))}{\cos(k(x_m-x_r))}\right) \\ &= \frac{1}{k\,NoP}\left(\arctan\frac{A_rA_m\sin(\phi_{OPD}) + A_rA_{g_n}\sin(n\phi_{OPD}) + A_mA_{g_n}\sin((n-1)\phi_{OPD}))}{A_rA_m\cos(\phi_{OPD}) + A_rA_{g_n}\cos(n\phi_{OPD}) + A_mA_{g_n}\cos((n-1)\phi_{OPD}))} - \dots \right. \\ &\quad \left. \arctan\frac{\sin(\phi_{OPD})}{\cos(\phi_{OPD})}\right) \\ &= \frac{1}{k\,NoP}\arctan\frac{\frac{A_{g_n}}{A_m}\sin((n-1)\phi_{OPD})) + \frac{A_{g_n}}{A_r}\sin((n-2)\phi_{OPD}))}{1+\frac{A_{g_n}}{A_m}\cos((n-1)\phi_{OPD})) + \frac{A_{g_n}}{A_r}\cos((n-2)\phi_{OPD}))} \end{aligned} \tag{5.7}$$

Where NoP = 8 for the QI. The simplification of Equation 5.7 uses some trigonometric identity transformations listed in Appendix C.5.

If the amplitude of the nth-order ghost beam is significantly less than the reference and measurement beam ($A_{g_n} \ll A_r, A_{g_n} \ll A_m$), Equation 5.7 can be simplified:

$$\varepsilon_n = \frac{1}{k\,NoP}\left(\frac{A_{g_n}}{A_m}\sin((n-1)\phi_{OPD}) + \frac{A_{g_n}}{A_r}\sin((n-2)\phi_{OPD})\right) \tag{5.8}$$

If the main order $n = 2$ ghost beam is considered only, Equation 5.8 is written as:

$$\varepsilon_2 = \frac{1}{k\,NoP}\frac{A_{g_2}}{A_m}\sin(\phi_{OPD}) \tag{5.9}$$

Equation 5.9 indicates that the amplitude of the PNL error resulted from the 2nd-order ghost beam can be estimated using the information of $\frac{A_{g_2}}{A_m}$. An estimation is performed considering the 2nd-order ghost beam experiences twice more reflection at the right surface of the wedge prism and twice more transmission at the specular CCR. According to the reflectance of the wedge prism and the transmisttance of the specular CCR given in Appendix E.3 and E.4 respectively, the $\frac{A_{g_2}}{A_m} \approx 0.03$. According to Equation 5.9, the amplitude of the PNL error resulted from the 2nd-order ghost beam is estimated as 0.91 nm.

5.4 Lab test

5.4.1 Aim

Section 5.2 shows that the QI is feasible when an AR coating is used partially on the wedge prism. However, one has to ask an optics supplier to manufacture this customized component. A small amount of customization order is not accepted by an optics supplier. Thus, building a QI with the calculated specs that fulfills all the requirements is not possible in this project. Also, the aim of the project does not include the product manufacturing and integration, there is no need to manufacture the product and validate all the requirements. Instead, building a lab setup using all off-the-shelf components is a useful test to get familiared with the hardware, improve alignment skills, learn to use the PGC detection, validate the working principle and find unknowns. Thus, in this section, the mitigated QI consisting only off-the-shelf components is built and tested on an optical table. Since the measurement range, deadpath, angular range and beam area size on the target mirror are not aimed to be validated in this test, the optics will be chosen and aligned so that the interference is obtained based on the design principle.

5.4.2 Setup

Figure 5.6 shows the QI built on an optical breadboard. The optical parts and their specifications as well as the mounts for them are listed in Table 5.4.

Table 5.4: Optics and optomechanics list in the QI lab setup.

Part name	**Mount name**	**Feature**
Collimator	1. Kinematic pitch/yaw adapter 2. Fixed mirror mount	Appendix E.1 F.1 F.2
Wedge prism	Kinematic mount	Appendix E.3 F.3
CCR	Fixed mirror mount	Appendix E.4 F.1
Mirror	Kinematic mount	Appendix E.5 F.4

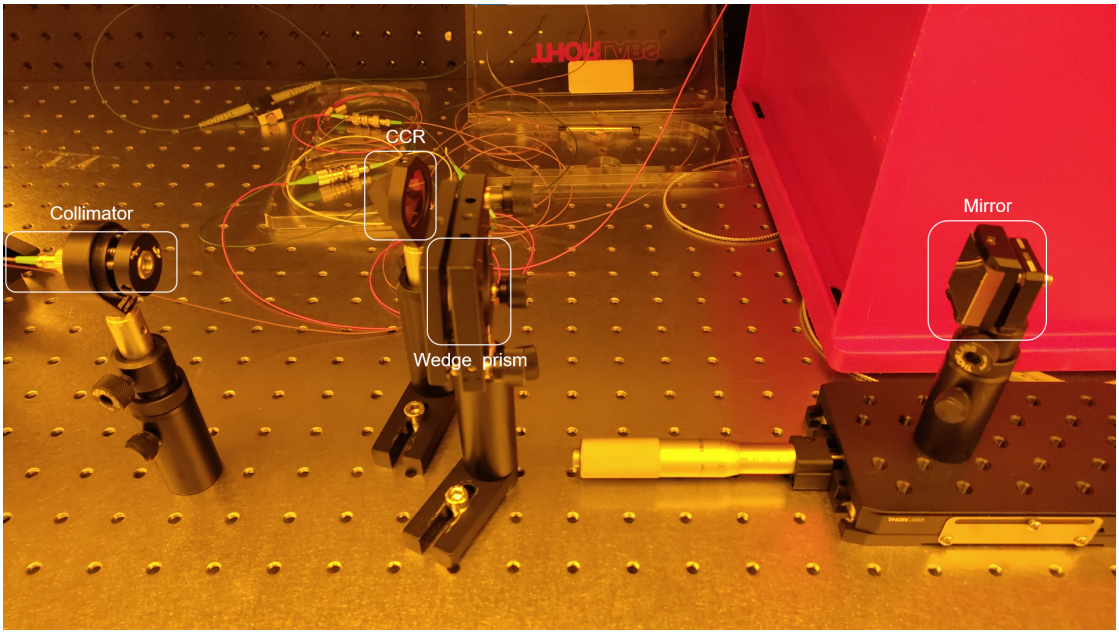

(a) A side view of the QI setup

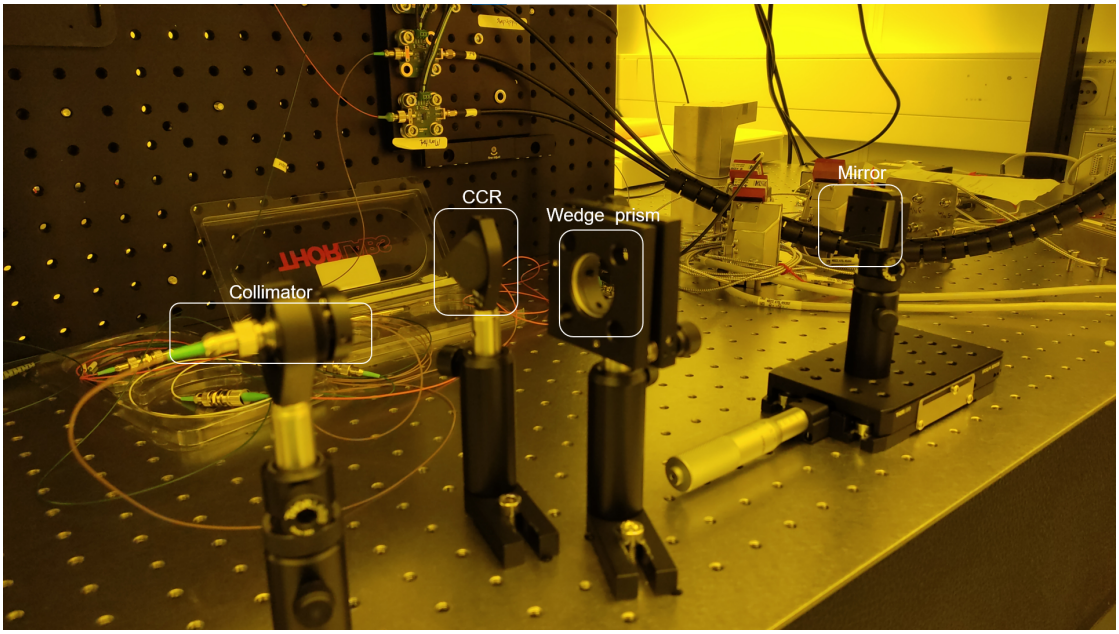

(b) Another view of the QI setup. The wedge prism can be seen more clearly.

Figure 5.6: The QI setup built on an optical breadboard

Besides the optics and the mounts, there are other parts used in the test: a laser and its driver board, an optical circulator, two photodetectors, a waveform generator and a Picoscope. These devices are introduced in Appendix G.

5.4.3 Procedure

With the parts mentioned in Subsection 5.4.2 prepared, the test can be performed in the following procedures:

1. Clean all the fiber tips
2. Connect the electronics
   Install the laser on its driver board. Then connect the laser output to the Port 1 of the optical circulator. Next connect the Port 3 of the optical circulator to the photodetector. The output of the waveform generator is connected to the laser driver board and another photodetector at the same time using a T-BNC connector. Finally connect the two photodetectors to the picoscope.
3. Alignment
   Details of the alignment part is separately written in Subsection 5.4.4.
4. Modulation tuning
   Observe the reference signal, which is the sinusoidal modulation, and the interference signal on the scope. The interference signal can be expressed by Equation 2.3 and to demodulate the phase it is then written into the Bessel series as Equation 2.4. The usable range of modulation index C, which is the Bessel function's base, is from 2.4 to 6 to prevent low signal level and high-order aliasing [39]. A quick method to check if the modulation index is in range is to count the number of periods of the interference signal in one modulation period. When the target stands still, the phase change of the interference signal is caused by the wavelength change. The range from 2.4 to 6 of modulation index C corresponds the number of periods of the interference signal in one modulation period from about three quarters to 2. This number is increased (or decreased) with the increase (or decrease) of the measurement distance and the modulation amplitude. According to this the modulation can be tuned.
5. Sampling
   Move the linear stage through the linear stage micrometer to create motions for the target mirror. Choose the correct sampling frequency by checking the spectrum of the interference signal. When the target moves, higher frequencies of the modulation frequency are excited. The sampling frequency should be chosen so that the Nyquist frequency is larger than the highest frequency in the signal spectrum. Move the linear stage and record the signals for post-processing.

5.4.4 Alignment

As mentioned in Subsection 5.4.3, before alignment the fiber tips have to be cleaned and the electronics should be connected. A fiber-delivered red laser is used for the alignment.

1. Align the reference beam
   The aim of this step is to make the rear surface of the wedge prism be perpendicular to the incident beam.

   First connect the red laser to the collimator. Now mount only the collimator and wedge prism (on holders). Be careful with the orientation of the wedge prism. On the optical table, it is more convenient to orient the wedge prism so that it only bends the beam in the plane parallel to the optical table. Roughly align the collimator and the wedge prism in line, and two weak spots should be able to observed around the collimator. According to

the orientation of the wedge, the spot reflected from the rear surface of the wedge prism can be determined.

In order to couple the reflection from the rear surface of the wedge prism into the fiber, an alignment plate with a pinhole can be used. The one used in alignment is shown in Appendix F.5. Align the pinhole to the incident beam from the collimator. Now a fraction of the light transmits the pinhole and two weak spots should be observed near the pinhole. Now carefully adjust the kinematic mount of the wedge prism. When the spot reflected from the rear surface of the wedge prism is coincident with the pinhole, the rough alignment is finished.

Now remove the alignment plate and the red laser. Connect the Port 2 of the optical circulator to the collimator, and turn on the laser. Since the diameter of the SMF core is only about 10 μm, the maximum permissible angle misalignment is very small (about ± 267 μrad according to Equation 6.8). Thus, it is very possible that there is no signal after rough alignment. One should adjust the kinematic mount very carefully and patiently until the signal is seen on the scope. It is not suggested to adjust the kinematic pitch/yaw adapter since the collimator is used for both delivering and receiving light. The sensitivity of adjusting the collimator is doubled. Continue adjusting the kinematic mount of the wedge prism until the maximum amount of signal is obtained. Now the aim is achieved: the rear surface of the wedge prism is perpendicular to the incident beam. This ensures the first and second pass beams are parallel to the third and fourth pass beams. Well aligning the reference beam makes the following steps of alignment much easier.

2. Align the measurement beam
The aim of this step is to make the mirror and the CCR aligned, so that the measurement is coupled to the fiber and interferes with reference beam.

   Connect the red laser to the collimator. Roughly align the mirror and the CCR, so that at least two spots are observed on the mirror (one spot is from the first-pass beam and the other is from the second-pass beam). It is not allowed to use the area close to the center of CCR as there is no offset. If the exit beam overlaps with the incident beam, the second-pass beam will be coupled into the fiber. Since the wedge prism is only with 1 inch diameter, the beam offset should also not be too large. If the second-pass beam is reflected by the wedge, the measurement beam will be reflected and retrace the same path as it comes.

   Now remove the red laser and connect the Port 2 of the optical circulator to the collimator. If the alignment of the reference beam is well done, the interference signal should be observed immediately when moving the linear stage. If there is no signal at all, it is shown that even the reference beam is missing. It is very likely due to the minor disturbance during disconnecting and connecting the fiber. So the interference signal should be obtained when very slightly adjusting the kinematic mount of the wedge prism. The alignment of the measurement beam is very easy if the alignment of the reference beam is well done. But if there is no signal after trials, one should restart aligning the reference beam.

   The last step is to turn on the sinusoidal modulation. With the modulated laser source, the interference signal should vary from 0 to its maximum. Otherwise the reference or the measurement beam is not well coupled thus the contrast is low. By blocking the measurement beam one can find which power of the beam is relatively smaller. Start from the corresponding alignment step according to which beam has smaller power. Align the setup until the interference signal varying from 0 to its maximum with a modulated light source.

5.4.5 Result

The collected reference and interference signals are post-processed in Matlab using the PGC algorithm. Figure 5.7 shows the demodulation results of one of the measurements. Subfigure 5.7a shows the raw interference signal, the modulation depth of which is close to 1. Subfigure 5.7b shows the Lissajous curve of the measurement without Heydemann correction. The Lissajous curve contains the sin and cos information of the phase of OPD. The fringe count is obtained from the Lissajous curve.

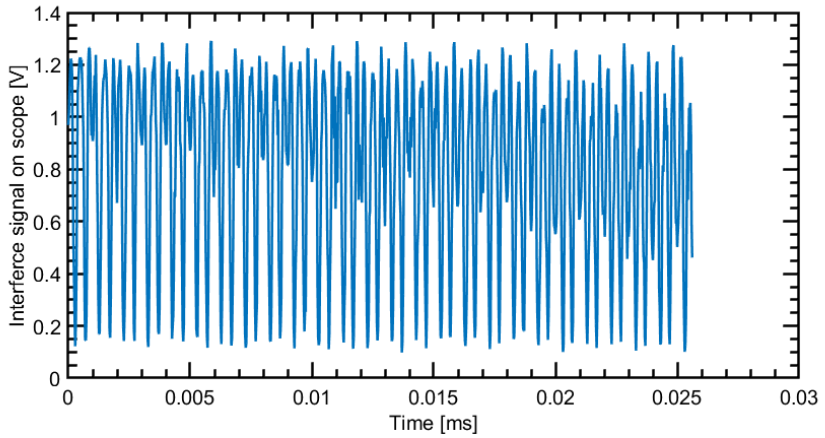

(a) The raw interference signal of one of the measurements.

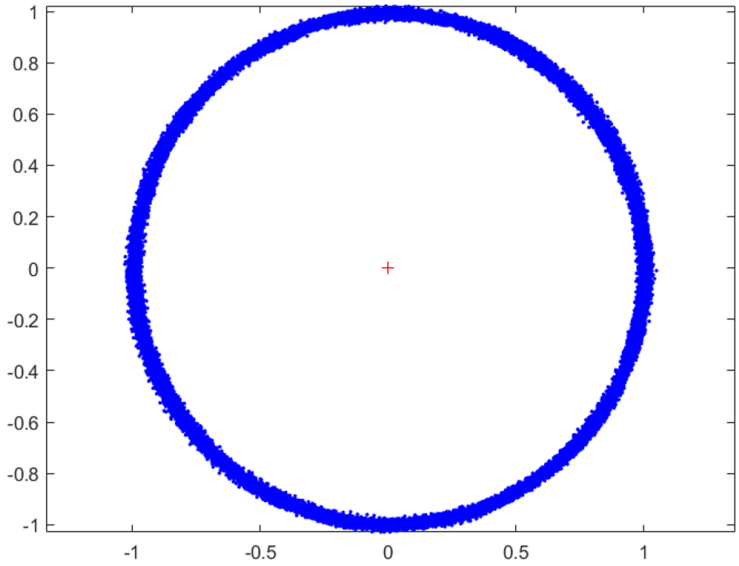

(b) The Lissajous curve of one of the measurements.

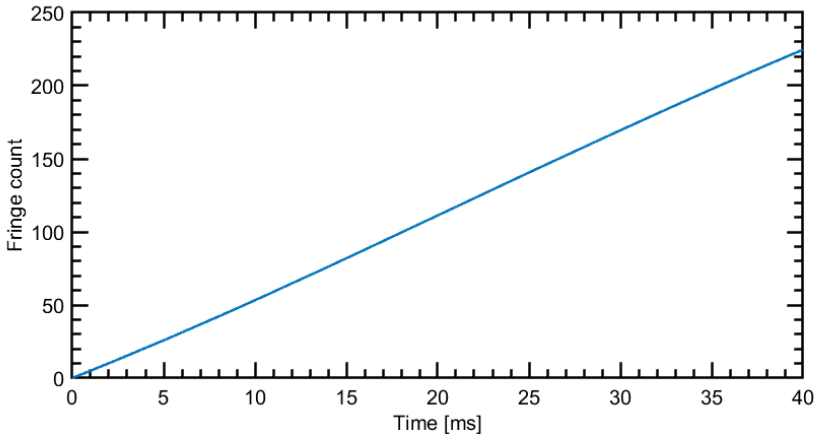

(c) The fringe counts of one of the measurements.

Figure 5.7: The demodulation result of one of the measurements.

There are several sources of noise in the measurement: unstabilized laser noise, detector noise, mechanical vibration noise, and algorithm noise. A simple method to process the displacement noise is to apply a moving average filter on the result of target displacement (i.e. $\frac{1}{NoP}$ of the fringe count). The displacement noise is the difference of the result of target displacement and its moving averaged. The spectrum of the displacement noise is shown in Figure 5.8.

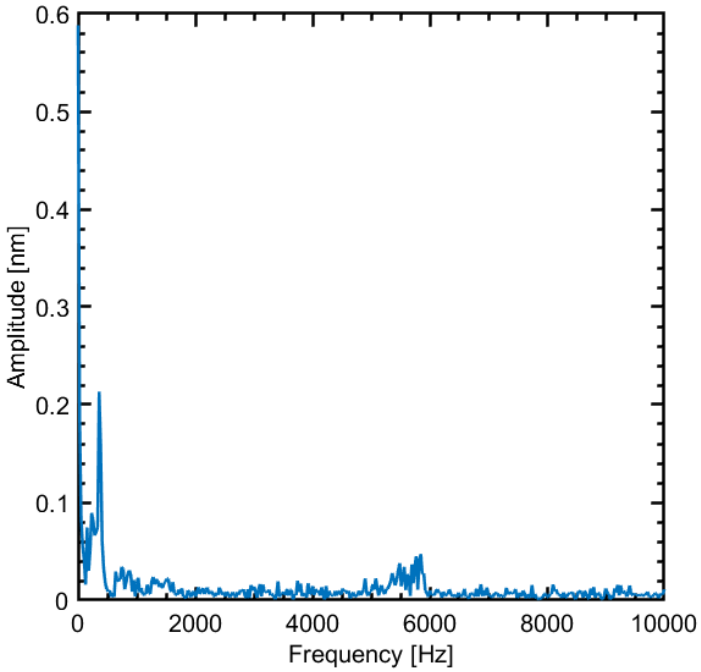

Figure 5.8: The spectrum of the displacement noise. The moving average filter is at 1 kHz.

Section 5.3 gives the theoretical derivations of the PNL error. According to Equation 5.9, the frequency of the 2nd-order ghost beam is the same as the frequency of OPD. Subfigure 5.7c shows the fringe count is nearly linear, thus the frequency of OPD can be estimated as the total fringe counts divided by the counted time, which is about 5687 Hz. In Figure 5.8, the highest peak of the displacement noise is located around 5700 Hz, which is not sharp due to the non-constant moving velocity. The theoretical result of the 2nd-order ghost beam frequency matches the measurement result.

Figure 5.9 shows the spectrum of displacement noises from two QI measurement results. The PNL error frequencies resulted from the 2nd-order ghost beam are marked in the legend and can be found in the spectrum. Besides the peaks of PNL error, there are some peaks at lower frequencies about 360 Hz. The optical table used in the lab is not vibration isolated, these low frequency peaks can be resulted from the table vibration.

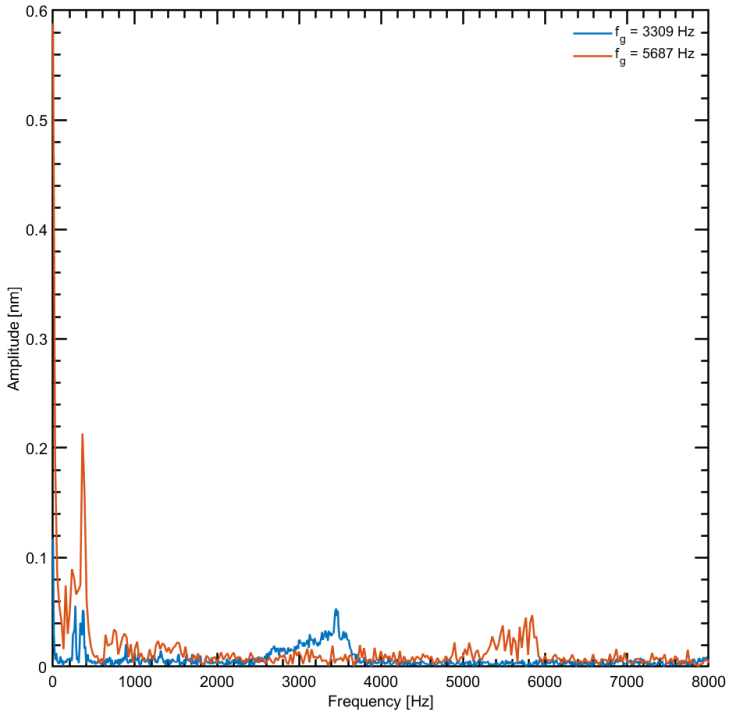

Figure 5.9: The spectrum of displacement noises from two QI measurement results. The f_g in the legend means the PNL error frequency resulted from the 2nd-order ghost beam, which is calculated from the corresponding fringe count frequency.

5.5 Conclusion

Based on the analysis in this Chapter, it is concluded that the QI has the following advantages and disadvantages:

- **Advantages**

  1. The reference and measurement beams have no walk-off.
  2. The target displacement factor $\frac{1}{NoP}$ of a quadruple-pass interferometer is smaller than a double-pass interferometer, which means a finer displacement resolution.
  3. The amplitude factor of PNL error $\frac{1}{NoP}$ of a quadruple-pass interferometer is smaller than a double-pass interferometer, which scales down the amplitude of PNL error.

- **Disadvantages**

  1. The deadpath is relatively large due to the intentional tilted target mirror design.
  2. The target velocity factor NoP of a quadruple-pass interferometer is larger than a double-pass interferometer, which results in a smaller permissible velocity in the PGC detection approach.

3. The deadpath lengths of the reference and the measurement beam are not balanced, which results in errors when temperature changes.

A design result is given with its performance compared to the given requirements. All the performance specifications are calculated based on the 350 mm measurement range. The result shown in Table 5.5 is only an example of a feasible design. The design method developed in Section 5.2 is more important than the single design result.

Table 5.5: An example of QI design results.

Item	**Requirement**	**Performance**
Measurement range	350 mm	350 mm
Maximum deadpath	350 mm	344 mm
Target angular range	> 300 μrad	± 700 μrad
Modulation depth	$> 50\%$	≈ 1 (no walk-off)
Beam area on the target mirror	within 20×8 mm^2	20×8 mm^2
PNL error amplitude	< 1 nm	≈ 0.91 nm
Thermal sensitivity	< 15 nm/K	Not investigated

Chapter 6

Double-pass Corner-cube retroreflector-based Interferometer

6.1 Principle

Figure 6.1 shows the configuration of the Double-pass Corner-cube retroreflector-based Interferometer (DCI) [41]. The light source emitted by a laser diode transmits through a SMF and exits from a collimator (input). The collimated beam strikes one of the three outer surfaces (referred as the surface A in Figure 6.1) of a TIR CCR. A fraction of the light is reflected at the air-glass interface and then collected as the reference beam by another collimator (output). Most of the light enters the CCR, undergoes TIR on one of the other surface of the CCR (referred as the surface B) and exits the TIR CCR. The target mirror is perpendicular to the beam. Being reflected by the mirror, the beam undergoes TIR on the surface B and then a fraction of light is reflected at the glass-air interface of the surface B. Then the beam undergoes TIR at the third surface of the CCR (referred as the surface C) and exits the TIR CCR. Being reflected by the mirror, the beam undergoes TIR at the surface C, then most of the light exits from the surface A of the CCR and is collected as the measurement beam by the collimator (output). A photodetector is connected to the collimator (output) through a fiber.

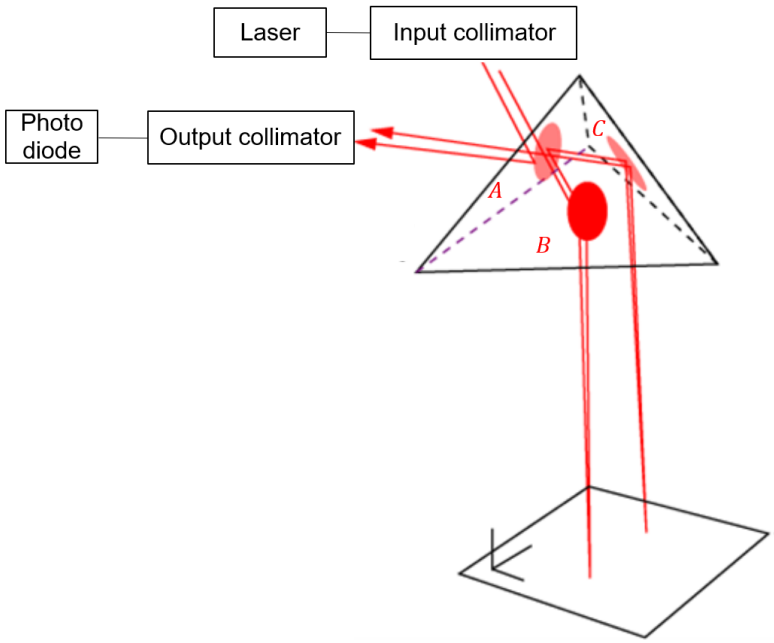

Figure 6.1: Schematic view of the double-pass corner-cube interferomter. A TIR CCR is represented by three orthogonal surfaces with their name marked as A, B and C.

6.2 Feasibility analysis

The principle of the DCI does not introduce a limit on the deadpath. According to the design strategies, the deadpath of the DCI can be determined to be the minimum value 233 mm limited by the PGC. Due to the double-pass design, the reference and measurement beams have walk-off when the target mirror is tip-tilted. The beam walk-off has to be calculated to check if the angular range is fulfilled at the maximum measurement distance 583 mm. The positions of the incident and exit beams at the CCR entrance determine the beam area size on the target mirror. Potential ghost reflections should be investigated for the PNL error requirement. Remarkably, the DCI requires a CCR that at least one of three orthogonal planes is transparent to feed in the source beam. Section 6.1 uses a TIR CCR for the principle explanation. The reflection of two planes on the three orthogonal planes of the CCR is the TIR. How the total reflections influence the measurement should be firstly investigated.

6.2.1 TIR CCR-based interferometer investigation

Section 2.1 shows that a TIR CCR is typically designed such that each face would have an incident angle of 54.7356° for normal incident beams. However, this angle cannot be achieved in the DCI where the source beam has to be fed into the glass from air. This indicates that in the DCI, the beam path inside the TIR CCR can only follow a specially designed path. Section 2.1 also explains that the TIR introduces different phase delays to s- and p- polarizations dependent on the angle of incidence and the refractive indices. Considering the geometry of a TIR CCR, it introduces different phase delays to s- and p- polarizations and also makes the two leak into each other. To find out how the interference is influenced by the TIR, the polarization

transformations in the TIR CCR have to be known first. The polarization properties of a TIR CCR is researched in [46]. This method modeling the polarization state changes using Jone's matrix can be applied in the DCI design to check how the interference signal is influenced by the TIR. The polarization transform matrices of the reference and measurement beam paths can be calculated using the rotation transform matrix 6.1, reflection matrix 6.2 and TIR matrix 6.3 [47].

$$R(\theta) = \begin{bmatrix} \cos\theta & \sin\theta \\ -\sin\theta & \cos\theta \end{bmatrix} \tag{6.1}$$

Where θ is the angle between two intersecting planes.

$$T(\theta) = \begin{bmatrix} \frac{n_t \cos\theta_i - n_i \cos\theta_t}{n_t \cos\theta_i + ni \cos\theta_t} & 0 \\ 0 & \frac{n_i \cos\theta_i - n_t \cos\theta_t}{n_i \cos\theta_i + nt \cos\theta_t} \end{bmatrix} \tag{6.2}$$

Where θ_i and θ_t are the angle of incidence and reflection respectively. n_i and n_t are the refractive indices of the incident medium and the other medium respectively.

$$TIR(\theta) = \begin{bmatrix} e^{\mathrm{i}\arctan\frac{n\sqrt{(n\sin\theta)^2-1}}{\cos\theta}} & 0 \\ 0 & e^{\mathrm{i}\arctan\frac{\sqrt{(n\sin\theta)^2-1}}{n\cos\theta}} \end{bmatrix} \tag{6.3}$$

Where θ is the incident angle, n is the ratio of the refractive index of the incident medium and the refractive index of the other medium. The simplified geometry of a TIR CCR is shown in Figure 6.2. It is emphasized that all the following conclusions are based on the target is perpendicular to the measurement beams (the algorithm is still applicable under the target tip-tilt, but some extra terms will be added in calculations. The perpendicularity assumption is good for the illustration purpose). The polarization transform matrix for the reference beam and the measurement beam can be calculated using Equation 6.4 and 6.5 respectively.

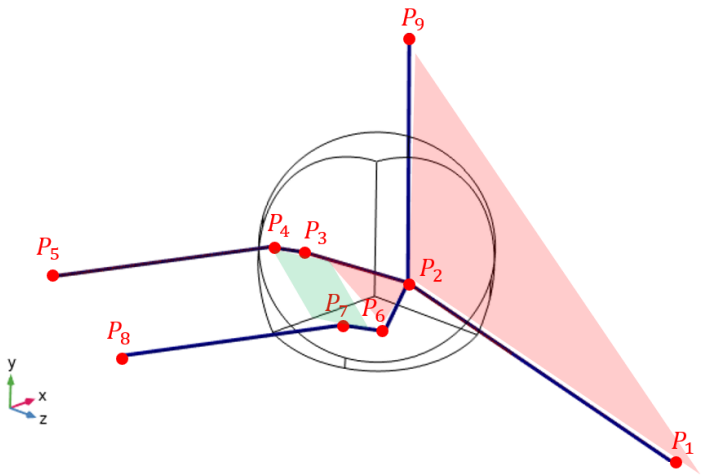

Figure 6.2: The geometry of a TIR CCR and the established coordinate system in the double-pass TIR CCR-based interferometer. An important premise is that the target mirror is perpendicular to the measurement beams but not drawn. The origin is at the vertex of the CCR. The coordinate axes are along the physical ridges of the CCR. Points $\mathbf{P_2}$, $\mathbf{P_3}$ and $\mathbf{P_6}$ are on the three orthogonal surfaces of the TIR CCR, Points $\mathbf{P_4}$ and $\mathbf{P_7}$ are on the entrance of the TIR CCR. The reference beam path is $\mathbf{P_1} \rightarrow \mathbf{P_2} \rightarrow \mathbf{P_9}$, the measurement beam path is $\mathbf{P_1} \rightarrow \mathbf{P_2} \rightarrow \mathbf{P_3} \rightarrow \mathbf{P_4} \rightarrow \mathbf{P_5} \rightarrow \mathbf{P_4} \rightarrow \mathbf{P_3} \rightarrow \mathbf{P_2} \rightarrow \mathbf{P_6} \rightarrow \mathbf{P_7} \rightarrow \mathbf{P_8} \rightarrow \mathbf{P_7} \rightarrow \mathbf{P_6} \rightarrow \mathbf{P_2} \rightarrow \mathbf{P_9}$. There are two different planes presented in the measurement beam path: the red noted one consisting of $\mathbf{P_3P_2P_6}$ and the green one consisting of $\mathbf{P_3P_4P_7P_6}$. When the beam enters one plane from the other, a rotation transform matrix using the angle between the two planes should be applied before the reflection matrix. The reference s-polarization is defined normal to the red plane, thus no extra rotation transformation is needed at the beginning and the end. This schematic is taken from a COMSOL model using the same parameters as the theoretical calculation, which is mutually verified with the algorithm.

$$J_{ref} = T(\theta) \tag{6.4}$$

$$\begin{aligned} J_{meas} =& TIR(\theta_6)R(-\theta_{rg})T_{mir}TIR(\theta_6)R(\theta_{rg})T(\theta_2) \\ & TIR(\theta_3)R(-\theta_{rg})T_{mir}TIR(\theta_3)R(\theta_{rg}) \end{aligned} \tag{6.5}$$

Where θ_{rg} is the angle between the red and green planes, θ_2, θ_3, θ_6 are the incident angles where the incident points of the reflections are at $\mathbf{P_2}$, $\mathbf{P_3}$ and $\mathbf{P_6}$ respectively. T_{mir} is the ideal mirror transform matrix $[-1\,0;\,0\,1]$.

With the polarization transform Jone's matrices J_{ref} and J_{meas}, the s- and p-components of the reference and measurement beams can be calculated. The imaginary terms in J_{meas} means phase delay. When the polarization state of the light source is not controlled, i.e. the s- or p- polarization of the light source changes in amplitude or phase, the measurement beam is delayed

differently, which will be finally falsely interpreted as a displacement of the target. For simplicity, the electric field of a linear polarized light E_{LP} is defined by its p- and s- components:

$$E_{LP} = \begin{bmatrix} \cos\theta_{LP} \\ \sin\theta_{LP} \end{bmatrix} \tag{6.6}$$

Where θ_{LP} is defined as the angle of a linear polarization, which varies from 0° to 90°. A simulation is performed to check how the target displacement is falsely interpreted when the angle of linear polarization changes. The TIR CCR is modelled as Figure 6.2, and the vector of the light source is [-1, 5, -1] following the axis convention. Simulate the interference signal and demodulate the phase. The initial phase of the demodulation result of θ_{LP} = 0° is defined as the base. Figure 6.3 shows the displacement error with respect to θ_{LP}. The whole polarization modeling and interference signal simulating script is in Appendix D.4.

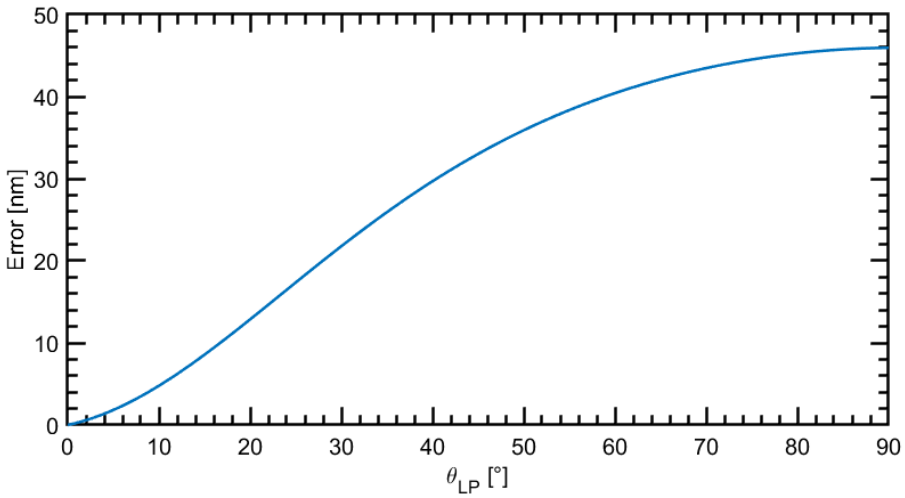

Figure 6.3: The simulated displacement error with respect to θ_{LP}

Since the aim of the design project is not to use polarization control elements, the use of a TIR CCR in the DCI is not feasible.

In addition, the incident angle should be carefully chosen. In some extreme cases, e.g., the light source is p-polarized and the incident angle is Brewster's angle, the power of one of the beams might be totally lost, thus no interference is obtained.

6.2.2 Restructured CCR-based interferometer investigation

Instead of using a TIR CCR, another retroreflector concept is combining two metallic-coated mirrors and one uncoated wedge prism (since the combination of the mirrors and the wedge prism functions as a CCR, the CCR hereinafter refers to the combination of the mirrors and the wedge prism). An example of a restructured CCR is shown in Figure 6.4. The use of two metallic-coated mirrors is to minimize the effect of polarization. The use of the uncoated wedge

prism is to ensure natural reflections being created at the surface orthogonal to the two mirrors. Also, the two surfaces of a wedge prism are not parallel, which prevents any undesired cavity reflection from being coupled. Without the TIR, the polarization change resulted from the CCR is minimized. However, the restructured CCR has risks when the three surfaces of the CCR are not exactly orthogonal to each others. In this paper, the angle deviating from 90° between two surfaces of the CCR is named as Orthogonal Error (OE). The unit of OE is radians. As the function of a CCR is to return the light along the axis parallel to the incident axis, the direct influence of OE is the exit beam is not exactly parallel to the incident beam. The angular deviation of the incident and the exit beam is called beam deviation BD, which is a technical indicator often given by CCR manufacturers. How the beam deviation finally influences the reference and measurement beams is the problem that has to be investigated first.

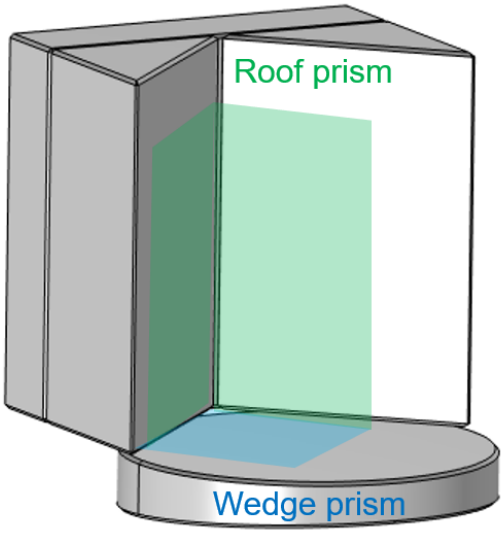

Figure 6.4: An restructured CCR consisting one wedge prism and one hollow roof prism. The roof prism has two metallic-coated mirrors that are orthogonal to each other. The wedge prism is orthogonal to the bottom plane of the roof prism. The green and blue semi-transparent planes indicate the three reflective planes, which together function as a CCR.

Coordinate based analysis

To solve this problem, a vector computing approach is developed that being able to set the angle between the wedge prism and the two mirrors, and find the beam path for the corresponding angular difference. A Cartesian coordinate system is established with the vertex of the CCR as the origin. The orientation of the axes is shown in Figure 6.5. To model all the beams in the coordinate system, each beam is represented by an originating point and a propagation vector. The plane of each optical surface is represented by a point on it and its normal vector. Rotation transform matrix 6.1 times the plane normal vector representing the rotation of the plane. The reflection and refraction of beams can be represented in vector calculations explained in Appendix D.1 and D.2 respectively. To find all the incident points and exit points, the algorithm of finding the intersection of a line and a plane is explained in Appendix D.3. With the algorithm developed, a mathematical ray tracing model is built with the freedom of changing the position and orientation of any beam and any plane. Figure 6.5 shows the beam path in the restructured

CCR-based interferomter when the target mirror is perpendicular to the measurement beams but the three surfaces of the CCR are orthogonal to each other. The following discussions are based on Figure 6.5 and the defined coordinate system.

In Figure 6.5, the direction of the reference and the measurement beams are represented by $\overrightarrow{\mathbf{P_{11}P_{12}}}$ and $\overrightarrow{\mathbf{P_9P_{10}}}$ respectively. The angle between the reference and the measurement beams θ_{rm} can be calculated using Equation D.2. Figure 6.5 also shows a beam walk-off, the value of which can be found by calculating the projection of $\overrightarrow{\mathbf{P_9P_{11}}}$ in the direction perpendicular to the reference beam (the beam walk-off is scaled with the distance between the receiving collimator and the wedge prism when $\theta_{rm} \neq 0$). The required beam area on the target mirror can be found using $\mathbf{P_6}$ and $\mathbf{P_7}$ ($\left|\overrightarrow{\mathbf{P_6P_7}}\right|$ = 14.4 mm in Figure 6.5). By changing the OE from zero to a small angle, the corresponding θ_{rm} and beam walk-off can be calculated. Since the beam deviation of the CCR is a more often used technical indicator than OE, The sensitivities are written in the forms of $\frac{\partial \theta_{rm}}{\partial BD}$. This computing approach can also be used for calculating the angular range. The results are listed in Table 6.1. The full script of the algorithm is in Appendix D.5.

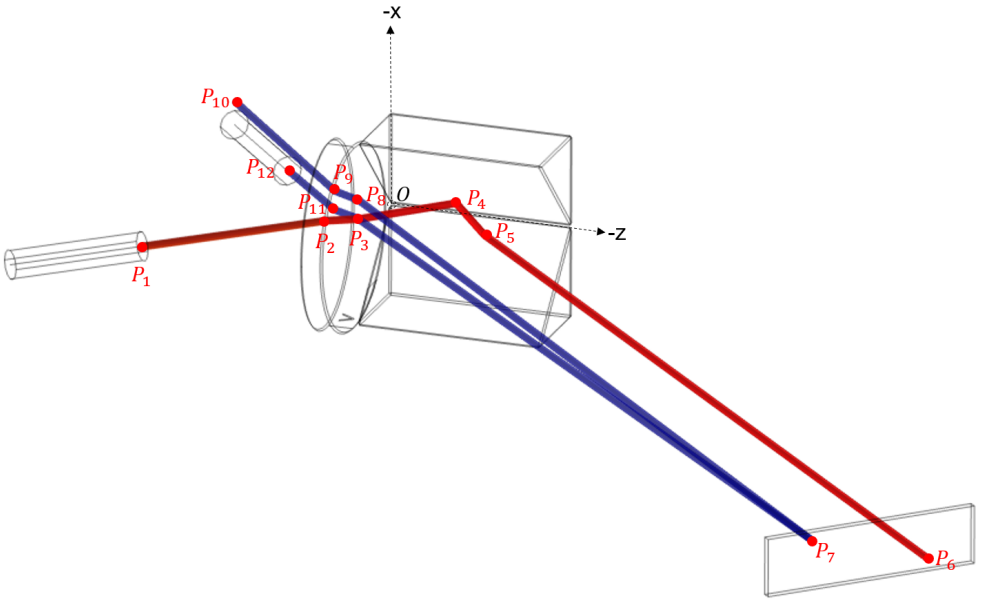

Figure 6.5: The beam path of the restructured CCR-based interferometer when the target mirror is perpendicular to the measurement beams but the three surfaces of the CCR are orthogonal to each other. The origin of the coordinate system is at the vertex of the restructured CCR and marked as O, the orientations of the axes are marked by dashed black lines (y-axis is not marked to keep the beam paths clear and it follows the right hand rule). Also, the reflection from the (rear) surface of the wedge is not shown in order to observe the beam paths clearly. The reference beam path is $\mathbf{P_1} \rightarrow \mathbf{P_2} \rightarrow \mathbf{P_3} \rightarrow \mathbf{P_{11}} \rightarrow \mathbf{P_{12}}$, the measurement beam path is $\mathbf{P_1} \rightarrow \mathbf{P_2} \rightarrow \mathbf{P_3} \rightarrow \mathbf{P_4} \rightarrow \mathbf{P_5} \rightarrow \mathbf{P_6} \rightarrow \mathbf{P_5} \rightarrow \mathbf{P_4} \rightarrow \mathbf{P_3} \rightarrow \mathbf{P_7} \rightarrow \mathbf{P_8} \rightarrow \mathbf{P_9} \rightarrow \mathbf{P_{10}}$. The red colored beams have stronger optical power than the blue colored beams. This schematic is taken from a COMSOL model using the same parameters as the theoretical calculation, which is mutually verified with the algorithm.

Table 6.1: Sensitivities at the measurement distance 583 mm. d_{rm} is the beam walk-off, θ_{rm} is the angle difference of the reference and the measurement beams, θ_{target} is the angular deviation of the target. Since both the wedge and the target can be rotated along any axis in space to generate OE and angular deviations, only two orthogonal rotation axes are selected in the calculation, and the larger sensitivity values are listed in the table.

Sensitivity	Value
$\frac{\partial d_{rm}}{\partial BD}$	1.188 mm/mrad
$\frac{\partial \theta_{rm}}{\partial BD}$	2.242
$\frac{\partial d_{rm}}{\partial \theta_{target}}$	2.381 mm/mrad

Coupling analysis

The next step is to determine the permissible beam walk-off d_{rm} and the beam deviation at the collimator θ_{rm}. Figure 6.6 shows the considerations on how d_{rm} and θ_{rm} affect the light coupling. The following calculations are based on the collimator and SMF data in Appendix E.1 and E.2 respectively. First of all, the two beams should be within the aperture of the collimator lens. If the two beams are within the aperture of the lens, d_{rm} results in a change of incident NA, and θ_{rm} results in a focus point shift on the focal plane. At a small angle, the NA and focus shift Δ_f can be estimated by Equation 6.7 and 6.8 respectively. The specifications of the collimator and SMF used for calculations are listed in Appendix E.1 and E.2 respectively. Rewriting Equation 6.7, the expression of angular range is derived. Using Equation 6.9, the SMF with NA = 0.14 permits around 0.825 mm beam walk-off, which corresponds to 346.4 µrad angular range. Figure 6.6 assumes the reference beam is ideally coupled, which means the beam waist diameter at the focus is nearly the model field diameter (MFD). The measurement beam is partially in the MFD due to the focus shift Δ_f, which in the end degrade the modulation depth. A simulation is done to calculate the modulation depth of the interference respect to the focus shift. Figure 6.7 shows the interfere patterns in the highest modulation depth (1) and in the degraded modulation depth. Figure 6.8 shows the simulation result about the modulation depth with respect to the focus shift Δ_f. From the result, 50% modulation depth is preserved when Δ_f = 5.3 µm, which permits the beam misalignment θ_{rm} = 282.7 µrad using Equation 6.8.

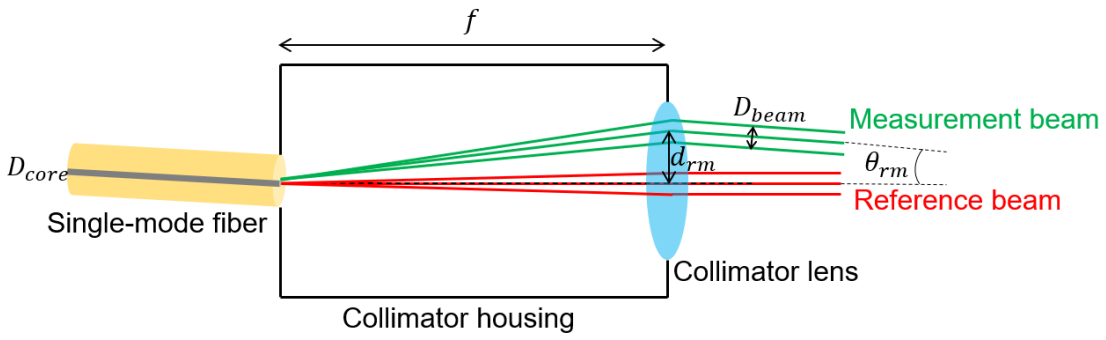

Figure 6.6: Schematic for coupling reference and measurement beams from free space using a collimator and SMF. The beam is characterized by three lines. The reference beam is supposed to be on axis and focused to the center of the core of SMF.

$$NA_{in} = \frac{\frac{D_{beam}}{2} + d_{rm}}{f} \tag{6.7}$$

$$\Delta_f = \theta_{rm} f \tag{6.8}$$

$$AngularRange = \frac{NA_{SMF} \cdot f - \frac{D_{beam}}{2}}{\frac{\partial d_{rm}}{\partial \theta_{target}}} \tag{6.9}$$

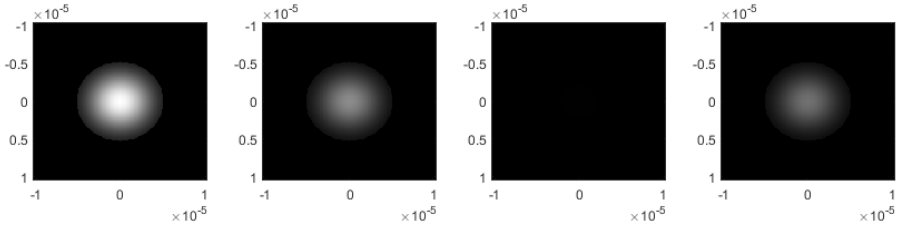

(a) Irrdiance plot when the reference and the measurement beams are ideally coupled in the MFD of the fiber. From the left to the right figure, the phase differences of the two are 0, $\frac{\pi}{2}$, π, $\frac{3\pi}{2}$ respectively.

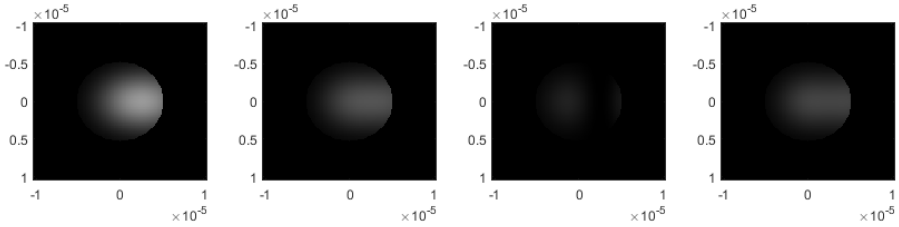

(b) Irradiance plot when the reference is ideally coupled in the MFD of the fiber but the measurement beam has a focus shift of half of the MFD. From the left to the right figure, the phase differences of the two are 0, $\frac{\pi}{2}$, π, $\frac{3\pi}{2}$ respectively.

Figure 6.7: The irradiance of the interference pattern in the MFD plotted in grey scale. The modulation depth loss can be visualized by comparing Subfigure 6.7a and 6.7b. The unit of the axes is meter.

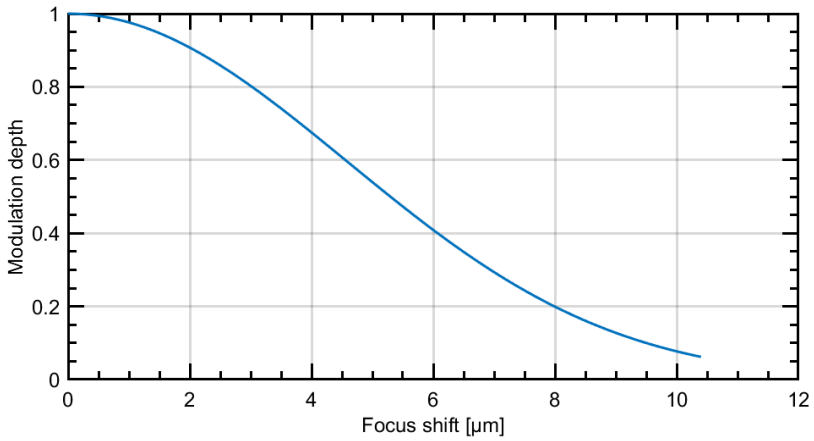

Figure 6.8: The modulation depth of the interference irradiance with respect to the focus shift.

The above discussion shows that the beam walk-off and beam misalignment are limited by the NA of a SMF and the modulation depth. A multi-mode fiber has a larger NA than a SMF, which permits a larger beam walk-off. However, a multi-mode fiber, as the name indicates, supports multiple modes of light traveling in the fiber core. Assuming the reference beam is deally coupled, the beam walk-off and beam misalignment result in an inclined measurement beam. On the cross section of the multi-mode fiber, fringes are observed due to the mode differences of the two beams. The fringes in the end degrade the modulation depth. A simulation is done to calculate the modulation depth of the interference respect to the inclined angle. Figure 6.9 shows the interfere patterns in the highest modulation depth (1) and in the degraded modulation depth. Figure 6.10 shows the simulation result about the modulation depth with respect to the inclined angle. From the result, 50% modulation depth is preserved when the inclined angle = 320 µrad.

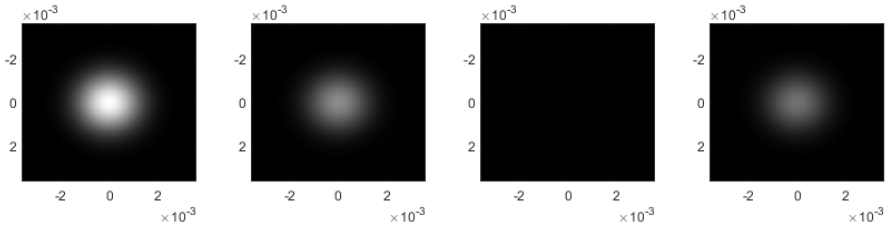

(a) Irrdiance plot when the reference and the measurement beams are both on axis. From the left to the right figure, the phase differences of the two are 0, $\frac{\pi}{2}$, π, $\frac{3\pi}{2}$ respectively.

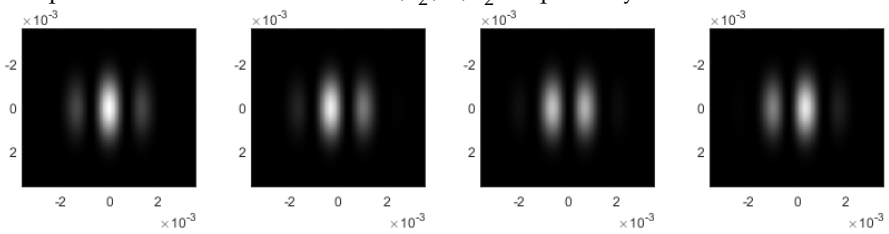

(b) Irradiance plot when the reference is on axis but the measurement beam has an inclined angle of 1 mrad. From the left to the right figure, the phase differences of the two are 0, $\frac{\pi}{2}$, π, $\frac{3\pi}{2}$ respectively.

Figure 6.9: The irradiance of the interference pattern in grey scale. The fringes can be visualized in Subfigure 6.9b, which results in a smaller modulation depth. The unit of the axes is meter.

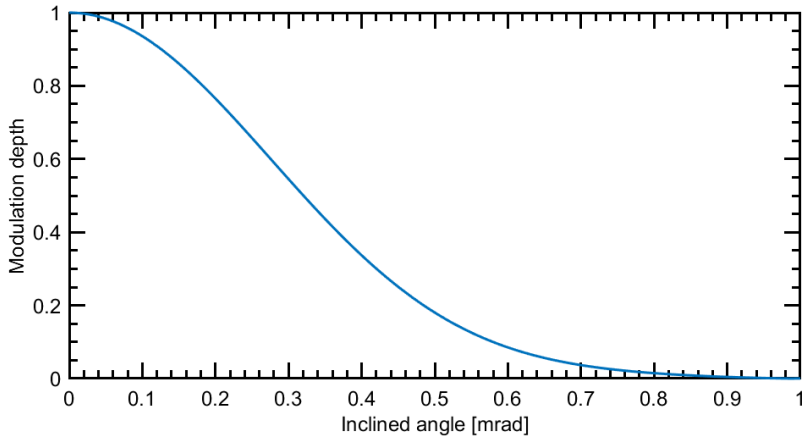

Figure 6.10: The modulation depth of the interference irradiance with respect to the inclined angle.

Feasibility conclusion

In summary, the restructured CCR-based interferometer model is investigated by building a coordinate system. The coordinate calculations find the most critical sensitivity values in the DCI system. To further use these values to obtain the angular range of the DCI and the tolerances of the CCR, the beam walk-off and beam misalignment satisfying 50% modulation depth for single-mode and multi-mode fiber couplings are discussed. The final results are list in Table.

Instead of using OE tolerance to indicate how large the three surfaces of the CCR can be not perpendicular to each other, the beam deviation of the CCR is used as it is the indicator more often used in the CCR manufacturing.

Table 6.2: The angular range and the required beam deviation of the CCR. The angular range using multi-mode fiber coupling is calculated based on a multi-mode fiber with 0.2 NA.

	SMF coupling	**Multi-mode fiber coupling**
Angular range [μrad]	±346.4	±818.9
Beam deviation of CCR [arcsec]	26.0	29.4

Due to its larger NA, a multi-mode fiber permits a larger angular range than a SMF. In both cases of coupling, the beam deviation of the CCR should be limited less than around 25 arcsec. A standard Thorlabs hollow CCR has less than 20 arcsec beam deviation [48]. The tolerance of the CCR is thus reasonable in the DCI design. It is safe to conclude that the DCI is a feasible design to satisfy the measurement range, deadpath, angular range and beam area on the target requirements.

6.3 PNL analysis

The restructured CCR-based interferometer only uses non-polarizing optics, thus there is no polarizing leakage issue. The PNL error is mainly from ghost reflections. Due to the two faces of the wedge prism are not parallel, cavity reflections will not become the ghost beam. The measurement beam combines with the reference beam after two passes traveling. But when the majority of the measurement beam transmits through the wedge prism at the second pass, a fraction of it is reflected at the air-glass interface of the wedge prism, travels another two passes, and finally mixes with the desired reference and measurement beams if there is no OE or target tip-tilt.

This scenario is similar to the scenario in the QI. Equation from 5.3 to 5.9 also hold for the PNL error calculations in the DCI. However, there are several differences:

- NoP
  In the QI, the $NoP = 8$. In the DCI, the $NoP = 4$.
- Polarization and incident angle dependent beam amplitudes
  In the QI, the reference, measurement and ghost beams are reflected at 90° at the wedge prism, which is special considering the reflection coefficient for both s- and p- polarizations are 0.2. In the DCI, the three beams are reflected at the same angle less than the TIR angle (for example, the angle used in Figure 6.5 is about 28°). Equation 6.4 shows the reflection coefficient with respect to the incident angle for s- and p- polarizations. On the one hand, since the light source is without polarization control, the incident angle for the reference beam should not be the Brewster's angle and in its close region to prevent large optical power loss. On the other hand, the polarization dependent reflection coefficient results in polarization dependent beam amplitudes. The amplitude of PNL error, which depends on the amplitude ratios of the three beams, will in the end depend on the polarization state of the light source and the incident angles of the reference beam.
- Target tip-tilt dependent beam amplitudes
  In the QI, the reference, measurement and ghost beams have no walk-off even if the target

is tip-tilt. In the DCI, the measurement beam has walk-off with the reference beam if the target is tip-tilted, and the 2nd-order ghost beam has the same walk-off with the measurement beam, which means the walk-off has been doubled compared to the reference beam. The target tip-tilt dependent beam walk-off results in target tip-tilt dependent beam amplitudes. The amplitude of PNL error, which depends on the amplitude ratios of the three beams, will in the end depend on the target tip-tilt.

To estimate the amplitude of the PNL error caused by the 2nd-order ghost beam, first it is assumed there is no beam walk-off or beam misalignment. The polarization transform matrices for the reference, measurement and nth-order ghost beams are expressed in Equation 6.10, 6.11 and 6.12 respectively, assuming the target mirror is normal to the measurement beams.

$$J_{ref} = T(\theta_{ref}) \tag{6.10}$$

$$J_{meas} = T(\theta_{meas}) \tag{6.11}$$

$$J_{g_n} = (J_{meas})^{1+n} \tag{6.12}$$

Where θ_{ref} is the incident angle of the reference beam (half of $\angle\mathbf{P_2P_3P_11}$ in Figure 6.5), and θ_{meas} is the incident angle of the measurement beam (half of $\angle\mathbf{P_4P_3P_7}$ in Figure 6.5). If the polarization state of the source beam is:

$$E_{sor} = \begin{bmatrix} A_p e^{i\theta_p} \\ A_s e^{i\theta_s} \end{bmatrix} \tag{6.13}$$

Where A_p and A_s are the electric field amplitudes of the p- and s- polarization of the source respectively. θ_p and θ_s are the phase delays of the p- and s- polarization of the source respectively. Since J_{ref}, J_{meas} and J_{g_n} are real matrices in the restructured CCR, the electric field of the reference, the measurement and the nth-order ghost beams can be expressed by:

$$\begin{aligned} E_{ref} &= J_{ref}\, E_{sor} = \begin{bmatrix} A_{ref,p} e^{i\theta_p} \\ A_{ref,s} e^{i\theta_s} \end{bmatrix} \\ E_{meas} &= J_{meas}\, E_{sor} = \begin{bmatrix} A_{meas,p} e^{i\theta_p} \\ A_{meas,s} e^{i\theta_s} \end{bmatrix} \\ E_{g_n} &= J_{g_n}\, E_{sor} = \begin{bmatrix} A_{g_n,p} e^{i\theta_p} \\ A_{g_n,s} e^{i\theta_s} \end{bmatrix} \end{aligned} \tag{6.14}$$

Where A represents the amplitude. The interference signal is the summation of the p- and s- interference. Thus the PNL error in the DCI is the summation of the p- and s- components on the numerator and denominator of Equation 5.7 respectively. Equation 6.15 is the expression of the PNL error resulted from nth-order ghost beam.

$$\varepsilon_n = \frac{1}{k\,NoP}\arctan\frac{\frac{A_{ref,s}A_{gn,s}+A_{ref,p}A_{gn,p}}{A_{ref,s}A_{meas,s}+A_{ref,p}A_{meas,p}}\sin((n-1)\phi_{OPD}) + \frac{A_{meas,s}A_{gn,s}+A_{meas,p}A_{gn,p}}{A_{ref,s}A_{meas,s}+A_{ref,p}A_{meas,p}}\sin((n-2)\phi_{OPD})}{1+\frac{A_{ref,s}A_{gn,s}+A_{ref,p}A_{gn,p}}{A_{ref,s}A_{meas,s}+A_{ref,p}A_{meas,p}}\cos((n-1)\phi_{OPD}) + \frac{A_{meas,s}A_{gn,s}+A_{meas,p}A_{gn,p}}{A_{ref,s}A_{meas,s}+A_{ref,p}A_{meas,p}}\cos((n-2)\phi_{OPD})} \tag{6.15}$$

If only consider the 2nd-order ghost beam and $A_{g_2} \ll A_{ref}$, $A_{g_2} \ll A_{meas}$, the PNL error is:

$$\varepsilon_2 = \frac{1}{k\,NoP}\frac{A_{ref,s}A_{gn,s} + A_{ref,p}A_{gn,p}}{A_{ref,s}A_{meas,s} + A_{ref,p}A_{meas,p}}\sin(\phi_{OPD}) \tag{6.16}$$

Equation 6.16 indicates that the PNL error is determined by the polarization state of the light source and the incident angle. With n = 1.5 and θ_{meas} = 0.7854 rad (in the configuration of Figure 6.5), the amplitude of PNL error is estimated as 0.55 nm for p-polarized source, 5.6 nm for s-polarized source.

6.4 Lab test

6.4.1 Aim

Section 6.2 shows that the DCI is feasible using the restructured CCR. However, one has to ask an optics supplier to manufacture this customized component, especially making the wedge prism and the two mirrors as a monolithic part and ensuring the beam deviation within the given tolerance. A small amount of customization order is not accepted by an optics supplier. Thus, building a DCI with the calculated specs that fulfills all the requirements is not possible in this project. Also, the aim of the project does not include the product manufacturing and integration, there is no need to manufacture the product and validate all the requirements. Instead, building a lab setup using all off-the-shelf components is a useful test to get familiared with the hardware, improve alignment skills, learn to use the PGC detection, validate the working principle and find unknowns. Thus, in this section, the restructured CCR is not manufactured, but mount a wedge prism and a hollow roof prism together on a kinematic platform. The OE thus can be controlled by the kinematic platform. With this idea, the DCI with only off-the-shelf components is built on an optical breadboard. Since there is a gap between wedge prism and the roof prism, the beam path is not the same as what is designed, and the beam area on the target mirror will be larger due to the gap in the CCR. The aim of the test is to validate the principle of the DCI design and the PNL error.

6.4.2 Setup

Figure 6.11 shows the DCI built on an optical breadboard. The optical parts and their specifications as well as the mounts for them are listed in Table 6.3.

Table 6.3: Optics and optomechanics list in the DCI lab setup.

Part name	**Mount name**	**Feature**
Collimator	1. Kinematic pitch/yaw adapter 2. Fixed lens mount	Appendix E.1 F.1 F.2
Wedge prism	1. Kinematic platform mount 2. Fixed mirror mount 3. Optical construction post 4. Angle post clamp	Appendix E.3 F.6 F.1 F.8 F.10
Hollow roof prism	1. Kinematic platform mount 2. Clamping arm	Appendix E.8 F.6 F.9
Mirror	Kinematic rectangular mount	Appendix E.5 F.7

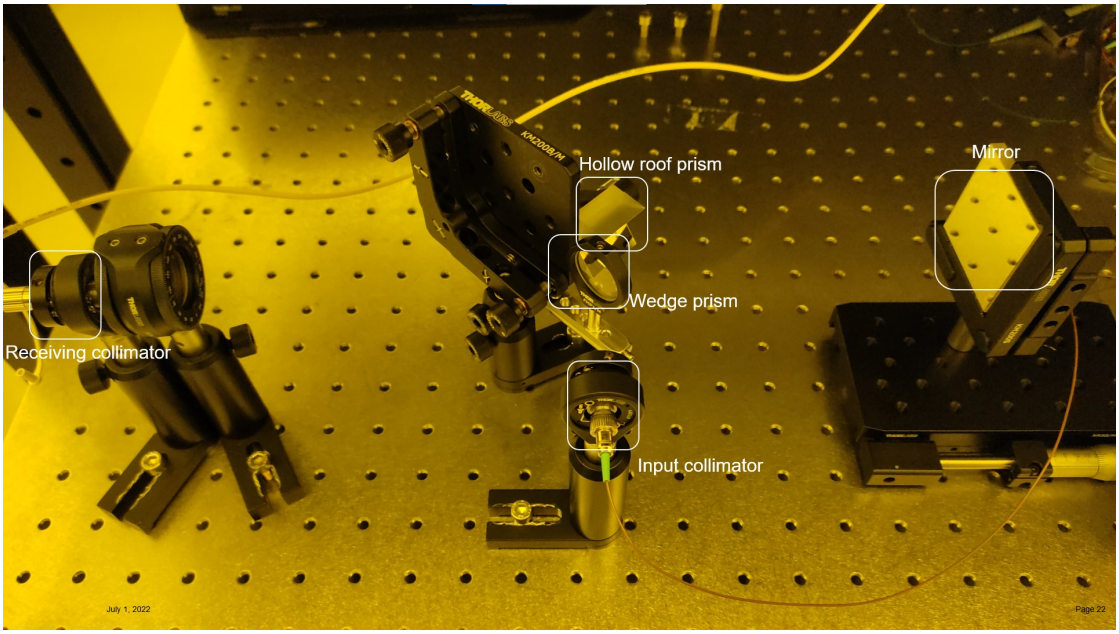

(a) A side view of the DCI setup. A dual wedge prism with rotation mounts is used to bend the beam in front of the receiving collimator for an easier coupling adjustment.

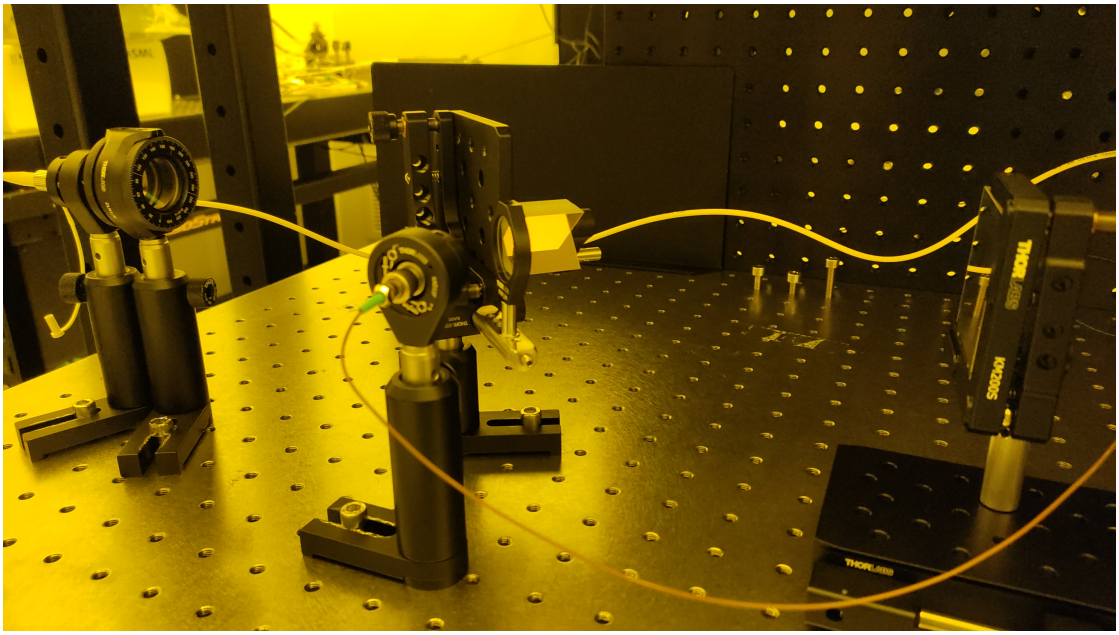

(b) Another view of the DCI setup. The restructured CCR can be seen more clearly.

Figure 6.11: The DCI setup built on an optical breadboard

6.4.3 Procedure

With the parts mentioned in Subsection 6.4.2 prepared, the test can be performed in the following procedures:

1. Clean all the fiber tips
2. Connect the electronics
   Install the laser on its driver board. Connect the output collimator and one photodetector with a fiber. The output of the waveform generator is connected to the laser driver board and another photodetector at the same time using a T-BNC connector. Finally connect the two photodetectors to the picoscope.
3. Alignment
   Details of the alignment part is separately written in Subsection 6.4.4.
4. Modulation tuning
   This setup is the same as the modulation tuning of the QI in Subsection 5.4.3.
5. Sampling
   This setup is the same as the sampling of the QI in Subsection 5.4.3.

6.4.4 Alignment

As mentioned in Subsection 5.4.3, before alignment the fiber tips have to be cleaned and the electronics should be connected. A fiber-delivered red laser is used for the alignment.

1. Install the restructured CCR
   The restructured CCR is the only functional optics in the DCI, the mount and alignment of which is the most important step to make the DCI work. In this lab test, the CCR is made by mounting a wedge prism and a hollow roof prism together on a kinematic platform. The kinematic platform consists of two parts: the L-shaped frame with bore through holes and the platform. The hollow roof prism is placed on the platform and clamped by an adjustable clamping arm. The wedge prism is firstly mounted in the fixed mirror mount. The post of the wedge prism mount is connected to the L-shaped frame through an optical construction post and an angle post clamp. By adjusting the optical construction post and the angle post clamp, the wedge prism can be placed as close as possible but not touching the roof prism, because some space is required to adjust the pitch/yaw of the platform. Fix the whole part on the optical table and prepare for the next step.
2. Inverse alignment
   The main aim of this step is to roughly adjust the OE of the restructured CCR. As the principle tells, the light source should be fed to the restructured CCR through the wedge prism. However, feeding light through the wedge makes the alignment very difficult, especially when the restructured CCR has not been carefully adjusted the OE. It is easier to first perform an inverse alignment, so that the light is perpendicularly sent to the (virtual) entrance of the restructured CCR. If the OE is very small, it is expected to observe the exit beam is parallel to the incident beam. A simple method to check the parallelism is to move a screen along the approximate axis of the incident beam and observe the position of the spot of the exit beam. A rough result is enough in this step, as Table 6.2 shows that the built requirements for the CCR is very strict. In the following steps finer alignments will be perform. The other aim of this step is to roughly find the incident angle of the input beam (fed from the wedge prism). As the incident angle at the wedge prism is always not

trivial (Figure 6.5 uses an incident angle 24.24° of the angle between $\mathbf{P_1P_2}$ and the normal of the wedge prism surface out of the CCR), it will be very useful to know where the beam is by the inverse alignment.

3. First path alignment
   The aim of this step is to align the input collimator and the target mirror perpendicular the incident beam. The OE does not affect the results of this step as Figure 6.5 shows. In this step a semi-transparent slice is needed so that light can transmit the slice at least once and the reflection can be observed on the slice. First connect the red laser to the input fiber and roughly point the collimator using the incident angle found in the inverse alignment step. The exit beam from the CCR should be as parallel to the optical table as possible. Next use the semi-transparent slice to adjust the target mirror, so that the spot from the incident beam and the spot from the reflection of the mirror are coincident. It is also possible to use a pinhole in front of the input fiber, when the target mirror is perpendicular to the incident beam, the spot of the reflection on the pinhole plane will be coincident with the pinhole.

4. Second path alignment
   The aim of this step is to complete the fine adjustment of the restructured CCR so that the OE is minimized. The second beam path is affected by the OE of the CCR. The mirror should not be adjusted in this step. Due to the wedge prism has two surfaces that are not parallel, there are two beams from the wedge prism reflections. The beam reflected from the one of the three surfaces of the CCR should be found first. Next use the semi-transparent slice to adjust the restructured CCR. If the OE is small enough, the spot from the second path incident beam and the spot from the reflection of the mirror are coincident.

5. Receiving collimator alignment
   The aim of this step is to couple the light into the receiving fiber. Subsection 6.2.2 has discussed the differences of using a SMF or a multi-mode fiber to couple the light. In this lab test a SMF is used as it does not suffer from unexpected mode coupling problems considering the OE of the restructured CCR is hard to accurately eliminate by the chosen kinematic platform mount. Coupling light from free space into a SMF is though, especially here the reference and the measurement beams should all be coupled and the OE is uncertain. A lens tube with diaphragms installed at its two ends is a useful alignment tool to point the receiving collimator to the beams. Then remove the red laser and connect the driver board output fiber. Repeat the step 5 until there is signal on the scope. By moving the linear stage and blocking the measurement beam path, it can be determined whether the reference, the measurement or both of the beams is/are coupled. If the measurement beam is not coupled or weakly coupled, one should repeat the alignment from the step 4 or 3. If the reference beam is not coupled or weakly coupled, one should repeat the alignment step 5.

6.4.5 Result

The collected reference and interference signals are post-processed in Matlab using the PGC algorithm. Figure 6.12 shows the demodulation results of one of the measurements. Subfigure 6.12a shows the raw interference signal, the modulation depth of which is close to 1. Subfigure 6.12b shows the Lissajous curve of the measurement without Heydemann correction. The Lissajous curve contains the sin and cos information of the phase of OPD. The fringe count is obtained from the Lissajous curve.

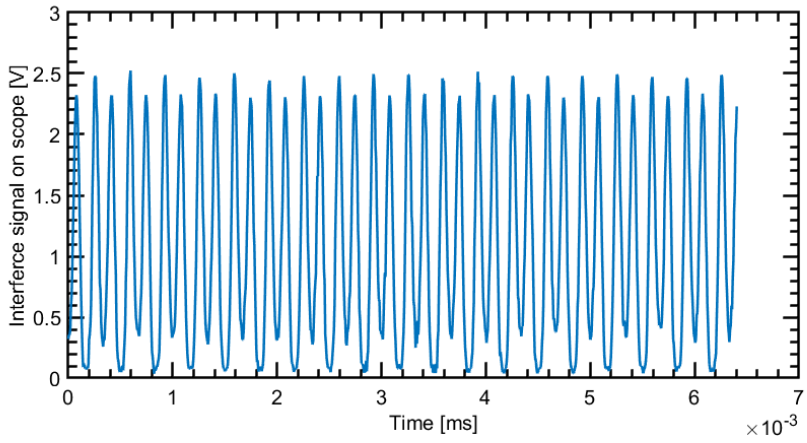

(a) The raw interference signal of one of the measurements.

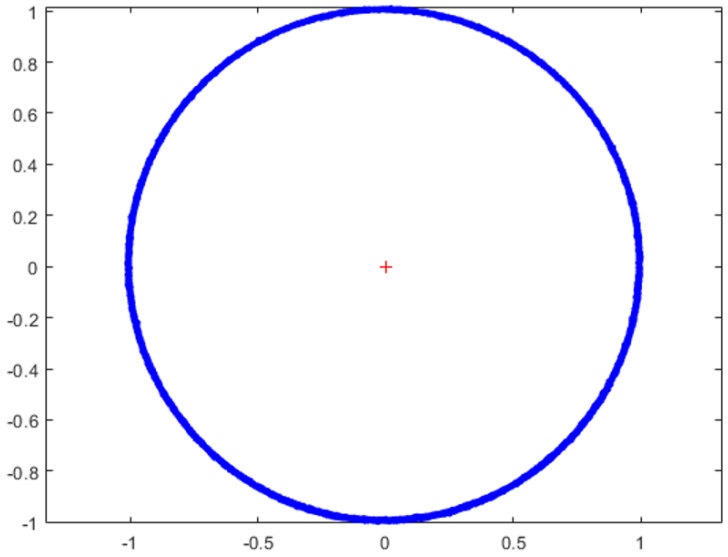

(b) The Lissajous curve of one of the measurements.

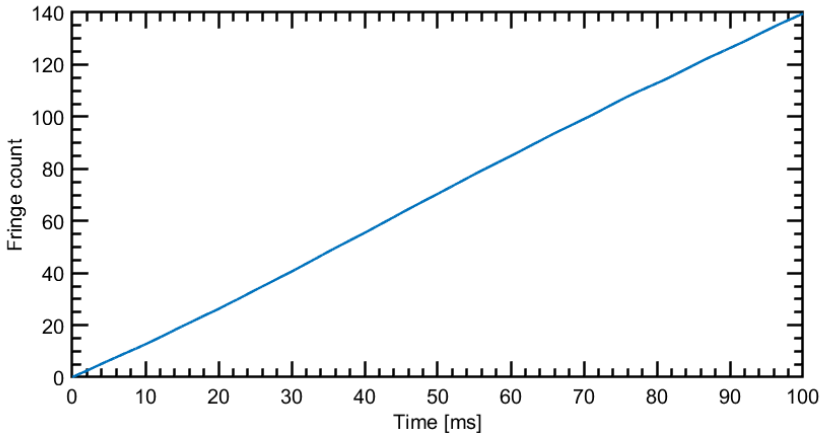

(c) The fringe counts of one of the measurements.

Figure 6.12: The interference signal and demodulation results of one of the measurements.

There are several sources of noise in the measurement: unstabilized laser noise, detector noise, mechanical vibration noise, and algorithm noise. A simple method to process the noise is to apply a moving average filter on the result of target displacement (i.e. $\frac{1}{NoP}$ of the fringe count). The displacement noise is the difference of the result of target displacement and its moving averaged. The spectrum of the displacement noise is shown in Figure 6.13.

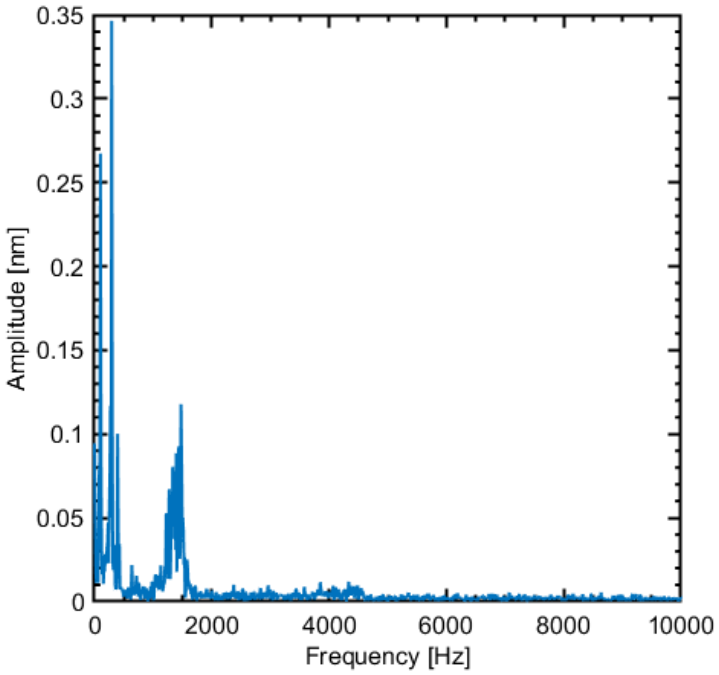

Figure 6.13: The spectrum of the displacement noise. The moving average filter is at 1 kHz.

Section 6.3 gives the theoretical derivations of the PNL error. According to Equation 6.16, the frequency of the 2nd-order ghost beam is the same as the frequency of OPD. Subfigure 6.12c shows the fringe count is nearly linear, thus the frequency of OPD can be estimated as the total fringe counts divided by the counted time, which is about 1419 Hz. In Figure 6.13, the highest peak of the displacement noise is located around 1400 Hz, which is not sharp due to the non-constant moving velocity. The theoretical result of the 2nd-order ghost beam frequency matches the measurement result.

Figure 6.14 shows the spectrum of displacement noises from two DCI measurement results. The PNL error frequencies resulted from the 2nd-order ghost beam are marked in the legend and can be found in the spectrum. Besides the peaks of PNL error, there are some peaks at lower frequencies, such as the 95 Hz peak and 286 Hz peak. The peaks around 300 Hz are common in the DCI and QI setup, which are more likely resulted from the table vibration. The hollow roof prism and wedge prism mounts have relatively low stiffness, which is more likely linked to the 95 Hz peak.

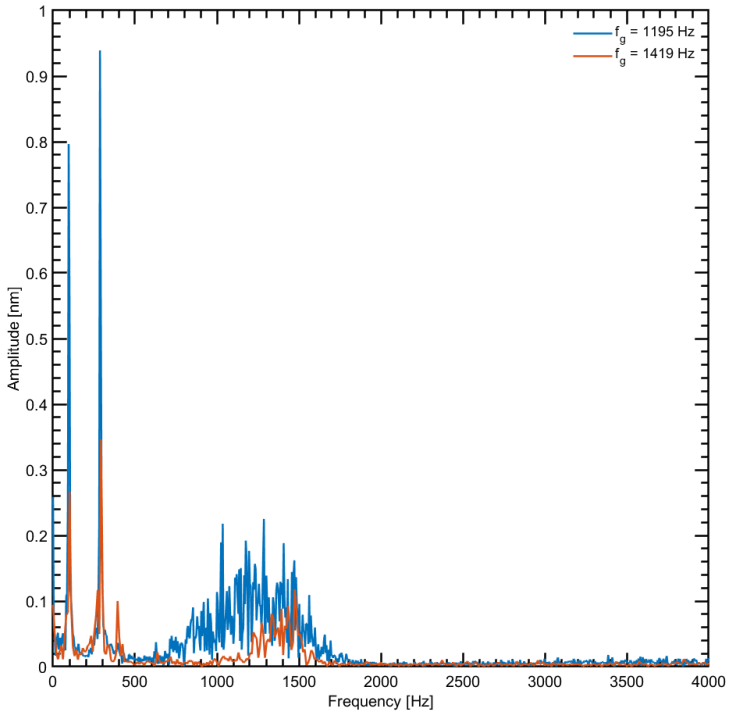

Figure 6.14: The spectrum of displacement noises from two DCI measurement results. The f_g in the legend means the PNL error frequency resulted from the 2nd-order ghost beam, which is calculated from the corresponding fringe count frequency.

6.5 Conclusion

Based on the analysis in this Chapter, it is concluded that the DCI has the following advantages and disadvantages:

- Advantages:

  1. The minimum deadpath is not limited by the design. Due to the PGC detection method, the minimum deadpath is about 233 mm.
  2. The layout is very simple.
  3. The target velocity factor NoP of a double-pass interferometer is smaller than a quadruple-pass interferometer, which results in a larger permissible velocity in the PGC detection approach.

- Disadvantages:

  1. The reference and measurement beams have walk-off when the target mirror is tip-tilted, which limits the angular range.

2. The amplitude factor of PNL error $\frac{1}{NoP}$ of a double-pass interferometer is larger than a quadruple-pass interferometer, which scales up the amplitude of PNL error.
3. The deadpath lengths of the reference and the measurement beam are not balanced, which results in errors when temperature changes.
4. The target displacement factor $\frac{1}{NoP}$ of a double-pass interferometer is larger than a quadruple-pass interferometer, which means a coarser displacement resolution.

A design result is given with its performance compared to the given requirements. All the performance specifications are calculated based on the 350 mm measurement range. The result shown in Table 6.4 is only an example of a feasible design. The design method developed in Section 6.2 is more important than the single result.

Table 6.4: An example of DCI design results.

Item	**Requirement**	**Performance**
Measurement range	350 mm	350 mm
Maximum deadpath	350 mm	233 mm
Target angular range	> 300 μrad	±818.9 μrad
Modulation depth	> 50%	≈ 50% - 100% (walk-off dependent)
Beam area on the target mirror	within 20×8 mm^2	within 14.4×4 mm^2
PNL error amplitude	< 1 nm	≈ 0.55 - 5.6 nm (polarization and angle dependent)
Thermal sensitivity	< 15 nm/K	Not investigated

Chapter 7

Conclusion and recommendation

7.1 Conclusion

In this thesis, three different interferometer design concepts have been introduced, and the feasibility of the three has been investigated. Theoretical analysis has shown that the QI and DCI are able of satisfying all the design requirements and the DLI is not feasible due to the risk of aberration. The QI and DCI have been built in the cleanroom with off-the-shelf parts to validate the working principle and PNL errors.

Table 7.1 compares the QI and DCI requirement by requirement based on the theoretical analysis in Chapter 5 and 6.

Table 7.1: Comparison of the design examples of the QI and DCI based on theoretical researches.

Requirement	**QI**	**DCI**
Measurement range	350 mm	
Maximum deadpath	344 mm	233 mm
Target angular range	$\pm$700 µrad	$\pm$818.9 µrad
Modulation depth	$\approx$ 1	$\approx$ 50% - 100%
Beam area on the target mirror	20$\times$8 mm^2	within 14.4$\times$4 mm^2
PNL error amplitude	$\approx$ 0.91 nm	$\approx$ 0.55 - 5.6 nm
Thermal sensitivity	Optical path not balanced	

The values shown in Table 7.1 are derived for the interferometers with parameters as specified in their respective chapters. These parameters could still be subject to change in a potential final implementation. Table 7.1 should therefore be seen as more of a future reference rather than a definitive estimation of the performance. The advantages and disadvantages of the QI and DCI concluded in Section 5.5 and 6.5 are more important to look at. More careful investigations need to perform after choosing the materials and mounting methods. The DCI is better than the QI

mainly in the view of deadpath, and the QI is better than the DCI mainly considering it has no beam walk-off. The other aspects, such as angular range and beam area on the target mirror, are more flexible to tune. The PNL amplitude can be compensated in the post-processing.

7.2 Recommendation

In this thesis, as much theoretical analysis as possible of three designs have been performed in the limited time, and two designs have been experimentally verified using only off-the-shelf optics and optomechanics. In the future, the following work can make this thesis more complete:

- **Theoretical work**

    1. The principles of the QI and DCI both use the natural reflections from the glass-air interface as the reference and measurement beams. The irradiance of the natural reflections is relatively very small compared to the source, which is not good to resist the noises. Although the power of laser can be adjusted, there are limits on the laser power considering damage threshold to humans and optics and laser wavelength stability. Some design improvements can made on increasing the signal strength.
    2. In the interferometry introduction, Section 2.1 shows the polarization properties of a TIR CCR. In the DCI design investigations, Subsection 6.2.1 discusses the polarization issues, which is sufficient to eliminate the TIR CCR-based interferometer concept. Subsection 6.2.2 then makes use of a restructured CCR to build the DCI, assuming that no phase delays are introduced on the mirror surfaces. Although the optics manufacturers design and coat the mirrors so that the polarization changes are minimized, the science of polarization and coating layers deserve further study.
    3. In the interferometry introduction, Section 2.1 shows some background knowledge of optical fibers. In the DCI design investigations, Subsection 6.2.2 discusses the fiber coupling issues, which is sufficient for the modulation depth calculations. The characteristics of various fibers, the differences when used in free space coupling and the effects on the signal deserve further study.

- **Experimental work**

    1. In the view of system engineering, the full project focuses on the definition of the system, including concept operations, requirements and detailed designs. The test and integration procedures are at the weak side. If ASML decides to promote the manufacturing, testing and integration one of the interferometer designs, a comprehensive test on the customized interferometer to qualify all the design requirements including the thermal sensitivity will be very necessary.
    2. The experimental research on the PNL error is yet not sufficient. Subsection 5.4.5 and 6.4.5 show the measured PNL error frequencies match the theoretical PNL error frequencies both in the QI and DCI. But the amplitudes of the PNL error can not be verified with only manual motion input on the linear stage. An actuator is needed to make a precise linear movement to the mirror. The mass of mirror is too large for the available piezo actuator in the lab. In addition, there are too many noise sources in the measurement. Building the setup on a vibration isolated table and shielding

the setup to minimize the temperature variation will help reduce the noise. With a proper motion input and a less noisy environment, the amplitude of the PNL error can be further investigated.

Appendix A

List of abbreviations

SMF Single-Mode Fiber

PMF Polarization Maintain Fiber

TIR Total Internal Reflection

CCR Corner-Cube Retroreflector

PBS Polarizing Beam Splitter

PMI Plane Mirror Interferometer

PGC Phase-Generated-Carrier

PNL Periodic Non-Linearity

DFB Distributed Feedback

AR Anti-Reflective

DLI Double-pass Lens-based Interferometer

QI Quadruple-pass Interferometer

CA Clear Aperture

OPD Optical Path Difference

DCI Double-pass Corner-cube retroreflector-based Interferometer

OE Orthogonal Error

MFD Mode Field Diameter

Appendix B

DLI

The deadpath, angular range, beam area size on the target and PNL error of the DLI are investigated.

The lenses in the DLI can be modeled using ray transfer (ABCD) matrix. The ray matrix of an on-axis thin lens in paraxial approximation is:

$$J_{lens} = \begin{bmatrix} 1 & 0 \\ -\frac{1}{f} & 0 \end{bmatrix} \tag{B.1}$$

Where f is the focal length. A light ray enters a lens crossing its input plane at a distance h from the optical axis, traveling in a direction that makes an angle θ with the optical axis. After propagation to the output plane that ray is found at a distance h' from the optical axis and at an angle θ' with respect to it:

$$\begin{bmatrix} h' \\ \theta' \end{bmatrix} = \begin{bmatrix} 1 & 0 \\ -\frac{1}{f} & 0 \end{bmatrix} \begin{bmatrix} h \\ \theta \end{bmatrix} = \begin{bmatrix} h \\ \theta - \frac{h}{f} \end{bmatrix} \tag{B.2}$$

The ray transfer (ABCD) matrix approach well models the distance from the optical axis and the angle of a paraxial ray, but the position along the optical axis is not explicitly included in the expression $\begin{bmatrix} h \\ \theta \end{bmatrix}$. In order to model all the rays in the DLI, the information along the optical axis is needed. A more effective modeling method is to establish a coordinate system with the optical axis as the horizontal axis and the direction vertical to the optical axis as the vertical axis, and express all rays by line equations. In this model, the surfaces of thin lenses, mirror and optical windows can be considered as lines. The focusing of a lens can be expressed by Equation **??**, and the angles of refraction and reflection can be calculated from the laws of refraction and reflection. The path of the ray can be determined by calculating the intersection of the lines. Figure B.1 shows the modeling result of DLI ray tracing using this method.

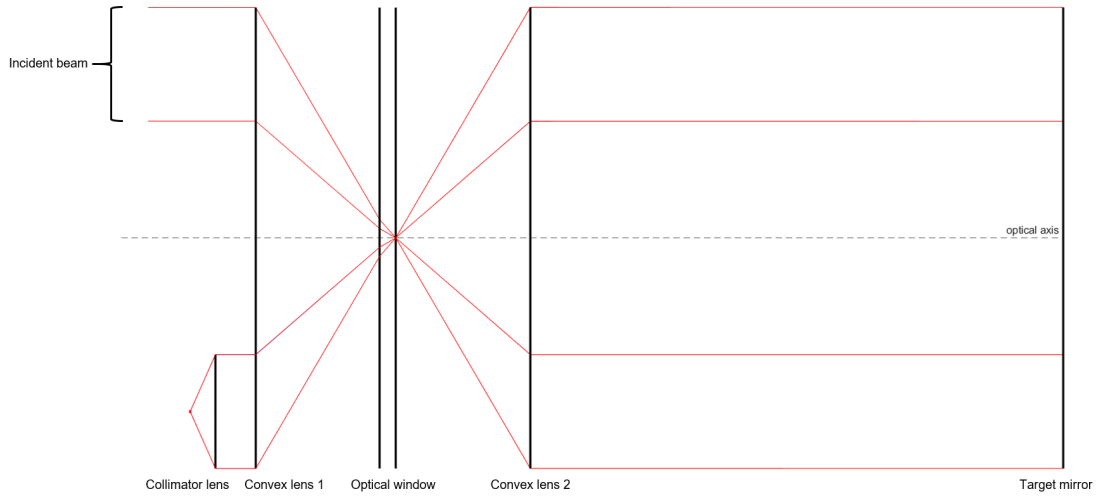

Figure B.1: The DLI ray tracing model. The incident beam is represented by two parallel red lines: the line closer to the optical axis and the other further to the optical axis. The separation between two lines is the beam diameter. The target mirror is normal to the measurement beams. The other parameters and constants used in this model is listed in Table B.1. The reflection from the

Table B.1: Parameters of the DLI model in Figure B.1

	Spec
Refractive index of air	1
Refractive index of lenses and optical window	1.5
Focal length of collimator lens	18.75 mm
Focal length of convex lenses	100 mm
Thickness of optical window	12 mm

The distance between the right surface of the wedge and the second convex lens is not a part of the measurement. Thus the deadpath of DLI is about the focal length of the second convex lens, which has been discussed in Section 4.2.

This model can research whether the reflection from the left surface of the optical window is harmful. Figure B.2 shows the reflection from the left surface of the optical window in green lines and how it is coupled. When the reference and the measurement beams are coupled into the core of a SMF with 10 μm diameter, the reflection from the left surface of the optical window is not coupled. Thus it will not disturb the interference.

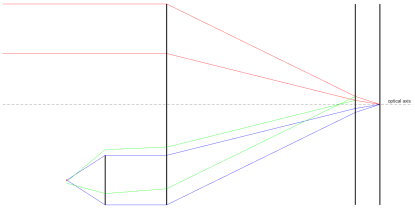

(a) Overview of the beam paths.

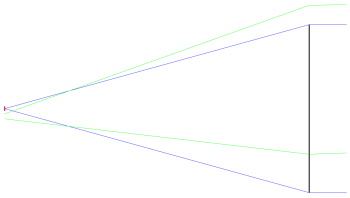

(b) Details of how the reference and measurement beams and the reflection from the left surface of the optical windows are focused by the collimator lens. The thick red line indicates the core of a SMF.

Figure B.2: The DLI ray tracing model. Blue lines represent the reference beam. Green lines represent the reflection from the left surface of the optical window.

Figure B.3 shows that if the target mirror is not normal to the measurement beams, the reference and measurement beams have walk-off. Using the model it can be calculated that 1 mrad target mirror misalignment results in 1.5272 mm beam walk-off. If a SMF with $NA_{SMF} = 0.14$ is used for coupling, the angular range of the DLI is $\pm$540.2 µrad according to Equation 6.9. The source of PNL error and the PNL error calculation of the DCI can be used to analyze and calculate the PNL error in the DLI.

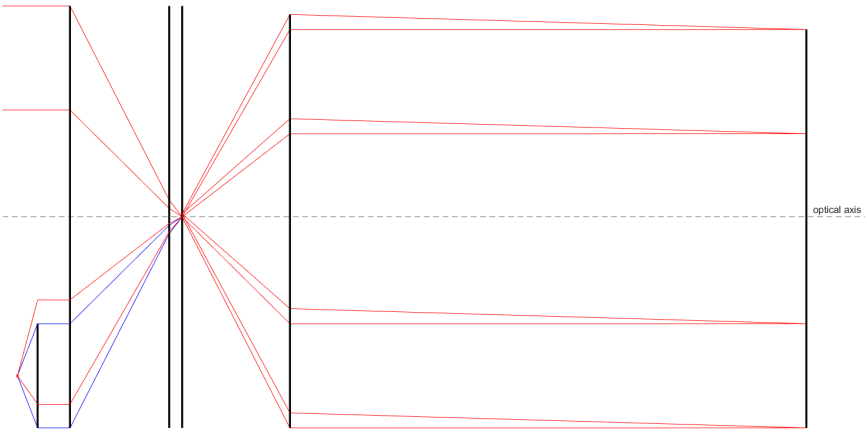

Figure B.3: The DLI ray tracing model. Blue lines represent the reference beam. The target mirror is at an angle of 540.2µrad to the optical axis.

A design result is given with its performance compared to the given requirements. All the performance specifications are calculated based on the 350 mm measurement range. The result shown in Table B.2 is only an example of a feasible design. It should be emphasized again that

this design result is not accepted due to the large volume of the lens series.

Table B.2: An example of DLI design results.

Item	**Requirement**	**Performance**
Measurement range	350 mm	350 mm
Maximum deadpath	350 mm	233 mm
Target angular range	> 300 μrad	$\pm$540.2 μrad
Modulation depth	> 50%	$\approx$ 50% - 100% (walk-off dependent)
Beam area on the target mirror	within 20$\times$8 mm^2	16$\times$4 mm^2
PNL error amplitude	< 1 nm	$\approx$ 2.4 nm (see Equation 5.9)
Thermal sensitivity	< 15 nm/K	Not investigated

Appendix C

QI

C.1 QI base model optimization function

```
%%Author: Wei She
clear; clc;
%%
x0 = [-2 -25 500  0.0025]; % initial searching point
lb = [-2 -50 233 0]; % lower bound
ub = [-2 0 4e3 pi/2]; % upper bound
options = optimoptions('fmincon','Display','iter','Algorithm','sqp');
[x_opt,fun_opt,exitflag,output,lambda,grad,hessian] = ...
    fmincon(@sqp_obj,x0,[],[],[],[],lb,ub,@sqp_noncon,options);
lambda.ineqnonlin
```

C.2 QI optimization results with the larger beam area on the target

The beam area on the target is within 20 mm×8 mm. Although this specification is given in the project proposal, it is still useful to see how much the s_{min} can be improved in both base model and advanced model by easing this constraint. The solution is listed in Table C.1, and the illustrations of the base model and the advanced model are shown in Figure C.1 and C.2 respectively.

Table C.1: Improvements of the base and advanced models if the beam area on the target is larger

D_{CCR}	**Approach**	**Optimized** s_{min}
25.4	Base model: change L_{mir} from 20 to 30 mm	575.0
25.6	Advanced model: change L_{mir} from 20 to 30 mm	280.9

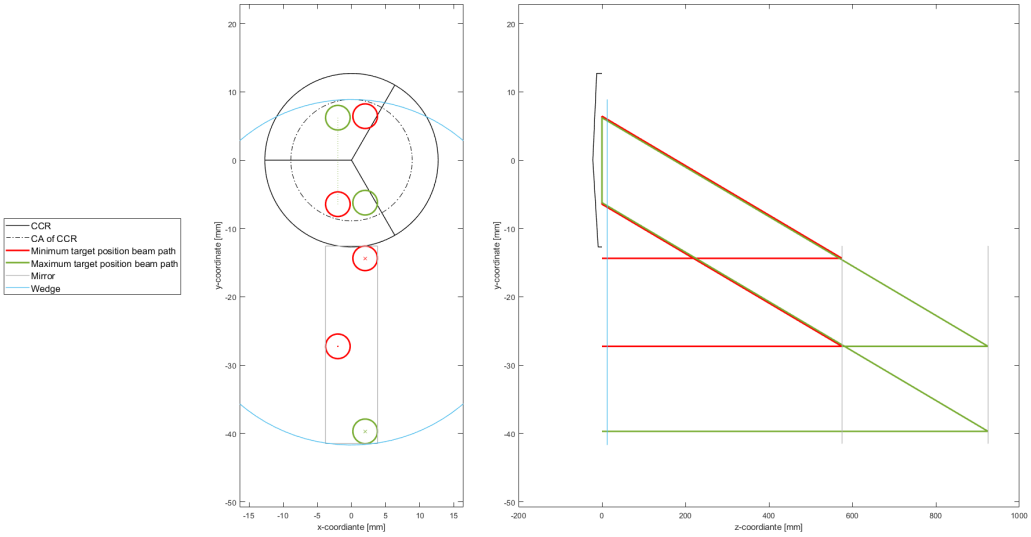

Figure C.1: The views of the QI in xy-plane and yz-plane using the solution in the first row of Table C.1.

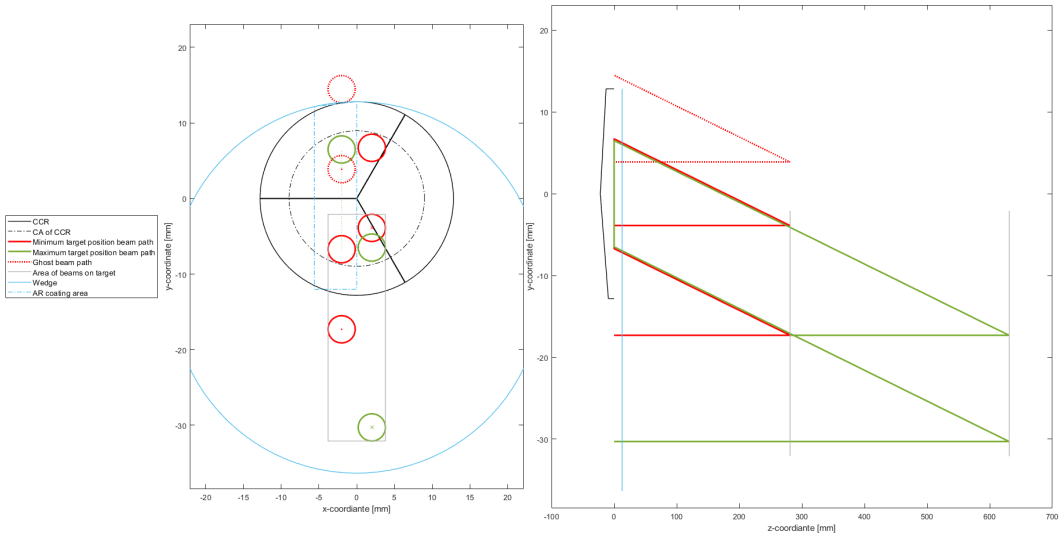

Figure C.2: The views of the QI in xy-plane and yz-plane using the solution in the second row of Table C.1.

C.3 QI base model: wedge prism positioning discussion

If we try to eliminate g_5 by carefully positioning the wedge prism so that it does not cover the exit point of $\mathbf{P_3}$, a new constraint will be introduced: $\mathbf{P_3}$ should be lower than $\mathbf{P_2'}$ with the beam

size, CA of the wedge and some tolerances considered. The solution of carefully positioning the wedge prism is listed in Table C.2 and illustrated in Figure C.3.

Table C.2: Solution of positioning the wedge prism

D_{CCR}	D_{Wedge}	Wedge center position	Optimized s_{min}
25.4	37.84	(0, -11)	589.0

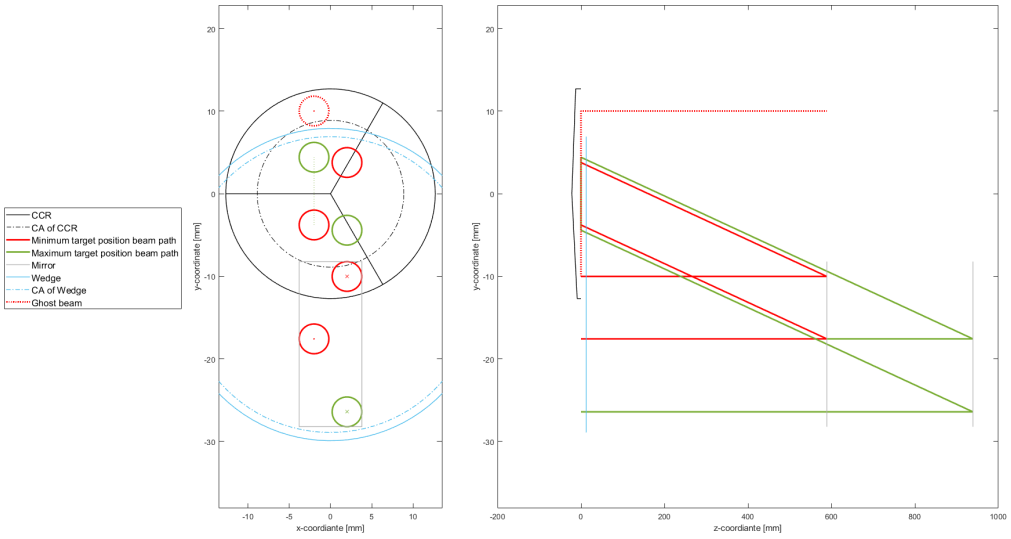

Figure C.3: The views of the QI in xy-plane and yz-plane using a 25.4 mm diameter CCR and the corresponding solution in the Table C.2. The wedge prism is positioned where the beams perpendicular to the wedge prism are within the CA and can be reflected. The risky ghost beam cannot be reflected by the wedge prism.

The drawback of this solution is that a non-standard wedge prism with its diameter of 37.84 mm is needed.

C.4 QI advanced model optimization function

```
% Author: Wei She
clear; clc;
%%
x0 = [-2 -10 500 0.01 25];
lb = [-2 -50 233 0 5];
ub = [-2 0 1000 pi/2 50];
options = optimoptions('fmincon','Display','iter','Algorithm','sqp');
[x_opt,fun_opt,exitflag,output,lambda,grad,hessian] = ...
    fmincon(@sqp_obj,x0,[],[],[],[],lb,ub,@sqp_noncon,options);
lambda.ineqnonlin
```

C.5 Trigonometric identity transformations used in the PNL error derivation

To simplify Equation 5.7, first use Equation C.1 [49] to combine the two arctangent functions into one, then eliminate the fractions in the denominator in the combined arctangent function, finally use Equation C.2 [50] to combine the sine and cosine functions.

$$\arctan(x) - \arctan(y) = \arctan\frac{x-y}{1+x\,y} \tag{C.1}$$

$$\begin{aligned} \sin(x)\cos(y) - \cos(x)\sin(y) &= \sin(x-y) \\ \cos(x)\cos(y) + \sin(x)\sin(y) &= \cos(x-y) \end{aligned} \tag{C.2}$$

Appendix D

DCI

D.1 Reflection law represented by vector calculations

The directional vector of the reflection $\vec{\mathbf{L}_\mathbf{r}}$ can be calculated when the normal vector of the media interface $\vec{\mathbf{N}}$ and the vector of the incident beam $\vec{\mathbf{L}_\mathbf{i}}$ are known. Figure D.1 illustrates the algorithm. The reflection vector $\vec{\mathbf{L}_\mathbf{r}}$ is the summation of the incident vector $\vec{\mathbf{L}_\mathbf{i}}$ and the scaled normal vector of the plane expressed in Equation D.1.

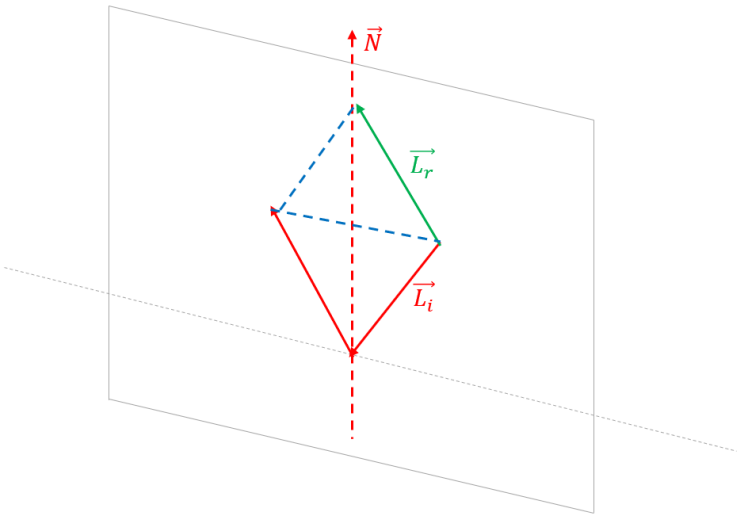

Figure D.1: The vectors resolved reflection. In this illustration $\vec{\mathbf{N}}$ points up for an easier understanding. Adding a symbol correction term in Equation D.1 will make the result independent of the direction of the normal vector.

$$\vec{\mathbf{L}_\mathbf{r}} = \vec{\mathbf{L}_\mathbf{i}} + 2\frac{\vec{\mathbf{L}_\mathbf{i}} \cdot \vec{\mathbf{N}}}{|\vec{\mathbf{N}}|}\frac{\vec{\mathbf{N}}}{|\vec{\mathbf{N}}|} \tag{D.1}$$

D.2 Refraction law represented by vector calculations

The directional vector of the refractive beam $\vec{\mathbf{L_t}}$ can be calculated when the normal vector of the media interface $\vec{\mathbf{N}}$, the vector of the incident beam $\vec{\mathbf{L_i}}$, the refractive indices of the two media n_i and n_t are known. Figure D.2 illustrates the algorithm. The incident angle θ_i can be found by calculating the acute angle between $\vec{\mathbf{N}}$ and $\vec{\mathbf{L_i}}$ using Equation D.2. The refractive angle θ_t can be calculated using Equation 2.1. The refractive vector $\vec{\mathbf{L_t}}$ is the summation of the incident vector $\vec{L_i}$ and the scaled normal vector of the plane expressed in Equation D.3.

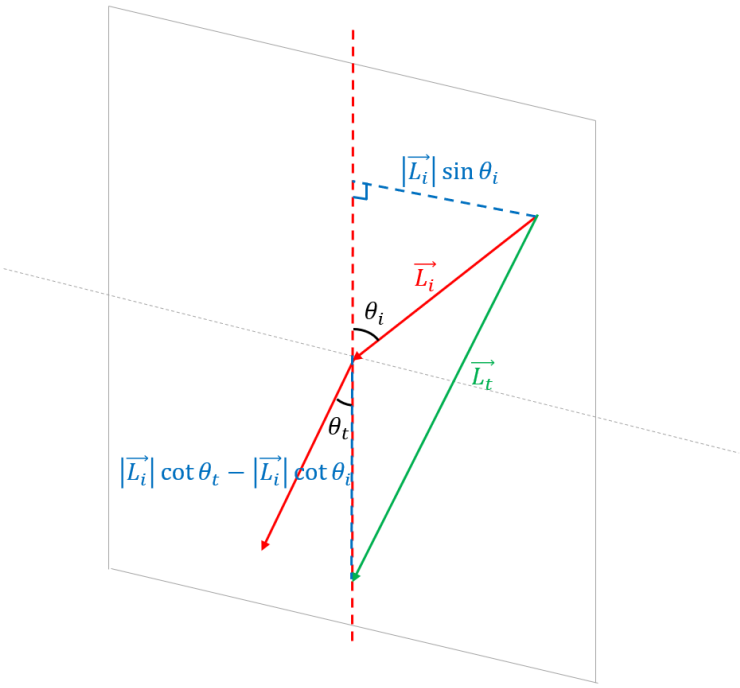

Figure D.2: The vectors resolved refraction. The normal vector of the interface $\vec{\mathbf{N}}$ is the dashed red line. In this illustration $n_i < n_t$. Equation D.2 and D.3 automatically correct the direction of $\vec{\mathbf{N}}$ and the refractive indices of the media.

$$\theta_i = \arccos \frac{\vec{\mathbf{L_i}} \cdot \vec{\mathbf{N}}}{|\vec{\mathbf{L_i}}|\,|\vec{\mathbf{N}}|} \tag{D.2}$$

$$\vec{\mathbf{L_t}} = \vec{\mathbf{L_i}} + |\vec{\mathbf{L_i}}|\,(\cot\theta_t - \cot\theta_i)\,\frac{\vec{\mathbf{N}}}{|\vec{\mathbf{N}}|} \tag{D.3}$$

D.3 Solution of the intersection of a line and a plane

In the Cartesian coordinate, the intersection $\mathbf{P_i}$ of an incident beam and a plane can be calculated when the direction of the beam $\vec{\mathbf{L}}$, the normal vector of the plane $\vec{\mathbf{N}}$, one point on the beam $\mathbf{L_0}$

and one point on the plane $\mathbf{P_0}$ are known. Figure D.3 illustrates the algorithm. Equation D.4 uses the projections of $\overrightarrow{\mathbf{L_0P_0}}$ and $\overrightarrow{\mathbf{L_0P_i}}$ on $\vec{\mathbf{N}}$ are the same. Rewriting Equation D.4 the distance between $\mathbf{L_0}$ and $\mathbf{P_i}$ is expressed as Equation D.5. The intersection can be found by adding $\overrightarrow{\mathbf{L_0P_i}}$ to $\mathbf{L_0}$ shown in Equation D.6.

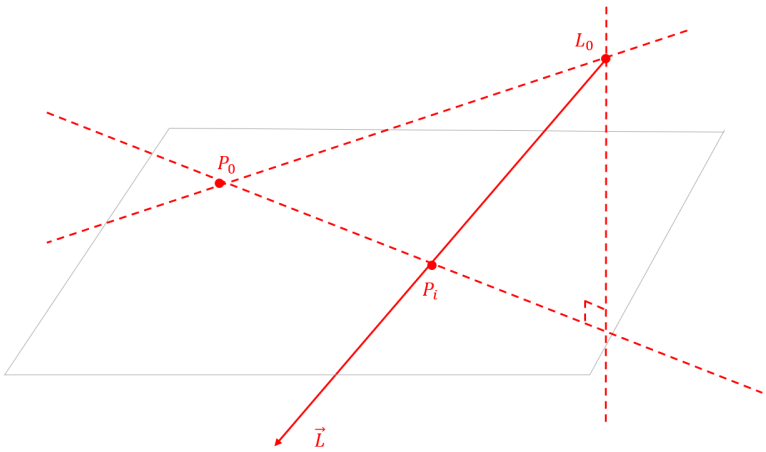

Figure D.3: Find the intersection with the known line vector $\vec{\mathbf{L}}$, normal vector of the plane $\vec{\mathbf{N}}$, a point $\mathbf{L_0}$ on the line and a point $\mathbf{P_0}$ on the plane.

$$\overrightarrow{\mathbf{L_0P_0}} \cdot \vec{\mathbf{N}} = \overrightarrow{\mathbf{L_0P_i}} \cdot \vec{\mathbf{N}} \tag{D.4}$$

$$|\,\mathbf{L_0P_i}\,| = \frac{\overrightarrow{\mathbf{L_0P_0}} \cdot \vec{\mathbf{N}}}{\frac{\vec{\mathbf{L}}}{|\,\vec{\mathbf{L}}|}\vec{\mathbf{N}}} \tag{D.5}$$

$$\mathbf{P_i} = \mathbf{L_0} + |\,\mathbf{L_0P_i}|\,\frac{\vec{\mathbf{L}}}{|\,\vec{\mathbf{L}}|} \tag{D.6}$$

D.4 Script for polarization modeling and interference signal simulating

```
% W.She
% 2022.5.3
clear;clc;close all;
addpath 'C:\Users\wshe\OneDrive - ASML\Personal notes\MSproject\Matlab\Design ...
    research\Config2_cc\Functions'
%% Geometry
n_air = 1; n_glass = 1.5; % refrective indices of air and glass
dis_mir = 583e-3;
theta_mir = 0e-6;
P_inc = [0 1 1]*10e-3; % incident point at CCR
P_ent = [-1 1 1]*22e-3; % a point at the entrance
```

```
%% Beam path
vec_in = [-1 5 -1];
vec_ref = RLT([1 0 0],vec_in);
vec_1 = Rrefraction([1 0 0],vec_in,n_air,n_glass);
vec_2 = RLT([0 0 1],vec_1);
vec_3 = Rrefraction([-1 1 1],vec_2,n_glass,n_air);
nor_mir = (RMy(theta_mir)*vec_3')';
vec_4 = RLT(nor_mir,vec_3);
vec_5 = Rrefraction([-1 1 1],vec_4,n_air,n_glass);
vec_6 = RLT([0 0 1],vec_5);
vec_7 = RLT([1 0 0],vec_6);
vec_8 = RLT([0 1 0],vec_7);
vec_9 = Rrefraction([-1 1 1],vec_8,n_glass,n_air);
vec_10 = RLT(nor_mir,vec_9);
vec_11 = Rrefraction([-1 1 1],vec_10,n_air,n_glass);
vec_12 = RLT([0 1 0],vec_11);
vec_mea = Rrefraction([1 0 0],vec_12,n_glass,n_air);
vec_mea = vec_mea*vec_ref(1)/vec_mea(1);

if (pi-Ang(vec_1,vec_2))<asin(n_air/n_glass)
    error('Not TIR at xy-plane')
end
if (pi-Ang(vec_7,vec_8))<asin(n_air/n_glass)
    error('Not TIR at xz-plane')
end

P_12 = intP(vec_1,P_inc,[0 0 1],[0 0 0]);
P_23 = intP(vec_2,P_12,[-1 1 1],P_ent);
P_mir = P_23 + vec_3*dis_mir;
P_45 = intP(vec_4,P_mir,[-1 1 1],P_ent);
P_56 = intP(vec_5,P_45,[0 0 1],[0 0 0]);
P_67 = intP(vec_6,P_56,[1 0 0],[0 0 0]);
P_78 = intP(vec_7,P_67,[0 1 0],[0 0 0]);
P_89 = intP(vec_8,P_78,[-1 1 1],P_ent);
P_910 = intP(vec_9,P_89,nor_mir,P_mir);
P_1011 = intP(vec_10,P_910,[-1 1 1],P_ent);
P_1112 = intP(vec_11,P_1011,[0 1 0],[0 0 0]);
P_exit = intP(vec_12,P_1112,[1 0 0],[0 0 0]);
WOW = sqrt(norm(P_exit - P_inc)^2 - abs(dot(vec_ref,P_exit - ...
    P_inc)/norm(vec_ref))^2);

ref_s = cross(vec_in,vec_ref)/norm(cross(vec_in,vec_ref)); % reference ...
    s-polarisation

R_12 = PRM(vec_12,vec_1,vec_2);
T_12 = RFM(vec_1,vec_2,n_glass,n_air);
T_mir = [-1 0;0 1];
R_21 = invPRM(vec_5,vec_6,vec_7);
T_21 = RFM(vec_5,vec_6,n_glass,n_air);

T_67 = RFM(vec_6,vec_7,n_glass,n_air);

R_78 = PRM(vec_6,vec_7,vec_8);
T_78 = RFM(vec_7,vec_8,n_glass,n_air);
R_1112 = invPRM(vec_11,vec_12,vec_mea);
T_1112 = RFM(vec_11,vec_12,n_glass,n_air);

T_mea = T_1112*R_1112*T_mir*T_78*R_78*T_67*T_21*R_21*T_mir*T_12*R_12;
T_ref = RFM(vec_in,vec_ref,n_air,n_glass);

%% Interference
% Constants
```

```
lambda = 1532e-9; k = 2*pi/lambda; NOP = 4;
A = [1; 1];
Ph0 = [0; 1]*linspace(0,2*pi,1e3)*NOP;
Ph90 = Ph0 + [0; pi/2];
Phopd = Ph0(2,:) - Ph0(1,:); Phdis = Phopd/2/pi/NOP;

azthe = linspace(0,pi/2);
testp = cos(azthe); tests = sin(azthe);
for j = 1:length(azthe)
    pol_sor = [testp(j) tests(j)];
    dm(j) = HQ(pol_sor,T_ref,T_mea);
end
dm = abs(dm-dm(1));

function dmPh = HQ(pol_sor,T_ref,T_mea)
A = [1;1];NOP = 4;
Ph0 = [0; 1]*linspace(0,2*pi,1e3)*NOP;
Ph90 = Ph0 + [0; pi/2];
pol_sor = pol_sor/norm(pol_sor);
pol_ref = (T_ref*pol_sor')';
pol_mea = (T_mea*pol_sor')';
E0p = A.*[pol_ref(1);pol_mea(1)].*exp(1i*Ph0);
E0s = A.*[pol_ref(2);pol_mea(2)].*exp(1i*Ph0);
E90p= A.*[pol_ref(1);pol_mea(1)].*exp(1i*Ph90);
E90s= A.*[pol_ref(2);pol_mea(2)].*exp(1i*Ph90);
I0 = abs(sum(E0p)).^2 + abs(sum(E0s)).^2; I0 = I0 - mean(I0);
I90 = abs(sum(E90p)).^2 + abs(sum(E90s)).^2; I90 = I90 - mean(I90);
dmPh = unwrap(atan2(I90,I0),pi/2);
dmPh = dmPh(1);
end
```

D.5 Script for calculating the beam walk-off and beam deviation caused by OE and target tip-tilt

```
% W.She
% 2022.5.3

clear;clc;close all;
addpath 'C:\Users\wshe\OneDrive - ASML\Personal notes\MSproject\Matlab\Design ...
    research\Config2_cc\Functions'

%% Beam tracing algorithm
n_air = 1; n_glass = 1.5;
nW_s = [0 0 -1]; % normal vector of wedge (standard)
nWf_s = (RMx(-deg2rad(3+53/60))*nW_s')'; % normal vector of wedge-tilted-surface

nRL = [1 1 0]; % normal vector of "left" surface of roof prism
nRR = [-1 1 0]; % normal vecteor of "right" surface of roof prism
dis_mir = 583e-3;
dtheta_mir = [0e-6 0 0];
P_inc = [-5 10 5]*1e-3;
switch 2
    case 1 % 1: inverse tracing (from mirror)
        a = 0;
        b = -1; %b>0
        c = 1; %c<0
        vec_1 = [a b c];
```

```
        vec_2 = RLT(nRR,vec_1);
        vec_3 = RLT(nRL,vec_2);
        vec_inw = Rrefraction(nW_s,vec_3,n_air,n_glass);
        vec_sor = Rrefraction(nWf_s,vec_inw,n_glass,n_air);
    case 2
        a = 0;
        b = -0.9445;
        c = -1.0526;
        vec_sor = [a b c]; % source
        vec_inw1 = Rrefraction(nWf_s,vec_sor,n_air,n_glass);
        vec_inw1R = RLT(nW_s,vec_inw1);
        vec_ref = Rrefraction(nWf_s,vec_inw1R,n_glass,n_air);
        vec_2 = Rrefraction(nW_s,vec_inw1,n_glass,n_air);
        vec_3 = RLT(nRL,vec_2);
        vec_4 = RLT(nRR,vec_3); % to the mirror
        nmir = vec_4;
        nmir = (RM(dtheta_mir)*nmir')';
        vec_5 = RLT(nmir,vec_4);
        vec_6 = RLT(nRR,vec_5);
        vec_7 = RLT(nRL,vec_6);
        vec_in0 = Rrefraction(nW_s,vec_7,n_air,n_glass); % compared to vec_inw1
        vec_8 = RLT(nW_s,vec_7); % to the mirror
        vec_9 = RLT(nmir,vec_8);
        vec_inw2 = Rrefraction(nW_s,vec_9,n_air,n_glass);
        vec_mea = Rrefraction(nWf_s,vec_inw2,n_glass,n_air);

        P_inw11R = intP(vec_inw1,P_inc,nW_s,[0 0 0]);
        P_inw1Rref = intP(vec_inw1R,P_inw11R,nWf_s,P_inc);
        P_23 = intP(vec_2,P_inw11R,nRL,[0 0 0]);
        P_34 = intP(vec_3,P_23,nRR,[0 0 0]);
        P_mir = P_34 + vec_4/norm(vec_4)*dis_mir;
        P_56 = intP(vec_5,P_mir,nRR,[0 0 0]);
        P_67 = intP(vec_6,P_56,nRL,[0 0 0]);
        P_78 = intP(vec_7,P_67,nW_s,[0 0 0]);
        P_89 = intP(vec_8,P_78,nmir,P_mir);
        P_9inw2 = intP(vec_9,P_89,nW_s,[0 0 0]);
        P_inw2mea = intP(vec_inw2,P_9inw2,nWf_s,P_inc);
        Lbatm = norm(P_mir-P_89);
        WOWc = sqrt(norm(P_inw2mea - P_inw1Rref)^2 - abs(dot(vec_ref,P_inw2mea ...
            - P_inw1Rref)/norm(vec_ref))^2);
        Angdiffc = Ang(vec_ref,vec_mea);
        NAc = atan((WOWc+1.8e-3+18.75e-3*Angdiffc)/18.75e-3);
end

%% Walk-off caused by target tip-tilt
dtheta_mirt = linspace(0e-6,1000e-6);
for j = 1:numel(dtheta_mirt)
    vec_int = [a b c];
    [WOW_angmir(j),¬,¬,¬] = solvehow(vec_int,[dtheta_mirt(j) 0 0],[0 0 0]); % a ...
        function repeating the beam tracing algorithm
    [WOW_angmirt(j),¬] = solvehowsp([a b c],dtheta_mirt(j)); % a function ...
        repeating the beam tracing algorithm
end
b_angmir = dtheta_mirt'\WOW_angmir';
b_angmirt = dtheta_mirt'\WOW_angmirt';

%% Reference and measurement beam deviation caused by OE
dtheta_w = linspace(0,100e-6);
for j = 1:numel(dtheta_w)
    vec_int = [a b c];
    [WOW_angwx(j),angwx(j),BDx(j),NAx(j)] = solvehow(vec_int,[0 0 ...
        0],[dtheta_w(j) 0 0]);
```

```
81      [WOW_angwy(j),angwy(j),BDy(j),NAy(j)] = solvehow(vec_int,[0 0 0],[0 ...
            dtheta_w(j) 0]);
82  end
83  b_wowwx = BDx'\WOW_angwx'; b_wowwy = BDy'\WOW_angwy';
84  b_angwx = BDx'\angwx'; b_angwy = BDy'\angwy';
85  b_NAx = BDx'\NAx'; b_NAy = BDy'\NAy';
```

Appendix E

Optics and fiber

E.1 Collimator

Some of useful information of the used collimator is shown in Table E.1 and Figure E.1 [51]. The part number of the used collimators is F280APC-1550.

Table E.1: Collimator data sheet used for theoretical calculations and lab tests in the project.

Item	Spec
Lens anti-reflective coating	1050 - 1620 nm $R_{avg} < 0.5\%$
Waist diameter	3.6 mm
Full-angle divergence	0.032°
Focus length	18.75 mm

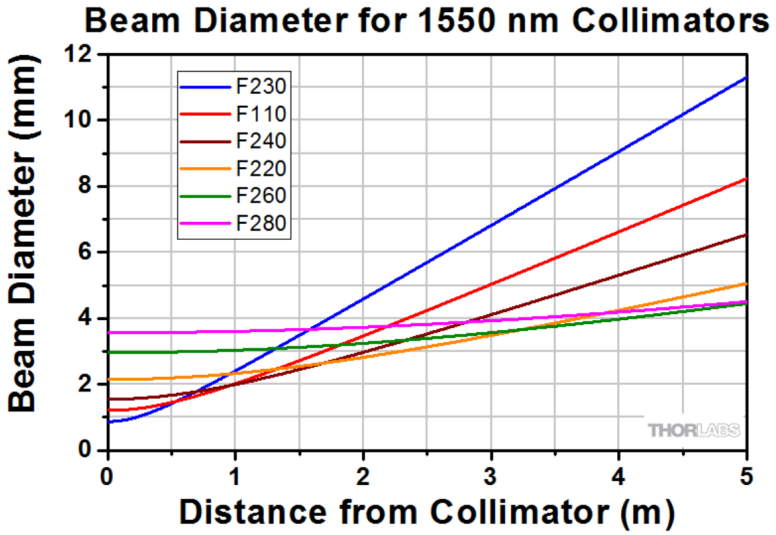

Figure E.1: Theoretical beam diameter for 1550 nm collimators. The one used in the project is corresponding to the pink line F280.

E.2 Single-mode fiber

Some of useful information of the used SMF is shown in Table E.2 [52]. The part number is SMF-28-J9. The Mode Field Diameter (MFD) is one measure of the beam width of light propagating in a SMF. The MFD is slightly larger than the core diameter since a small fraction of the light propagates in the cladding. The light can be approximated as a Gaussian power distribution, where the MFD is the diameter at which the optical power is reduced to $\frac{1}{e^2}$ from its peak level. MFD can be used to estimate the output beam diameter when focused by a collimator lens using Equation E.1 [53].

Table E.2: SMF data sheet used for theoretical calculations and lab tests in the project.

Item	Spec
Wavelength range	1260-1625 nm
Mode field diameter	10.4 ± 0.5 μm @ 1550 nm
Cladding	125 ± 0.7 μm
NA	0.14 mm

$$d \approx 4\lambda \frac{f}{\pi\, MFD} \tag{E.1}$$

Where λ is the wavelength of light being used, and f is the focal length of the collimator.

E.3 Round wedge prism

Some of useful information of the used round wedge prism is shown in Table E.3 and Figure E.2 [54]. The part number of the used round wedge prism is PS810.

Table E.3: Round wedge prism data sheet used for theoretical calculations and lab tests in the project.

Item	Spec
Diameter	25.4 mm
Beam deviation	2°
Material	N-BK7
Clear aperture	>80% of Diameter

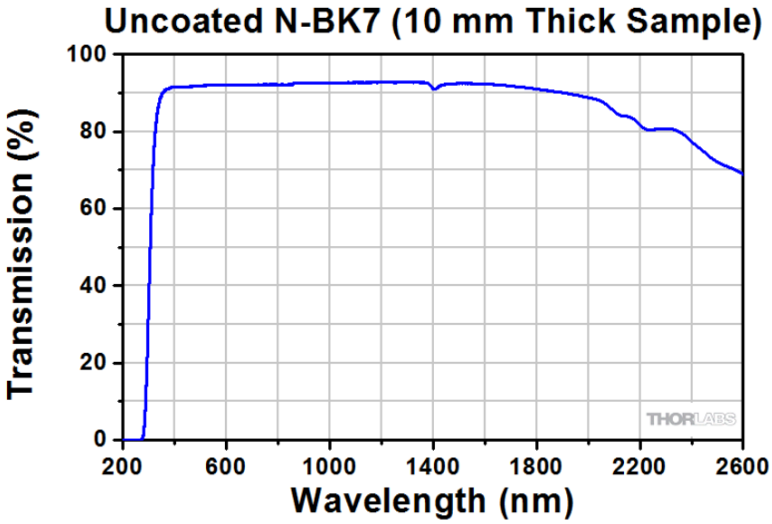

Figure E.2: Uncoated N-BK7 transmission with respect to wavelength curve.

E.4 Specular CCR

Some of useful information of the used specular CCR is shown in Table E.4 and Figure E.3 [44]. The part number of the used specular CCR is PS975-M01B.

Table E.4: Specular CCR data sheet used for theoretical calculations and lab tests in the project.

Item	Spec
Diameter	25.4 mm
Beam deviation	<3 arcsec
Clear aperture	>17.8 mm in Diameter
Coating range	800 - 2000 mm

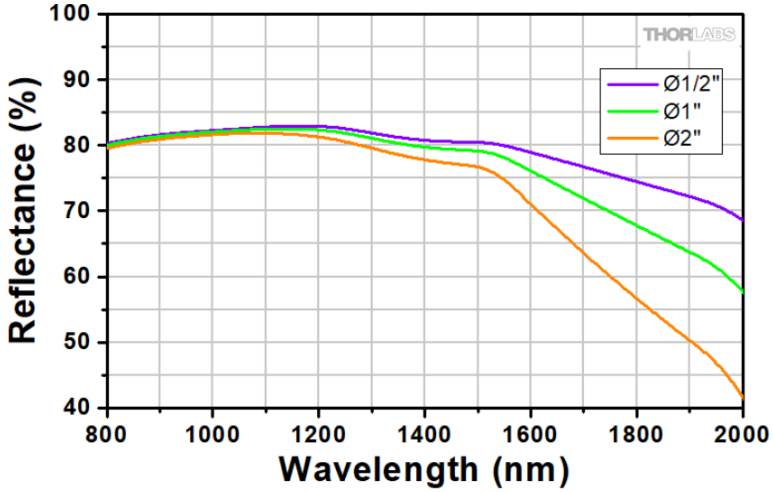

Figure E.3: Theoretical reflectance of N-BK7 retroreflectors with -M01B coating.

E.5 Mirror

Some of useful information of the used mirror is shown in Table E.5 [55].

Table E.5: Mirror data sheet used for theoretical calculations and lab tests in the project.

	PFSQ10-03-P01	**PFSQ20-03-P01**
Face dimensions	25.4 mm x 25.4 mm	50.8 mm x 50.8 mm
Reflectance	>96% for 2 - 20 µm	

E.6 Lens

Some of useful information of the lenses used in simulations is shown in Table E.6 [56] [57] [58].

Table E.6: Mirror data sheet used for theoretical calculations and simulations in the project.

Lens	**material**	**Diameter**	**Focal length (mm)**
Plano-convex	N-BK7	1 inch	99.7
Bi-convex	N-BK7	1 inch	100.0
Doublet	N-BAF10/N-SF6	1 inch	100.1
Doublet	N-BAF10/N-SF6	1 inch	30.4

E.7 Optical window

Some of useful information of the optical window used in simulations is shown in Table E.7[59]. The part number of the used optical window is WG11050.

Table E.7: Optical window data sheet used for theoretical calculations and simulations in the project.

Item	Spec
Diameter	25.4 mm
Thickness	5 mm
Material	N-BK7
Coating	Uncoated

E.8 Hollow roof prism

Some of useful information of the used hollow roof prism is shown in Table E.8, which is coated with unprotected gold. According to the Thorlabs introduction, the unprotected gold is ideal for use in applications where the polarization state needs to be strictly maintained or to prevent dispersion due to the overcoat of protected gold mirrors [60]. The part number of the used roof prism is HRS1015-M03.

Table E.8: Hollow roof prism data sheet used for theoretical calculations and lab tests in the project.

Item	Spec
Substrate dimension	25.4 mm x 25.4 mm
Mirror face dimension	25.4 mm x 18.03 mm
Dihedral angle accuracy	$\pm$10 arcsec
Coating	Unprotected gold for 800 nm - 2000 nm $R_{avg} > 97\%$

Appendix F

Optomechanics

The optomechanics used in the lab tests are shown in this appendix with their figures and key features. The reasons for using the specific optomechanics are also elaborated.

F.1 Fixed mirror mount

Figure F.1 shows the outlook of the fixed mirror mount used in the lab test [61]. It is used for mounting the wedge prism and the specular CCR. The specular CCR is fixed in the QI. The wedge prism does not require any degree of freedom in the DCI. Thus, the fixed mirror mount is the best choice for mounting the wedge prism in the DCI and the specular CCR in the QI.

The wedge prism used in the QI does need degrees of freedom, which is discussed in Section F.3.

Figure F.1: The outlook of the fixed mirror mount (FMP1/M) used in the lab test.

F.2 Kinematic pitch/yaw adapter

Figure F.2 shows the outlook of the kinematic pitch/yaw adapter used in the lab test [62]. It is used for mounting the collimator with an outer diameter of 11 mm. The collimator is used in both the QI and DCI. It needs the pitch and yaw degrees of freedom to complete a rough pointing. In the QI the collimator functions both delivering and receiving light. As long as the wedge prism is well aligned, the reference and the measurement beams can be easily coupled to the fiber. However in the DCI there are two collimators. For the receiving collimator, it is very important to have these degrees of freedom to point towards the reference and the measurement beams. Thus, the kinematic pitch/yaw adpater is the best choice for mounting the collimator.

The resolution of the kinematic pitch/yaw adapter is about 24 mrad per revolution.

Figure F.2: The outlook of the kinematic pitch/yaw adapter (KAD11NT) used in the lab test.

F.3 Bore kinematic mount

Figure F.3 shows the outlook of the bore kinematic mount used in the lab test [63]. It is used for mounting the wedge prism in the QI. Since the rear surface of the wedge prism must be 90° with respect to the incident beam, the wedge prism needs two rotation degrees of freedom. Subsection 5.4.4 has explained that although kinematic pitch/yaw adapters are used for the collimator, the resolution of the adapters is too coarse and the sensitivity of adjusting the collimator mount is double of adjusting the wedge prism mount. The bore kinematic mount is designed for 30 mm cage system. Since it is already available in the lab and compatible for 1 inch optics, it is the best choice for mounting the wedge prism in the QI.

Figure F.3: The outlook of the bore kinematic mount (KC1/M) used in the lab test.

F.4 Compact (square) kinematic mount

Figure F.4 shows the outlook of the compact square kinematic mount used in the lab test [64]. It is used for mounting the mirror in the QI. Since the mirror in the QI is intentionally tilted at an angle, the mirror needs two rotation degrees of freedom. Thus the compact square kinematic mount is the best choice for mounting the mirror in the QI.

Figure F.4: The outlook of the compact square kinematic mount (KMSR/M) used in the lab test.

F.5 Alignment plate

Figure F.5 shows the outlook of the alignment plate used in the lab test [65]. It is used for aligning the reference beam in the QI. Since in the QI the reference beam path is exactly coincidence with the path it comes, a tool for aligning two coincident beams in the reverse direction is needed. It is designed for 30 mm cage system, so it can be easily fixed and removed using a

simple cage system. Thus, the alignment plate is the best choice for aligning the reference beam in the QI.

Figure F.5: The outlook of the alignment plate (VRC6SCPT) used in the lab test.

F.6 Kinematic platform mount

Figure F.6 shows the outlook of the kinematic platform mount used in the lab test [66]. The kinematic platform mount has a large flat surface, which is suitable for placing the hollow roof prism. It also has a L-shaped frame separated from the platform. There several M4 tapped holes on the L-shaped frame, which can be used to connect other mechanics. When one of the platform or the L-shaped frame constrained, the other one has pitch and yaw degrees of freedom by rotating the knobs. The kinematic platform is the best choice for mounting the wedge prism and the roof prism, thus making a restructured CCR for the DCI with only off-the-shelf components.

Figure F.6: The outlook of the kinematic platform mount (KM200B/M) used in the lab test.

F.7 Kinematic rectangular mount

Figure F.7 shows the outlook of the kinematic rectangular mount used in the lab test [67]. It is used for mounting the mirror in the DCI. The mirror has to be pointed perpendicular to the measurement beams in the DCI. The mirror needs two rotation degrees of freedom. Thus the kinematic rectangular mount is the best choice for mounting the mirror in the DCI.

Figure F.7: The outlook of the kinematic rectangular mount (KM200S) in the lab test.

F.8 Optical construction post

Figure F.8 shows the outlook of the optical construction post used in the lab test [68]. It has five M4 counterbores and a mounting flat. It is used together with the angle post clamp (Appendix F.10) to mount the wedge prism on the L-shaped frame and in the meantime make it close to the roof prism.

Figure F.8: The outlook of the optical construction post (TR75C/M) in the lab test.

F.9 Adjustable clamping arm

Figure F.9 shows the outlook of the adjustable clamping arm used in the lab test [69]. It used for clamping the hollow roof prism.

Figure F.9: The outlook of the adjustable clamping arm (PM4/M) used in the lab test.

F.10 Angle post clamp

Figure F.9 shows the outlook of the angle post clamp used in the lab test [70]. The construction of the angle post clamp makes complex assemblies possible. It is used together with the optical construction post (Appendix F.8) to mount the wedge prism on the L-shaped frame and in the meantime make it close to the roof prism.

Figure F.10: The outlook of the angle post clamp (RA90/M) used in the lab test.

Appendix G

Electronics

The electronics devices used in the lab tests are shown in this appendix. Knowing the specifications of the devices helps decide whether the device is feasible for the test and make sure operating them correctly.

G.1 Laser and driver board

A DFB laser diode module from FITEL is used [71]. The emission wavelength is 1531.9 nm measured at 22.5°C. The DFB laser is integrated with an optical isolator, thus it can be used in the DCI test where the first-pass beam might go back to the laser. It can be directly connected to a modulator, and the polarization state of output laser beam is maintained to a consistent orientation. This does not conflict with the requirement of using non-polarizing light, since the modulated light will be delivered by a SMF. Increasing the junction temperature of the laser diode may degrade the device. In order to minimize this degradation, the driving current should not exceed the specified LO forward current (lfmax) and the temperature of the laser diode should be controlled at the specified operating temperature from 20°C to 35°C.

A digital butterfly laser diode driver from Koheron is used to modulate the injection current of laser. Some useful information of the driver is shown in Table G.1. In the lab tests the modulation frequency is set within the allowable range.

Table G.1: Some useful information of the used laser driver (Koheron CTL200)

Item	**Spec**
Laser current	5 mA to 225 mA
Modulation gain	2.5 mA/V
Modulation range	DC - 10 MHz

G.2 Photodetector and Picoscope

A low noise photodetector from Koheron and a Picoscope are used for measuring and sampling data [72] [73]. The bandwidth of the used photodetector is up to about 100 MHz. The sampling rate of the Picoscope is up to 1.25 GHz. In the lab tests the maximum used sampling rate is about 80 MHz.

Bibliography

[1] Gordon E Moore et al. *Cramming more components onto integrated circuits*. 1965.

[2] JCGM Jcgm et al. "Evaluation of measurement data—Guide to the expression of uncertainty in measurement". In: *Int. Organ. Stand. Geneva ISBN* 50 (2008), p. 134.

[3] K Baxter Larry. *Capacitive Sensors: Design and Applications*. 1997.

[4] "ASML internal reference".

[5] William T. Silfvast. "Lasers". In: *Encyclopedia of Physical Science and Technology (Third Edition)*. Ed. by Robert A. Meyers. Third Edition. New York: Academic Press, 2003, pp. 267–281. ISBN: 978-0-12-227410-7. DOI: https://doi.org/10.1016/B0-12-227410-5/00363-X. URL: https://www.sciencedirect.com/science/article/pii/B012227410500363X.

[6] AF Fercher, Hong Zhang Hu, and U Vry. "Rough surface interferometry with a two-wavelength heterodyne speckle interferometer". In: *Applied optics* 24.14 (1985), pp. 2181–2188.

[7] Timothy Alan Heumier. "Mode hopping in semiconductor lasers". PhD thesis. Montana State University-Bozeman, College of Letters & Science, 1992.

[8] Haiyin Sun. *Laser diode beam basics, manipulations and characterizations*. Springer Science & Business Media, 2012.

[9] Ali Reza Bahrampour et al. "Optical fiber interferometers and their applications". In: *Interferometry-Research and Applications in Science and Technology* 1 (2012), pp. 3–30.

[10] Govind P. Agrawal. "Chapter 1 - Introduction". In: *Nonlinear Fiber Optics (Sixth Edition)*. Ed. by Govind P. Agrawal. Sixth Edition. Academic Press, 2019, pp. 1–25. ISBN: 978-0-12-817042-7. DOI: https://doi.org/10.1016/B978-0-12-817042-7.00008-7. URL: https://www.sciencedirect.com/science/article/pii/B9780128170427000087.

[11] William Shieh and Ivan B Djordjevic. *OFDM for optical communications*. Academic press, 2009.

[12] Holmarc. *Corner Retroreflector Prisms*. URL: https://www.holmarc.com/corner_cube_retroreflectors.php (visited on 03/06/2022).

[13] MA Acharekar. "Derivation of internal incidence angles and coordinate transformations between internal reflections for corner reflectors at normal incidence". In: *Optical Engineering* 23.5 (1984), p. 235669.

[14] Grant R. Fowles. Dover Publications, 1975, pp. 38–40. ISBN: 978-0-486-65957-2. URL: https://app.knovel.com/hotlink/toc/id:kpIMOE0001/introduction-modern-optics/introduction-modern-optics.

[15] SCHOTT. *Optical Glass Collection Datasheets*. 2021. URL: https://mss-p-009-delivery.stylelabs.cloud/api/public/content/fbe7dba4c62540d889539c1ffc4b24d4?v=240eeb85&download=true (visited on 01/09/2022).

[16] Albert A Michelson and Edward W Morley. "On the Relative Motion of the Earth and of the Luminiferous Ether". In: *Sidereal Messenger, vol. 6, pp. 306-310* 6 (1887), pp. 306–310.

[17] K P Zetie, S F Adams, and R M Tocknell. "How does a Mach-Zehnder interferometer work?" In: *Physics Education* 35.1 (2000), pp. 46–48. DOI: 10.1088/0031-9120/35/1/308. URL: https://doi.org/10.1088/0031-9120/35/1/308.

[18] Joseph M Geary. *Introduction to optical testing*. Vol. 15. SPIE Press, 1993.

[19] Norman Bobroff. "Recent advances in displacement measuring interferometry". In: *Measurement Science and Technology* 4.9 (1993), p. 907.

[20] Vidi Saptari. *Fourier transform spectroscopy instrumentation engineering*. SPIE Optical Engineering Press Bellingham Washington, DC, 2003.

[21] Peter L. M. Heydemann. "Determination and correction of quadrature fringe measurement errors in interferometers". In: *Appl. Opt.* 20.19 (1981), pp. 3382–3384. DOI: 10.1364/AO.20.003382. URL: http://www.osapublishing.org/ao/abstract.cfm?URI=ao-20-19-3382.

[22] Anthony Dandridge, Alan B Tveten, and Thomas G Giallorenzi. "Homodyne demodulation scheme for fiber optic sensors using phase generated carrier". In: *IEEE Transactions on microwave theory and techniques* 30.10 (1982), pp. 1635–1641.

[23] David L Colton, Rainer Kress, and Rainer Kress. *Inverse acoustic and electromagnetic scattering theory*. Vol. 93. Springer, 1998.

[24] Russell Loughridge and Daniel Y. Abramovitch. "A tutorial on laser interferometry for precision measurements". In: *2013 American Control Conference*. 2013, pp. 3686–3703. DOI: 10.1109/ACC.2013.6580402.

[25] José Henrique Galeti, Cláudio Kitano, and Michael J. Connelly. "Improved synthetic-heterodyne Michelson interferometer vibrometer using phase and gain control feedback". In: *Appl. Opt.* 54.35 (2015), pp. 10418–10424. DOI: 10.1364/AO.54.010418. URL: http://www.osapublishing.org/ao/abstract.cfm?URI=ao-54-35-10418.

[26] James H Cole, Bruce A Danver, and Joseph A Bucaro. "Synthetic-heterodyne interferometric demodulation". In: *IEEE Transactions on Microwave Theory and Techniques* 30.4 (1982), pp. 540–543.

[27] Tony L. Schmitz et al. "Periodic error correction in heterodyne interferometry". In: *2013 American Control Conference*. 2013, pp. 3712–3716. DOI: 10.1109/ACC.2013.6580404.

[28] Chien-ming Wu and Ching-shen Su. "Nonlinearity in measurements of length by optical interferometry". In: *Measurement Science and Technology* 7.1 (1996), p. 62.

[29] Pengcheng Hu et al. "Nonlinearity error in homodyne interferometer caused by multi-order Doppler frequency shift ghost reflections". In: *Opt. Express* 25.4 (2017), pp. 3605–3612. DOI: 10.1364/OE.25.003605. URL: http://www.osapublishing.org/oe/abstract.cfm?URI=oe-25-4-3605.

[30] GV Fedotova. "Analysis of the measurement error of the parameters of mechanical vibrations". In: *Measurement Techniques* 23.7 (1980), pp. 577–580.

[31] Suzanne Johanna Antonetta Geertruda Cosijns. "Displacement laser interferometry with sub-nanometer uncertainty". In: (2004).

[32] RWP Drever et al. "Laser phase and frequency stabilization using an optical resonator". In: *Applied Physics B* 31.2 (1983), pp. 97–105.

[33] DR Scifres, RD Burnham, and W Streifer. "Distributed-feedback single heterojunction GaAs diode laser". In: *Applied Physics Letters* 25.4 (1974), pp. 203–206.

[34] Bengt Edlén. "The Refractive Index of Air". In: *Metrologia* 2.2 (1966), pp. 71–80. DOI: 10.1088/0026-1394/2/2/002. URL: https://doi.org/10.1088/0026-1394/2/2/002.

[35] K P Birch and M J Downs. "An Updated Edlén Equation for the Refractive Index of Air". In: *Metrologia* 30.3 (1993), pp. 155–162. DOI: 10.1088/0026-1394/30/3/004. URL: https://doi.org/10.1088/0026-1394/30/3/004.

[36] K P Birch and M J Downs. "Correction to the Updated Edlén Equation for the Refractive Index of Air". In: *Metrologia* 31.4 (1994), pp. 315–316. DOI: 10.1088/0026-1394/31/4/006. URL: https://doi.org/10.1088/0026-1394/31/4/006.

[37] Philip E. Ciddor. "Refractive index of air: new equations for the visible and near infrared". In: *Appl. Opt.* 35.9 (1996), pp. 1566–1573. DOI: 10.1364/AO.35.001566. URL: http://www.osapublishing.org/ao/abstract.cfm?URI=ao-35-9-1566.

[38] Philip E. Ciddor and Reginald J. Hill. "Refractive index of air. 2. Group index". In: *Appl. Opt.* 38.9 (1999), pp. 1663–1667. DOI: 10.1364/AO.38.001663. URL: http://www.osapublishing.org/ao/abstract.cfm?URI=ao-38-9-1663.

[39] ASML-SPM-EUV. "PIR PHASE GENERATED CARRIER INTERFEROMETER INTERROGATOR".

[40] R. Paschotta. "Modulation depth". In: *Encyclopedia of Laser Physics and Technology* (2008).

[41] Maarten Jozef JANSEN. Pat. WO2022042947A1.

[42] "Interferometer System and Lithographic Apparatus". Pat.

[43] Wouter Onno Pril. "Development of high precision mechanical probes for coordinate measuring machines". In: *PhD. Thesis, Eindhoven University of Technology* (2002), pp. 64–66.

[44] THORLABS. *Specular retroreflector prisms*. URL: https://www.thorlabs.com/newgrouppage9.cfm?objectgroup_id=13580 (visited on 06/24/2022).

[45] Grant R Fowles. *Introduction to modern optics*. Courier Corporation, 1989, pp. 22–25.

[46] Jian Liu and R. M. A. Azzam. "Polarization properties of corner-cube retroreflectors: theory and experiment". In: *Appl. Opt.* 36.7 (1997), pp. 1553–1559. DOI: 10.1364/AO.36.001553. URL: http://www.osapublishing.org/ao/abstract.cfm?URI=ao-36-7-1553.

[47] Francis Arthur Jenkins and Harvey Elliott White. "Fundamentals of optics". In: *Indian Journal of Physics* 25 (1957), pp. 265–266.

[48] THORLABS. *Mounted hollow retroreflector mirrors*. URL: https://www.thorlabs.com/newgrouppage9.cfm?objectgroup_id=12625 (visited on 06/24/2022).

[49] Milton Abramowitz, Irene A Stegun, and Robert H Romer. *Handbook of mathematical functions with formulas, graphs, and mathematical tables*. 1988.

[50] Dan Zwillinger. *CRC standard mathematical tables and formulas*. chapman and hall/CRC, 2018.

[51] THORLABS. *Fixed focus collimation packages: FC/APC connectors*. URL: https://www.thorlabs.com/newgrouppage9.cfm?objectgroup_id=1696 (visited on 06/15/2022).

[52] THORLABS. *Single Mode Fiber*. URL: https://www.thorlabs.com/newgrouppage9.cfm?objectgroup_id=949 (visited on 06/16/2022).

[53] THORLABS. *Fixed focus collimation packages: FC/APC connectors*. URL: https://www.thorlabs.com/newgrouppage9.cfm?objectgroup_id=1696&pn=F280APC-1550#5983 (visited on 06/16/2022).

[54] THORLABS. *Round wedge prisms*. URL: https://www.thorlabs.com/newgrouppage9.cfm?objectgroup_id=147 (visited on 06/24/2022).

[55] THORLABS. *Protected Silver Mirrors*. URL: https://www.thorlabs.com/newgrouppage9.cfm?objectgroup_id=903&pn=PFSQ20-03-P01 (visited on 06/24/2022).

[56] THORLABS. *N-BK7 Plano-Convex Lenses*. URL: https://www.thorlabs.com/newgrouppage9.cfm?objectgroup_id=3281 (visited on 06/24/2022).

[57] THORLABS. *N-BK7 Bi-Convex Lenses*. URL: https://www.thorlabs.com/newgrouppage9.cfm?objectgroup_id=4850 (visited on 06/24/2022).

[58] THORLABS. *Unmounted Achromatic Doublets*. URL: https://www.thorlabs.com/newgrouppage9.cfm?objectgroup_id=899 (visited on 06/24/2022).

[59] THORLABS. *N-BK7 High Precision Windows*. URL: https://www.thorlabs.de/newgrouppage9.cfm?objectgroup_id=1117 (visited on 06/24/2022).

[60] THORLABS. *Retroreflecting Hollow Roof Prism Mirrors*. URL: https://www.thorlabs.com/newgrouppage9.cfm?objectgroup_ID=10007 (visited on 06/24/2022).
[61] THORLABS. *Fixed Mirror Mounts*. URL: https://www.thorlabs.com/newgrouppage9.cfm?objectgroup_id=989 (visited on 06/24/2022).
[62] THORLABS. *Kinematic Pitch/Yaw Adapter for Ø11 mm Cylindrical Components*. URL: https://www.thorlabs.com/thorproduct.cfm?partnumber=KAD11NT (visited on 06/24/2022).
[63] THORLABS. *30 mm Cage-Compatible Smooth Bore Kinematic Mount*. URL: https://www.thorlabs.com/newgrouppage9.cfm?objectgroup_id=185 (visited on 06/24/2022).
[64] THORLABS. *Compact Kinematic Mount for 25.4 mm Tall Rectangular Optics, M4 Taps*. URL: https://www.thorlabs.com/thorproduct.cfm?partnumber=KMSR/M#ad-image-0 (visited on 06/24/2022).
[65] THORLABS. *30 mm Cage System Alignment Plate with MIR Disk*. URL: https://www.thorlabs.com/newgrouppage9.cfm?objectgroup_id=3201&pn=VRC6SCPT (visited on 06/24/2022).
[66] THORLABS. *Kinematic Platform Mount*. URL: https://www.thorlabs.com/newgrouppage9.cfm?objectgroup_id=1811&pn=KM200B/M (visited on 06/24/2022).
[67] THORLABS. *Kinematic Mount for 2" (50.8 mm) Tall Rectangular Optics, Right Handed*. URL: https://www.thorlabs.com/newgrouppage9.cfm?objectgroup_id=3971&pn=KM200S#5122 (visited on 06/24/2022).
[68] THORLABS. *Optical Construction Post, SS, M4 Counterbores*. URL: https://www.thorlabs.com/thorproduct.cfm?partnumber=TR75C/M (visited on 06/24/2022).
[69] THORLABS. *Large Adjustable Clamping Arm, M4 x 0.7 Threaded Post*. URL: https://www.thorlabs.com/thorproduct.cfm?partnumber=PM4/M (visited on 06/24/2022).
[70] THORLABS. *Angle Post Clamps*. URL: https://www.thorlabs.com/newgrouppage9.cfm?objectgroup_id=1985&pn=RA90/M (visited on 06/24/2022).
[71] FITEL. *1529nm-1611nm, 40mW, DWDM*. URL: https://www.laserdiodesource.com/shop/1529nm-1611nm-40mW-butterfly-DWDM-Fitel (visited on 06/24/2022).
[72] Koheron. *Low noise photodetector*. URL: https://www.koheron.com/photonics/pd100-photodetection (visited on 06/24/2022).
[73] PicoScope. *PicoScope 6000E Series*. URL: https://www.picotech.com/oscilloscope/6000/picoscope-6000-overview (visited on 06/24/2022).

Acknowledgements

During the time studying at TU Delft and doing internship at ASML I have learned a lot in terms of knowledge and personal development. In the Master program High-tech engineering at TU Delft, I finally had the opportunity to follow the courses truly attracting me. At ASML I started to know how the knowledge I learned is applied in the cutting edge of technology, and to think what career I truly want to pursue. To make these happen, I would like to thank my parents for supporting my decision on study in the Netherlands both mentally and financially. I would also like to thank J. P. Kappelhof and L. A. Cacace for teaching me Opto-mechatronics course and introducing the precious internship opportunity at ASML.

My company supervisor W. Pril is the person I am most grateful for. I would like to thank him for his professional and patient guidance throughout my internship. Every talk with him was so interesting, informative and inspiring.

In my university, I would like to thank my coach N. Bhattacharya for her patient guidance. Through her regular meetings my project proceeded methodically. I would like to thank the L. A. Cacace and Opto-Mechatronics group members: Aditya Garde, Emile Heezen and Sawa Bezelev. Every Opto-Mechatronics meeting was interesting and inspiring. I would like to give special thanks to Sawa Bezelev. Throughout the project, I often discussed my confusion with him. He always thought and answered carefully. He also put forward a lot of revisions to my thesis in detail, both in knowledge and in English expressions. In my company, I would like to thank all my colleagues in the ASML SPM group. They are very friendly and made me feel integrated. I would like to thank my group leader Kees van Weert, who regularly tracked my progress and helped me resolve management issues immediately. I would like to thank Niels de Goeij, who cared so much about my internship and life, and always listened and gave advice very patiently. I would like to thank Aditya Singh, he always helped me with the lab equipments and the problems I encountered in my experiments. I would like to thank Maarten Jansen and Ton Ikkink, they helped me understand a lot of phase detection algorithms. I want to thank Thomas Theunisse for lots of interesting daily chats with him. I would like to thank Jiajin Li, who is in the MTD group and graduated from the same faculty in TU Deflt, for telling me lots of company backgrounds and giving me a lot of guidance on my project. There are also many colleagues not mentioned, each of whom makes me feel the harmony of ASML.

Further I would like to thank all the members of my committee for their support and for reviewing this thesis: Dr N. Bhattacharya, Dr.ir. M. Tichem, Dr S. Iskander-Rizk, Dr A.J.L. Adam, Dr L.A. Cacace and Dr W. Pril.

I thank everyone, I have not mentioned earlier, and contributed in my study and life. Finally I want to sincerely thank my girlfriend Jialing Zou for the happiness during the two years' study abroad.